*Doklady Physics, Vol. 49, No. 5, 2004, pp. 261–265. Translated from Doklady Akademii Nauk, Vol. 396, No. 1, 2004, pp. 35–40.*
*Original Russian Text Copyright © 2004 by Grigor'eva.*

**PHYSICS**

# Crystal-Geometry Description of the Morphological Features and Determination of the Chiral Angle of Carbon Nanotubes

**L. D. Grigor'eva**

Presented by Academician Yu.A. Osip'yan July 10, 2003

Received October 23, 2003

A carbon nanotube is a surface carbon structure that is morphologically a crystal bent around a certain axis in the *ab* graphite plane. Each carbon loop of the graphite plane is a benzene-type hexagon that has carbon atoms in its nodes and a 1.42-Å-long side (Fig. 1a). The elementary cell of the two-dimensional crystal lattice of the *ab* graphite plane can be specified by the basis vectors **a** and **b**, whose length $|\mathbf{a}| = |\mathbf{b}| = 2.46$ Å and angle between them is equal to 120° (Fig. 1). The elementary cell of the spatial crystal lattice of graphite is obtained by complementing these two vectors with the basis vector **c** that is perpendicular to the *ab* plane and has length $|\mathbf{c}| = 6.70$ Å.

The nanotube is a chiral object. Let the rolling of the graphite plane into a cylinder lead to the coincidence of the $(m, n)$ hexagon with the (0, 0) hexagon located at the origin (Fig. 1b). A line connecting the $(m, n)$ and (0, 0) hexagons is called the chiral direction. Then, $(m, n)$ are the chiral indices, and the chiral angle is the angle $\alpha$ between the chiral direction and direction in which the neighboring hexagons have a common side. The chiral characteristics of the nanotube are important, because they determine the electronic properties of the carbon nanotube [1–3].

The reciprocal lattice of the single-wall nanotube is a body generated by rotating the point nodes of the reciprocal lattice of the graphite plane *ab* about an axis arbitrarily oriented in this plane. The axis of the ordinarily oriented nanotube is perpendicular to an electron beam. Therefore, the corresponding electron diffraction pattern is the reciprocal-lattice section that passes through the nanotube axis. The morphological features of the nanotube graphite structure lead to the features of the electron diffraction patterns of this structure. This work aims to determine the crystallographic directions of the chiral characteristics of the nanotube, to describe the position of the nodes of the reciprocal lattice, and to determine the nanotube chiral angle.

The nanotube is geometrically a right cylinder, where the chiral direction is a closed directrix and a straight line parallel to the nanotube axis is its generatrix. The directrix of the right cylinder is perpendicular to its generatrix. Therefore, the chiral direction is perpendicular to the nanotube axis. Figure 1 shows the chiral directions with the indices (8, 0), (7, 1), (8, 3), and (8, 4) and corresponding nanotube axes. The chiral angle varies from 0° to 30°. Let us construct the basis vectors **a*** and **b*** of the reciprocal lattice for the two-dimensional direct lattice specified by the basis vectors **a** and **b**, as is shown in Fig. 1c. Let us determine the crystallographic directions of the basic characteristics of the nanotube for the extreme chiral angles 0° and 30° (Fig. 1). The results are presented in the table.

For an arbitrary chiral angle $0° < \alpha < 30°$, the characteristics of the nanotube are between those presented in the table. According to the above definition of the chiral angle, Fig. 1, and the table, the chiral angle in the direct lattice is equal to the angle between the nanotube axis and the [120] direction, and in the electron diffraction pattern, it is the angle between the nanotube axis and the [010]* direction. Since the multiwall-nanotube axis always lies in the *ab* plane, the multiwall nanotube is always perpendicular to the *Z* axis, which is manifested on the electron diffraction pattern as $(00l)$ reflec-

**Table**

| Chiral indices $(m, n)$ | $(m, 0)$ | $(2n, n)$ |
|---|---|---|
| Chiral angle $\alpha$, deg | 0 | 30 |
| Chiral direction in the direct lattice | [100] | [210] |
| Chiral direction in the reciprocal lattice | $[2\bar{1}0]$* | [100]* |
| Nanotube axis direction in the direct lattice | [120] | [010] |
| Nanotube axis direction in the reciprocal lattice | [010]* | $[\bar{1}20]$* |

* Hereinafter, the dot at the place of the third index is omitted.

---

*Institute of Solid State Physics,*
*Russian Academy of Sciences, Chernogolovka,*
*Moscow oblast, 142432 Russia*
*e-mail: ldg@issp.ac.ru*

1028-3358/04/4905-0261$26.00 © 2004 MAIK "Nauka/Interperiodica"

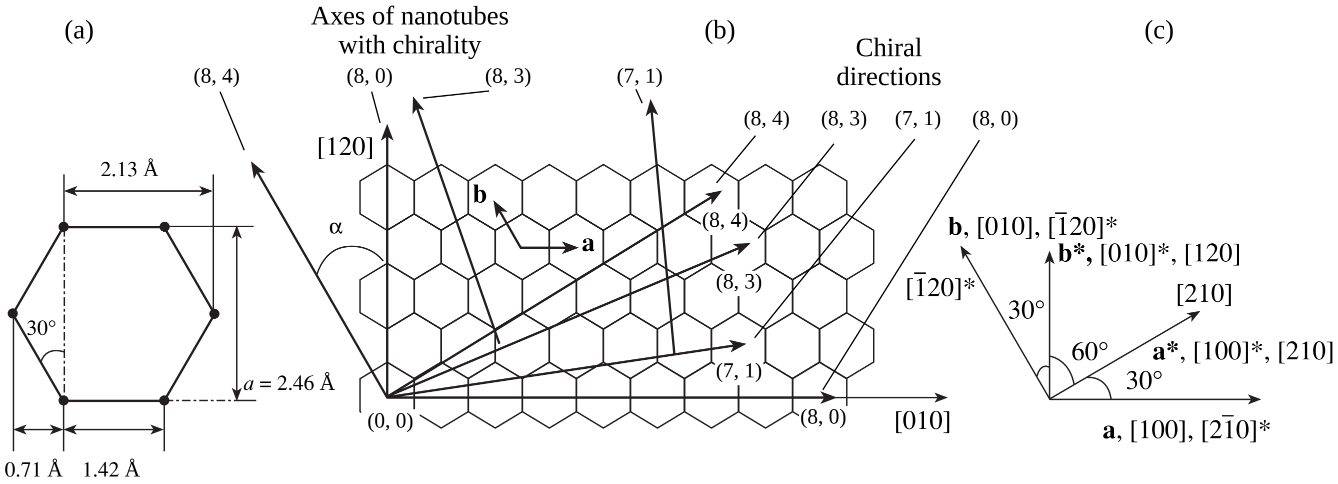

**Fig. 1.** (a) Carbon hexagon, where *a* is the length of the elementary-cell edge; (b) the (001) graphite plane, where the elementary cell is specified by the basis vectors **a** and **b**, the coordinates of hexagons are given by the numbers (*m*, *n*), and the chiral direction, the direction of the nanotube axis, and chiral angle α with the chiral indices (8, 4) are indicated for the plane rolled into the nanotube; and (c) the crystallographic directions in the direct and reciprocal lattices of the graphite *ab* plane, [100] ⊥ [120], [010] ⊥ [210], and **a*** ⊥ **b** and **b*** ⊥ **a** according to the construction of the reciprocal lattice.

tions presenting the interlayer distance in graphite (Fig. 2b). Therefore, the axis of the multiwall nanotube is always perpendicular to the line of the positions of (00*l*) reflections.

On the basis of the above crystallographic directions of the basic characteristics of the nanotube structure, let us describe the positions of the (*h*, *k*, 0) nodes of the reciprocal lattice of the arbitrary-chirality carbon nanotube. The *X** and *Y** axes are specified as is shown in Fig. 2a. In this case, the nodes of the reciprocal lattice of the *ab* graphite plane have indices shown in Fig. 2. Let us rotate the shown section of the reciprocal lattice of graphite about the nanotube axis, which, as follows from the table, must lie in the *a***b** plane between the [010]* (*Y** axis) and $[\bar{1}20]$* directions (Fig. 2b). In this case, the *X** and *Y** axes are transformed to the *X**' and *Y**' axes, respectively. Thus, a node symmetric about the rotation axis appears for each node, and 12 nodes, rather than 6 nodes as usually in graphite with a rectilinear node row, lie on circles uniting the {100} and {110} nodes. The chiral angle in the reciprocal lattice is the angle between the nanotube axis and [010]* direction. Therefore, the chiral angle can be determined from the electron diffraction pattern and is equal to half the angle between the radius vectors of the (010) and (010)' nodes. Considering two equilateral triangles that are formed by the {(110), $(\bar{1}20)$, (000)} and {(110)', $(\bar{1}20)$', (000)} nodes and are turned with respect to each other by angle 2α, we conclude that the double chiral angle also appears as the angle between the radius vectors of the (110) and $(\bar{1}20)$' nodes (or pairs symmetrically equivalent to them).

Thus, the rotation of the reciprocal lattice about the nanotube axis arbitrarily directed between the [010]* and $[\bar{1}20]$* directions leads to the splitting of nodes. The angle between the radius vectors of the split reflections (010) and (010)' or (110) and $(\bar{1}20)$' (Fig. 2) is equal to the double chiral angle of the nanotube. Splitting is due to the fact that nodes symmetric for graphite with a parallelepiped lattice [e.g., (110) and $(\bar{1}20)$ nodes symmetric about the *Y** axis, see Fig. 2a] are generally not symmetric about the rotation axis in the lattice of cylindrical graphite. Therefore, the nodes are not transformed to each other by rotation and take the (110)' and $(\bar{1}20)$' positions, different from the symmetric positions usual for parallelepiped graphite. It is easy to understand that nodes are not split when the rotation axis of the reciprocal lattice coincides with one of the [010]* and $[\bar{1}20]$* directions, which corresponds to a chiral angle of 0° and 30°, respectively.

The arrangement of nodes of the hexagonal grid of the reciprocal lattice arising from the graphite plane (Fig. 2a) is uniquely specified by the interplane spacings $d_{hk0}$ in the graphite plane that determine the distances from the (*hk*0) nodes of the reciprocal lattice to the center of the electron diffraction pattern [4]. In the reciprocal lattice of the graphite plane rolled into a cylinder, the number of the (*hk*0) nodes is generally twice as large as that in the graphite plane with a rectilinear node row, and the positions of nodes depend on the position of the rotation axis. Therefore, interplane spacings are insufficient for the complete characteristic of the electron diffraction pattern. The position of each (*hk*0) node in the reciprocal lattice of the nanotube is specified by two parameters: the distance $D_{hk0}$ from the node to the rotation axis and the distance $S_{hk0}$ from the origin to the plane that is perpendicular to the rotation

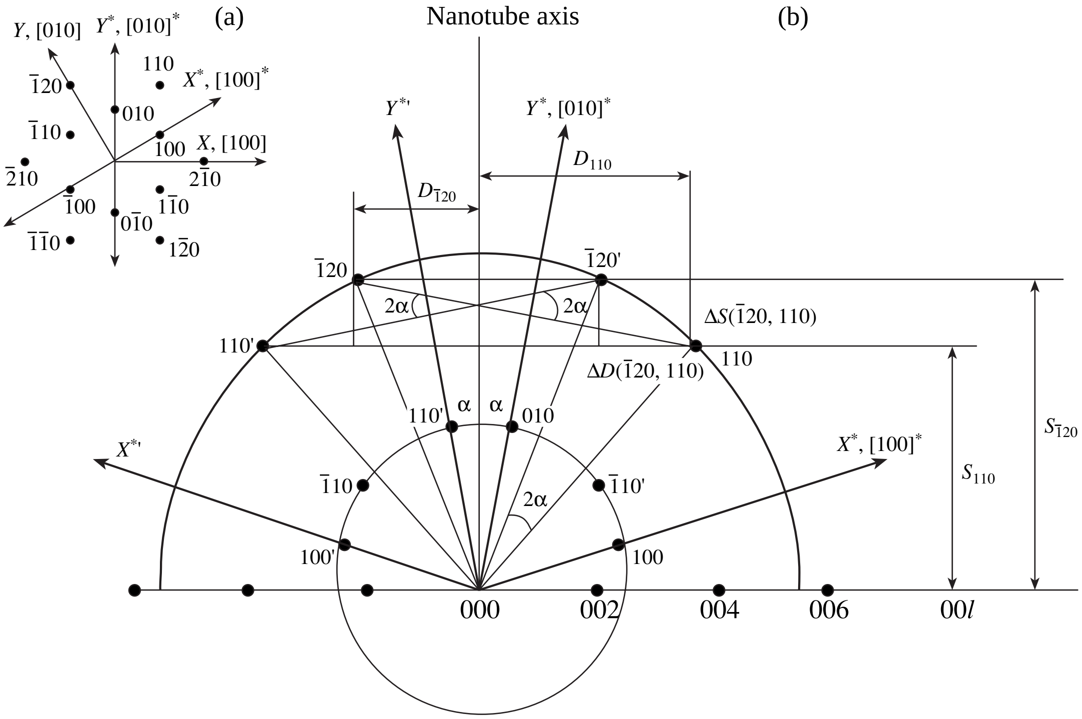

**Fig. 2.** (a) Directions in the direct and reciprocal lattices and node indices in the [001] zone of graphite with a parallelepiped cell, and (b) the scheme of an electron diffraction pattern of a multiwall monochiral carbon nanotube as a result of the rotation of the nodes of the reciprocal lattice that are shown in Fig. 2a about the nanotube axis (some nodes are shown). The prime denotes the directions and reflections arising due to the rotation of the reciprocal lattice about the nanotube axis. The $(\bar{1}20)$ and (110) reflections are symmetric about the $Y^*$ axis, and the $(\bar{1}20)'$ and (110)' reflections are symmetric about the $Y^{*\prime}$ axis. The scheme shows the splitting of the reflections for $0° < \alpha < 30°$ and determination of the quantities $D_{hk0}$, $S_{hk0}$, $\Delta D$, and $\Delta S$ for the $(\bar{1}20)'$ and (110) nodes that do not coincide for $\alpha \neq 0$ and the arising splitting is characterized by the parameters $\Delta D = \Delta D(\bar{1}20, 110)$ and $\Delta S = \Delta S(\bar{1}20, 110)$.

axis and passes through the given node [shown in Fig. 2 for the $(\bar{1}20)$ and (110) nodes]. Let us find the dependence of these parameters on the chiral angle for an arbitrary node of the lattice that is rolled into a cylinder and whose cell has the edges $a$, $b$, and $c$ and angles $\alpha = \beta = 90°$ and $\gamma$.

We consider the row of nodes ($h0l$) in the reciprocal lattice with the basis vectors $\mathbf{a}^*$, $\mathbf{b}^*$, and $\mathbf{c}^*$ with fixed $h$ and varying $l$ indices. This row is parallel to the $Z^*$ axis and, according to its indices, cuts the interval $ha^* = \dfrac{h}{a\sin\gamma}$ on the $X^*$ axis. The position of this row is described by the parameters $D_{h00}$ and $S_{h00}$ (Fig. 3a). Similarly, the row of the ($0kl$) nodes with fixed $k$ and varying $l$ indices cuts interval $kb^* = \dfrac{k}{b\sin\gamma}$ on the $Y^*$ axis and is described by the parameters $D_{0k0}$ and $S_{0k0}$. Thus, the position of the row of nodes with fixed $h$ and $k$ indices and varying $l$ index that is projected into the ($hk0$) reflection on the $a^*b^*$ plane is described by the quantities

$$D_{hk0} = |D_{h00} + D_{0k0}|$$
$$= \left|\frac{h}{a\sin\gamma}\sin(\gamma^* + \alpha) + \frac{k}{b\sin\gamma}\sin\alpha\right|,$$
$$S_{hk0} = |S_{h00} + S_{0k0}|$$
$$= \left|\frac{h}{a\sin\gamma}\cos(\gamma^* + \alpha) + \frac{k}{b\sin\gamma}\cos\alpha\right|.$$

For nodes on the rotation axis, $D_{hk0} = 0$, whereas $S_{hk0} = 0$ for nodes on the equatorial line of the electron diffraction pattern.

For the hexagonal lattice of graphite, where $a = b = 2.46$ Å, $\gamma = 120°$, and $\gamma^* = 180° - \gamma = 60°$, we have

$$D_{hk0} = \left|\frac{h}{2.13}\sin(60 + \alpha) + \frac{k}{2.13}\sin\alpha\right|, \quad (1)$$

$$S_{hk0} = \left|\frac{h}{2.13}\cos(60 + \alpha) + \frac{k}{2.13}\cos\alpha\right|. \quad (2)$$

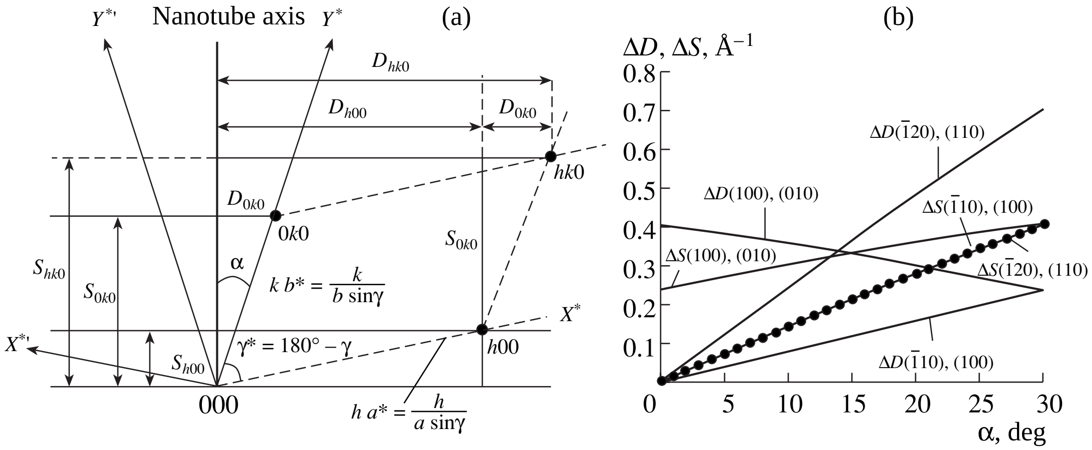

**Fig. 3.** (a) Reciprocal lattice for a two-dimensional oblique crystal lattice that is rolled into a cylinder and has a cell whose edges *a* and *b* form angle γ (for simplicity, the (*h*00)', (0*k*0)', and (*hk*0)' nodes that are symmetric to the (*h*00), (0*k*0), and (*hk*0) nodes, respectively, about the nanotube axis are not shown). The three-dimensional lattice is obtained adding the *Z** axis perpendicular to the figure plane. The coordinates $D_{h00}$ and $S_{h00}$ of the (*h*00) node, as well as the coordinates $D_{0k0}$ and $S_{0k0}$ of the (0*k*0) node, are shown for determining the coordinates $D_{hk0}$ and $S_{hk0}$ of the (*hk*0) node. (b) The chiral-angle dependence of the characteristics of the splitting between the nodes [$\Delta S(\bar{1}20)$, (110) and $\Delta D(\bar{1}20)$, (110)] $(\bar{1}20)'$ and (110) and [$\Delta S(\bar{1}10)$, (100) and $\Delta D(\bar{1}10)$, (100)] $(\bar{1}10)'$ and (100), as well as the chiral-angle dependence of the distances ΔS(010), (100) and ΔD(010), (100) between the (010) and (100) nodes.

In terms of the coordinates $S_{hk0}$ and $D_{hk0}$, the splitting between the $(h_1k_10)$ and $(h_2k_20)'$ reflections (Fig. 2b) that depends on the chiral angle is characterized by the quantities

$$|\Delta S| = |\Delta S(h_1k_10), (h_2k_20)| = \left||S_{h_1k_10}| - |S_{h_2k_20}|\right|,$$

$$|\Delta D| = |\Delta D(h_1k_10), (h_2k_20)| = \left||D_{h_1k_10}| - |D_{h_2k_20}|\right|,$$

where the parameters for the $(h_2k_20)'$ node are determined by the $(h_2k_20)$ node symmetric about the rotation axis. Using expressions (1) and (2), we obtain

$$|\Delta S| = \left|\left|\frac{h_1}{2.13}\cos(60+\alpha) + \frac{k_1}{2.13}\cos\alpha\right| - \left|\frac{h_2}{2.13}\cos(60+\alpha) + \frac{k_2}{2.13}\cos\alpha\right|\right|, \quad (3)$$

$$|\Delta D| = \left|\left|\frac{h_1}{2.13}\sin(60+\alpha) + \frac{k_1}{2.13}\sin\alpha\right| - \left|\frac{h_2}{2.13}\sin(60+\alpha) + \frac{k_2}{2.13}\sin\alpha\right|\right|. \quad (4)$$

Figure 3b shows the ΔS and ΔD quantities that are calculated by Eqs. (3) and (4), respectively, and characterize the splitting between the $(\bar{1}20)$ and (110) nodes, as well as between the $(\bar{1}10)$ and (100) nodes, as functions of the chiral angle α in comparison with these quantities for a pair of (100) and (010) nodes lying on the *X** and *Y** axes, respectively. Since these nodes are asymmetric about the *Y** axis, the initial ΔS and ΔD values (for α = 0°) are not equal to zero, unlike these quantities for the $(\bar{1}20)$ and (110) nodes, as well as for the $(\bar{1}10)$ and (100) nodes, symmetric about the *Y** axis. The quantities $D_{hk0}$, $S_{hk0}$, ΔD, and ΔS calculated for the reciprocal lattice are represented in an electron diffraction pattern by the distances

$$r\,(\text{mm}) = R\,(\text{Å}^{-1}) \cdot C\,(\text{Å mm}), \quad (5)$$

where *R* is any of the above quantities and *C* is the electron-microscope constant determining the electron-pattern scale.

To illustrate one of the possible applications of the proposed coordinates of nodes in the reciprocal lattice of the nanotube, we find the chiral angle of an arbitrary nanotube by using the $S_{hk0}$ coordinate. Let us consider the electron diffraction pattern of a multiwall nanotube with a diameter of about 190 nm, shown in Fig. 4a [5]. The standard procedure of determining the chiral angle implies measurement of the angle between the radius vectors of the split reflections $(\bar{2}10)'$ and $(2\bar{1}0)$ or $(\bar{2}10)$ and $(2\bar{1}0)'$, because these reflections are closest to the equatorial line of the electron diffraction pattern and, therefore, the procedure of measuring the angle on these reflections is most independent of the strands that are parallel to the equatorial line and always correspond to the diffraction patterns of tube structures. It is impossible to measure the chiral angle between the radius vectors of the (010) and (010)' reflections by the standard method, because their positions are indefinite due to the presence of strands (Fig. 4a). However, using the quantity $S_{hk0}$ given by Eq. (2), one can measure the chiral angle on the basis of an arbitrary reflection including the extended (010) reflection. Indeed, since the parameter $S_{010}$ shows the distance from the zeroth node to the straight line that is perpendicular to the rota-

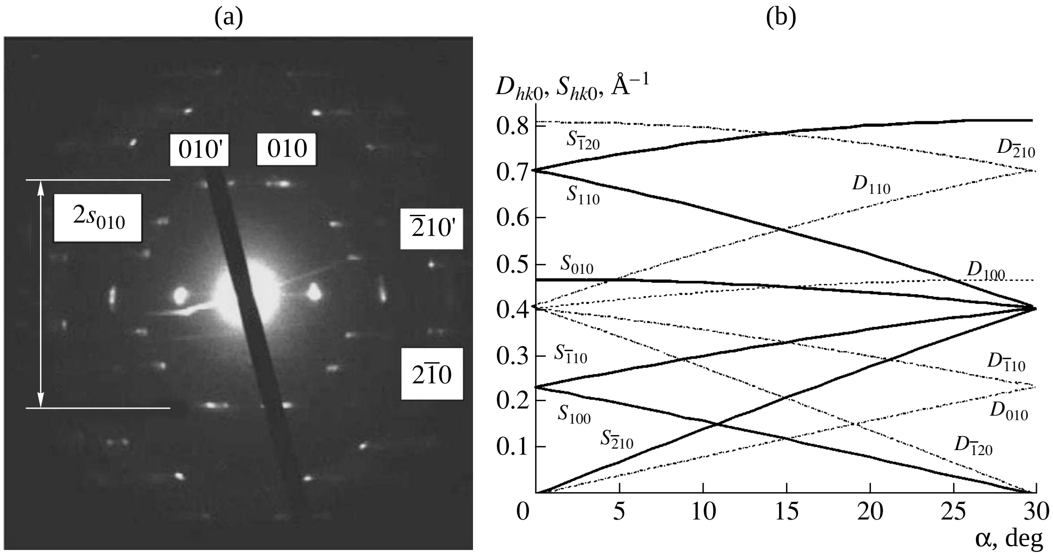

**Fig. 4.** (a) Electron diffraction pattern of the multiwall monochiral carbon nanotube [5], where the double distance $s_{010}$ presenting the parameter $S_{010}$ on the electron diffraction pattern is marked, and (b) $D_{hk0}(\alpha)$ and $S_{hk0}(\alpha)$ plots drawn by using Eqs. (1) and (2) for the (100), (010), $(\bar{1}10)$, (110), $(\bar{1}20)$, and $(\bar{2}10)$ reflections.

tion axis and passes through the (010) node, the $S_{010}$ value is independent of the position of the node on the straight line and, therefore, on the strands. At the same time, the $S_{010}$ value is uniquely related to the chiral angle. Therefore, calculating the $S_{010}$ value for the (010) reflection from the electron diffraction pattern of the nanotube, one can uniquely determine the chiral angle of the nanotube by formula (2).

Calculating the device constant from the reflections of the {110} family and using Eq. (5) with $R$ (Å$^{-1}$) = $S_{010}$ (Å$^{-1}$) and $r$ (mm) = $s_{010}$ (mm) (electron diffraction pattern in Fig. 4), we obtain $S_{010} = 0.462$ Å$^{-1}$ and then the chiral angle $\alpha = 10° \pm 0.1°$ by formula (1). The same value is obtained by measuring $S_{hk0}$ but on the $(2\bar{1}0)$ reflection, and a close value of $9.7° \pm 0.3°$ was obtained in [5] by using the standard procedure for measuring the chiral angle. Figure 4b shows the $S_{hk0}(\alpha)$ and $D_{hk0}(\alpha)$ plots drawn by using Eqs. (1) and (2) for the (100), (010), $(\bar{1}10)$, (110), $(\bar{1}20)$, and $(\bar{2}10)$ reflections. In particular, calculation of $S_{hk0}$ values from the electron diffraction pattern for these reflections makes it possible to uniquely determine the chiral angle of the nanotube from the $S_{hk0}(\alpha)$ dependence.

Calculation of the chiral angle by formula (2) with the use of the $S_{hk0}$ coordinate (or determination of this quantity from plots shown in Fig. 4) is favorable over the standard procedure of measuring the chiral angle for the following reasons. First, the chiral angle α is determined from the position of only one of the split reflections. Second, the chiral angle α is calculated from an arbitrary reflection, e.g., (010), while the extension of the (010) and (010)' reflections makes it impossible to measure the chiral angle by the standard procedure. Third, the accuracy of the determination of the angle increases, because the accuracy becomes independent of the extension of reflections that is always present on the electron diffraction patterns of nanotubes and is directed along the equatorial line of an electron diffraction pattern.

In summary, the behavior of the basic crystallographic characteristics of a nanotube (chiral directions, rotation axis direction, and chiral angle α) has been considered. The parameters $D_{hk0}(\alpha)$, $S_{hk0}(\alpha)$, $\Delta D(\alpha)$, and $\Delta S(\alpha)$ have been introduced that provided the complete quantitative characteristic of the positions of the ($hk$0) nodes in the reciprocal lattice of a carbon nanotube with arbitrary chirality. To increase the measurement accuracy and to provide the possibility of using one arbitrary reflection for calculation of the chiral angle of the nanotube, the use of the parameter $S_{hk0}(\alpha)$ has been proposed.

## REFERENCES

1. L. A. Bursill, J.-L. Peng, and X.-D. Fan, Philos. Mag. **71**, 1161 (1995).
2. S. Roche, T. Francois, R. Angel, and M. Didier, Phys. Lett. A **285**, 94 (2001).
3. H. Yorikawa and S. Muramatsu, Phys. Rev. B **50**, 12203 (1994).
4. K. W. Andrews, D. J. Dyson, and S. R. Keown, *Interpretation of Electron Diffraction Patterns*, 2nd ed. (Hilger, London, 1971; Mir, Moscow, 1971).
5. W. Ruland, A. K. Schaper, H. Hou, and A. Greiner, Carbon **41**, 423 (2003).

*Translated by R. Tyapaev*

*Doklady Physics, Vol. 49, No. 5, 2004, pp. 266–269. Translated from Doklady Akademii Nauk, Vol. 396, No. 2, 2004, pp. 174–177.*

**PHYSICS**

# Effect of Self-Sustained Oscillations on Critical Fluctuations

**N. I. Vaganova*, O. D. Vaganova*, and É. N. Rumanov**

Presented by Academician A.G. Merzhanov January 8, 2004

Received January 27, 2004

As is known [1, 2], the space of the parameters of an exothermic flow reactor includes a bistability region, where either a low- or high-temperature stationary regime is realized, depending on the initial conditions. The boundary of this region has a cusp, where the difference between regimes disappears. The properties of the cusp are similar to those of a critical point on the phase diagram of a substance with the first-order phase transition between the phases with the same symmetry [3]. In particular, it is the endpoint of the equilibrium line between a liquid and vapor (boiling curve) on the pressure–temperature plane, where the bistability domain is bounded by a spinodal. Fluctuations of the reaction rate must be large near the cusp [4] the same as density fluctuations increase near the critical point. At the same time, this similarity is not universal: the stationary regimes of a reactor lose stability for certain parameter values and become periodic [5–7]. In [4], an increase in fluctuations was calculated in the linear approximation and disregarding the oscillation mode. In this work, critical fluctuations are analyzed by numerical simulation for the conditions when they cannot be treated as small, as well as upon the transition from the stationary regime to the periodic one at the cusp.

**1.** The reactor state is determined by three parameters [8] such as the Damköhler number $D$, which is the ratio of the substance residence time in the reactor to the characteristic reaction time $\tau_R$; the Semenov number, which is the ratio of the heat-exchange time of the reactor with the environment to $\tau_R$; and the Zel'dovich number

$$Z = E\frac{T_b - T_0}{T_b^2}, \quad T_b = T_0 + \frac{Q}{c}. \tag{1}$$

Here, $E$ is the activation energy, $T_0$ is the ambient temperature, $Q$ is the reaction heat, and $c$ is the specific heat. Near the cusp, the boundary of the bistability domain is determined by the formula

$$s = \frac{d}{2} \pm \frac{\sqrt{2}}{3}(-d)^{3/2}. \tag{2}$$

Here, $s = SS_c^{-1} - 1$ and $d = DD_c^{-1} - 1$, where the subscript $c$ refers to the parameters at the cusp. For $d < 0$, the phase-equilibrium line $s = \frac{d}{2}$ corresponds to the zero velocity of switching waves in the reactor [9]. Outside the bistability section for $d > 0$, this straight line is similar to the critical isochore for the van der Waals equation. Along the $s = \frac{d}{2}$ straight line to the cusp, the average square of reaction-rate fluctuations increases as $\frac{1}{d}$ in the linear approximation [10]. For numerical simulation, we use the set of equations

$$\dot{\eta} = \Phi(\eta, \theta) - \eta\left[\frac{1}{D} + \frac{1}{D_c}y(t)\right], \tag{3}$$

$$\dot{\theta} = Z\Phi - \frac{\theta + Z}{S}, \tag{4}$$

where the dots stand for differentiation with respect to time, the time unit is equal to $\tau_R(T_b)$, $\eta$ is the reaction product concentration, $\Phi = (1 - \eta)e^{\theta}$, and $\theta$ is the dimensionless temperature measured from $T_b$ in the $\frac{T_b^2}{E}$ units so that $\eta_c = \frac{1}{2}$, $\theta_c = 2 - Z$, $D_c = \exp(Z - 2)$, and $S_c = \frac{4D_c}{Z}$. The cusp corresponds to the equality of the reaction rate to the inverse time of substance residence in

---

*Institute of Structural Macrokinetics and Materials Science, Russian Academy of Sciences, Chernogolovka, Moscow oblast, 142432 Russia*
** e-mail: ed@ism.ac.ru*

the reactor. The random function $y(t)$ takes a value in the interval (–0.1, 0.1) with $\langle y^2 \rangle = \frac{1}{150}$ and simulates small variations in the mixture-feed rate. In calculations by the RKF45 subroutine, $y$ is generated by the RANDOM generator of the FORTRAN 77 compiler. The function $\Phi(t)$ is analyzed for $d$ from the interval (–0.1, 0.1) and $s = \frac{d}{2}$.

**2.** For $y = 0$, the transition from the stationary regime to the periodic one at the cusp occurs at $Z = 8$. First, we analyze the effect of noise $y(t)$ for $Z = 7$ on stationary regimes. The time of establishing such a regime increases upon approaching the cusp. For this reason, the initial conditions $\eta = \eta_c$ and $\theta = \theta_c$ are used to minimize the establishing time. The computation time is equal to $3 \times 10^5$ in most variants, and the establishing time (without noise) does not exceed 2000. The average $\langle \Phi \rangle$ is a decreasing function of $d$ (Fig. 1), because temperature $\theta \approx \theta_c$ on the $s = \frac{d}{2}$ straight line and the product concentration increases with $d$. Susceptibility can be introduced for the stationary regimes of the active system as it is for a system in equilibrium. In particular, the susceptibility of a reactor can be defined as $\left|\frac{\partial \Phi}{\partial D}\right|$. It is seen that this quantity has a sharp maximum at the cusp. The origin of this maximum is the same as the origin of high susceptibility in continuous phase transitions. For $d \ll 1$, the stationary regime is stable under infinitely small perturbations, but the "force" restoring the system to the stable point after deviation is small. For this reason, deviations arise easily and relax slowly. In other words, susceptibility is high in the low-frequency limit, which is given by the above partial derivative.

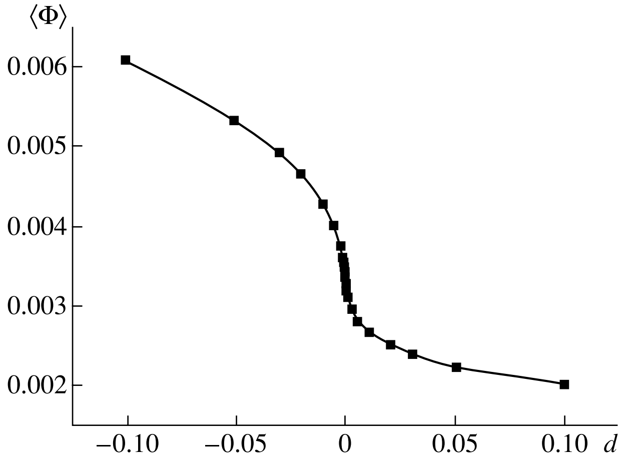

**Fig. 1.** Reaction rate vs. the Damköhler number near the cusp.

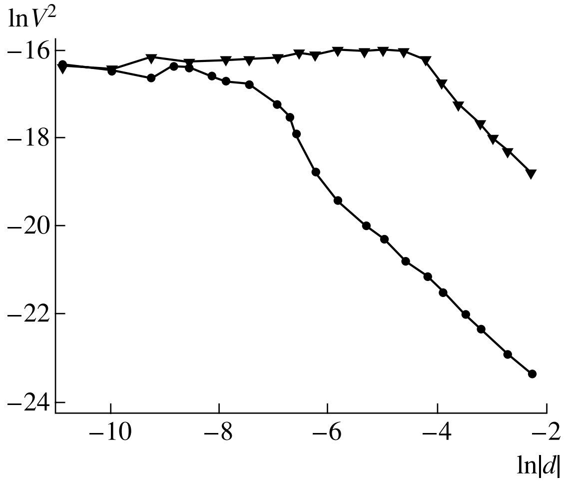

**Fig. 2.** Average square of pulsations against $|d|$ in the double logarithmic scale.

Small random variations of the parameters that are inherent in any real system do not noticeably affect its state far from the bifurcation points. However, near the cusp, where susceptibility is high, weak noise $y(t)$ induces intense pulsations of the reaction rate. Figure 2 shows variation of the variance $V^2 = \langle (\Phi - \langle \Phi \rangle)^2 \rangle$ along the $s = \frac{d}{2}$ straight line in the double logarithmic scale. The upper and lower branches of the plot refer to negative and positive $d$ values, respectively. Upon approaching the point $(D_c, S_c)$, a power increase with the critical exponent $\gamma$ close to –1 is observed. A least squares fit yields $\gamma_- \approx -1.2$ and $\gamma_+ \approx -1.1$ for the upper and lower branches, respectively. The ratio $\frac{V_-}{V_+} \approx \sqrt{56}$, while the average square of fluctuations of the order parameter in the symmetric phase for second-order phase transitions is twice as large as that in the asymmetric phase. An increase in pulsations stops near the cusp similarly to the case of continuous phase transitions, where this behavior is attributed to the nonsingular part of susceptibility. The saturation-region boundaries are $d_- \approx 0.02$ and $d_+ \approx 5 \times 10^{-4}$. The pulsation intensity $\sqrt{V^2}$ in this region is less than $\langle \Phi \rangle$ by a factor of only 3–5, which is similar to the variance-to-mean value ratio for developed turbulence. In [11], the nonlinear saturation of fluctuations for the bifurcation of period doubling is numerically simulated upon a point mapping, as well as for an oscillator with spontaneous symmetry violation (transition from one potential well to two wells; only the symmetric region of the bifurcation parameter was analyzed).

According to [10], the spectra of pulsations generated by weak white noise must have a peak at zero frequency, and the peak width decreases upon approaching the cusp. Figure 3 shows certain frequency spectra.

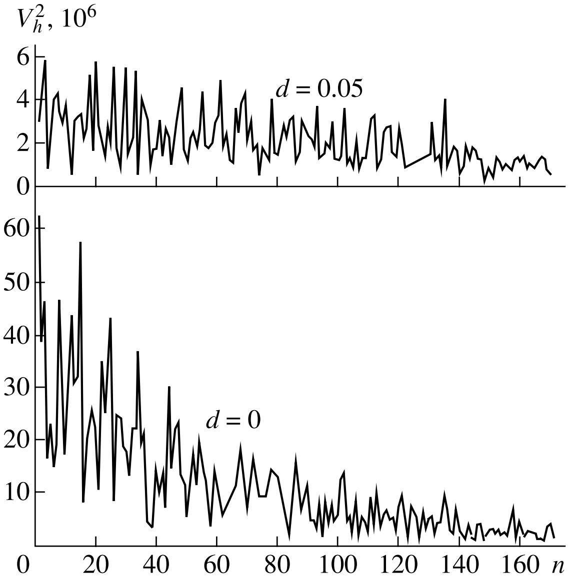

**Fig. 3.** Frequency spectra of pulsations for $d = 0.05$ and 0. The low-frequency peak narrows with a decrease in $d$.

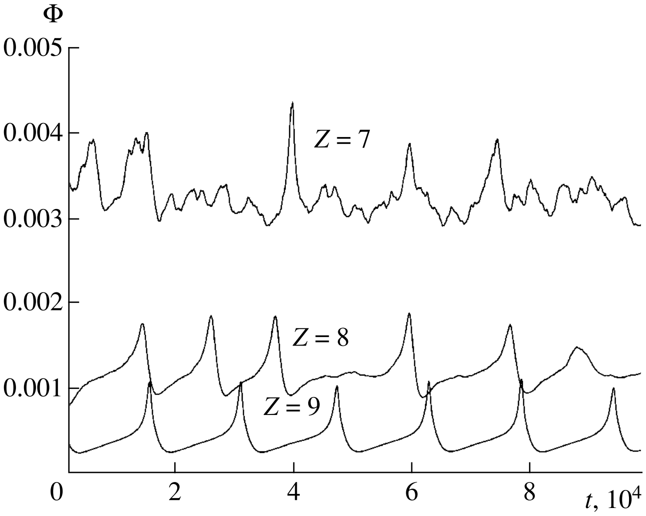

**Fig. 4.** Change in the $\Phi(t)$ plot when exciting self-sustained oscillations as calculated for $d = 0$.

Since the computation time is finite, these spectra are formally line spectra with line frequencies $\omega_n = \frac{2\pi n}{t_0}$, where $n = 1, 2, \ldots$, and $t_0$ is the computation time. The computation time must be much larger than the characteristic oscillation times in $\Phi(t)$, which is ensured by the above $t_0$ value. Intensity is chaotically distributed over the lines but decreases in average with an increase in frequency. The spectrum is shifted towards low frequencies for $d \to 0$ due to an increase in the correlation time of fluctuations. Therefore, their statistical properties are independent of initiating noise, because any external noise can be treated as δ correlated, or white, noise at such long times. At the same time, in contrast to flicker noise, the low-frequency peak is formed only near the cusp. Diagnostics of weak noise that is based on its enhancement by a system under critical conditions was proposed in [11]. Since the height of the plateau in Fig. 2 is the property of the enhancing system, the possible enhancement of initial noise is larger for weaker noise. However, as was stated above, only low frequencies are enhanced, which considerably restricts the possibilities of diagnostics. At the same time, an increase in low-frequency noise of the system, whose parameters can vary, in advance indicates approaching a critical (emergency) situation.

Only the randomization of stationary regimes was considered above. For $Z = 8$, the stationary regime at the cusp loses stability and becomes periodic. The transition to self-sustained oscillations (Fig. 4) suppresses chaotic pulsations. A decrease in $\langle\Phi\rangle$ is attributed to a decrease in the critical temperature $\theta_c = 2 - Z$, whereas the order of magnitude of the amplitude does not change when chaotic oscillations are transformed to regular oscillations. This transition can be attributed to the synchronization of frequencies, or, in other words, to the "condensation" of vibrational modes of the chaotic regime.

**3.** High susceptibility near the bifurcation points (including the points of the continuous phase transition) is responsible for critical phenomena. Susceptibility increases due to smallness of the force restoring the system to the stationary regime or equilibrium after deviation. In the state space, equilibrium or the stationary state corresponds to a point where trajectories converge. Under critical conditions, the attraction basin to the attractor point is small (at least in certain directions), because unstable elements of the state space (saddle points, unstable cycles, etc.) approach it. Thus, almost indifferent equilibrium with a weak restoring force arises. In this work, a reactor is considered as a system with lumped parameters. In a distributed system, pulsations may be inhomogeneous (chaotic autowaves), and their spatial correlations also have singularities under critical conditions.

## ACKNOWLEDGMENTS

We are grateful to A.G. Merzhanov for discussion of the results. This work was supported by the Russian Foundation for Basic Research (project no. 01-03-32772).

## REFERENCES

1. D. A. Frank-Kamenetskiĭ, Dokl. Akad. Nauk SSSR **30**, 729 (1941).
2. Ya. B. Zel'dovich, Zh. Tekh. Fiz. **11**, 493 (1941).

3. A. G. Merzhanov and É. N. Rumanov, Usp. Fiz. Nauk **151**, 553 (1987) [Sov. Phys. Usp. **30**, 293 (1987)].
4. É. N. Rumanov, Dokl. Akad. Nauk **336**, 339 (1994) [Phys. Dokl. **39**, 339 (1994)].
5. D. A. Frank-Kamenetskiĭ and I. E. Sal'nikov, Zh. Fiz. Khim. **17**, 79 (1943).
6. R. Aris and N. R. Amundson, Chem. Eng. Sci. **7**, 121 (1958).
7. D. A. Vaganov, N. M. Samoilenko, and V. G. Abramov, Chem. Eng. Sci. **33**, 1133 (1978).
8. D. A. Frank-Kamenetskiĭ, *Diffusion and Heat Transfer in Chemical Kinetics* (Nauka, Moscow, 1967), p. 339.
9. A. G. Merzhanov, V. V. Barelko, I. I. Kurochka, and K. G. Shkadinskiĭ, Dokl. Akad. Nauk SSSR **221**, 1114 (1975).
10. A. Yu. Dovzhenko, M. Dovzhenko, L. B. Mashkinov, and É. N. Rumanov, Dokl. Akad. Nauk **388**, 181 (2003) [Dokl. Phys. **48**, 13 (2003)].
11. Yu. A. Kravtsov and E. D. Surovyatkina, Phys. Lett. A **319**, 348 (2003).

*Translated by R. Tyapaev*

*Doklady Physics, Vol. 49, No. 5, 2004, pp. 270–274. Translated from Doklady Akademii Nauk, Vol. 396, No. 2, 2004, pp. 178–182.*
*Original Russian Text Copyright © 2004 by Kravchenko, Basarab.*

**PHYSICS**

# Generalized Method of Eigenmodes and *R* Function in Problems of Wave Diffraction

**V. F. Kravchenko* and M. A. Basarab****

Presented by Academician Yu.V. Gulyaev January 28, 2004

Received January 28, 2004

In this study, a new hybrid method for solving a wide range of internal and external problems of diffraction theory is proposed and substantiated on the basis of concepts described in [1–5]. It is well known that the generalized eigenmode method is based on solving a certain auxiliary eigenvalue problem in a complex region by expanding the solution in the basis functions and then finding the coefficients of this series by one of the variational methods. The basis functions must satisfy certain requirements, in particular, boundary conditions. For a region of an arbitrary shape, the choice of the basis can be a complicated task. However, this task is efficiently solved by the method based on the theory of *R* functions [1–4].

## STATEMENT OF THE PROBLEM AND A METHOD OF ITS SOLUTION

**Closed cavity.** We analyze diffraction of electromagnetic waves by a dielectric body placed in a closed cavity. Let the function $U$ satisfy the equations

$$\Delta U + k^2 \varepsilon U = f, \tag{1}$$

$$\Delta U + k^2 U = f \tag{2}$$

and the matching conditions

$$U^+ - U^-\big|_{\partial\Omega^+} = 0, \quad \left(\frac{\partial U^+}{\partial \mathbf{n}} - \frac{\partial U^-}{\partial \mathbf{n}}\right)\bigg|_{\partial\Omega^+} = 0 \tag{3}$$

inside a finite dielectric region $\Omega^+ \subset \Omega$, remaining region $\Omega^- = \Omega \backslash \Omega^+$, and at the dielectric boundary $\partial\Omega^+$, respectively. Here, $\mathbf{n}$ is the external normal vector to $\partial\Omega^+$, whereas $U^+$ and $U^-$ are the $U$ values on either side of $\partial\Omega^+$. The permittivity $\varepsilon$ can be a complex number. The Dirichlet

$$U\big|_{\partial\Omega} = 0, \tag{4a}$$

Neumann

$$\frac{\partial U}{\partial \mathbf{n}}\bigg|_{\partial\Omega} = 0, \tag{4b}$$

or third kind

$$\left(U + w\frac{\partial U}{\partial \mathbf{n}}\right)\bigg|_{\partial\Omega} = 0 \tag{4c}$$

boundary condition is satisfied at the cavity boundary $\partial\Omega$. Here, $w$ is the impedance independent of the frequency $k$. In a particular case, the impedance $w$ can be superconducting. Previously, such a case was analyzed by the generalized eigenmode method by one of us (V.E.K.) in [6, 7]. Let the field $U^0$ satisfy the equation

$$\Delta U^0 + k^2 U^0 = f \tag{5}$$

everywhere in the cavity with the same boundary conditions. In this case, the solution to the diffraction problem specified by Eqs. (1)–(4) can be represented in the form of the series

$$U = U^0 + \sum_n A_n u_n, \tag{6}$$

where $u_n$ are eigenfunctions of the auxiliary homogeneous problem

$$\Delta u_n + k^2 \varepsilon_n u_n = 0 \text{ in } \Omega^+, \tag{7}$$

$$\Delta u_n + k^2 u_n = 0 \text{ in } \Omega^- \tag{8}$$

with the matching conditions

$$u_n^+ - u_n^-\big|_{\partial\Omega^+} = 0, \quad \left(\frac{\partial u_n^+}{\partial \mathbf{n}} + \frac{\partial u_n^-}{\partial \mathbf{n}}\right)\bigg|_{\partial\Omega^+} = 0 \tag{9}$$

---

* *Institute of Radio Engineering and Electronics, Russian Academy of Sciences, Mokhovaya ul. 18, Moscow, 103907 Russia*
*e-mail: kravchenko-vf@fromru.com*

** *Bauman Moscow State Technical University, Vtoraya Baumanskaya ul. 5, Moscow, 107005 Russia*
*e-mail: bmic@mail.ru*

and the boundary conditions

$$u_n\big|_{\partial\Omega} = 0, \qquad (10a)$$

$$\left.\frac{\partial u_n}{\partial \mathbf{n}}\right|_{\partial\Omega} = 0, \qquad (10b)$$

or

$$\left.\left(u_n + w\frac{\partial u_n}{\partial \mathbf{n}}\right)\right|_{\partial\Omega} = 0. \qquad (10c)$$

The numbers $\varepsilon_n$ are the eigenvalues of the latter problem, which describes the eigenmodes (in the field free of sources) in a system consisting of a cavity and a dielectric body. Outside the dielectric, the eigenfunctions and diffracted field $U - U^0$ satisfy the same equation. The eigenfunctions of the problem that is given by Eqs. (7)–(9), (10a), and (10b) are orthogonal,

$$\int_{\Omega^+} u_n u_m d\sigma = 0, \quad n \neq m, \qquad (11)$$

$$\int_{\Omega^+} u_n u_m^* d\sigma = 0, \quad n \neq m, \qquad (12)$$

and the eigenvalues $\varepsilon_n$ are real. If boundary condition (10c) with the complex impedance $w$, $\operatorname{Im} w < 0$ (absorbing walls) is given on $\partial\Omega$, then the homogeneous problem for $u_n$ is not self-conjugate, the eigenvalues $\varepsilon_n$ are complex, and only relationship (11) is valid. When energy losses exist, eigenmodes are possible only if energy is released in the dielectric. In this case, the imaginary part of $\varepsilon$ must be positive, whereas the energy released in the dielectric body must be identical to the energy absorbed by the walls. In order to determine $\varepsilon_n$, we should vary the functional

$$L(u) = \int_{\Omega}(\nabla u)^2 d\sigma - k^2\int_{\Omega^-} u^2 d\sigma - k^2\varepsilon\int_{\Omega^+} u^2 d\sigma, \qquad (13)$$

where $\varepsilon$ plays the role of the Lagrange multiplier. Representing $u_n$ as the following series in terms of the basis functions $\varphi_m$ that satisfy boundary conditions (10),

$$u_n = \sum_m C_m^{(n)}\varphi_m \qquad (14)$$

and applying the Ritz method to functional (13), we arrive at the algebraic eigenvalue problem

$$\sum_m a_{ml}C_m^{(n)} = \varepsilon_n\sum_m b_{ml}C_m^{(n)}, \qquad (15)$$

where

$$a_{ml} = \int_{\Omega}\nabla\varphi_m\nabla\varphi_l d\sigma - k^2\int_{\Omega^-}\varphi_m\varphi_l d\sigma,$$

$$b_{ml} = k^2\int_{\Omega^+}\varphi_m\varphi_l d\sigma.$$

The solution to the initial problem given by Eqs. (1)–(4) is expressed in form (6), where

$$A_n = \frac{1}{\varepsilon - \varepsilon_n}\frac{1-\varepsilon}{k^2(1-\varepsilon_n)}\frac{\int_{\Omega} u_n f d\sigma}{\int_{\Omega^+} u_n^2 d\sigma}. \qquad (16)$$

For a region of a complicated shape, the method of *R* functions makes it possible to construct the basis functions $\varphi_m$ in Eq. (14) that exactly satisfy homogeneous boundary conditions (10). In this case, the right-hand side of (14) can be considered as a solution to the boundary value problem that contains indeterminate coefficients $C_m^{(n)}$. These coefficients are found by minimizing functional (13). Let the equation for the domain $\Omega$ be constructed by the method of *R* functions (we assume that $\Omega \subset R^2$)

$$\omega(x, y) = 0, \qquad (17)$$

such that $\omega > 0$ and $\omega < 0$ inside and outside $\Omega$, respectively, and $\omega = 0$ on $\partial\Omega$. In the case of boundary conditions of the second or third kind, we also require that the function $\omega$ be normalized, i.e., $\left.\frac{\partial\omega}{\partial\mathbf{n}}\right|_{\partial\Omega} = -1$. We choose an arbitrary system of functions $\psi_n$ that is complete in $\Omega$. Then, the basis functions $\varphi_n$ that appear in Eq. (14) and exactly satisfy boundary conditions (10) have the form

$$\varphi_n = \omega\psi_n, \qquad (18a)$$

$$\varphi_n = \psi_n - \omega D\psi_n, \qquad (18b)$$

$$\varphi_n = \psi_n - \omega\left(D\psi_n - \frac{\psi_n}{w}\right). \qquad (18c)$$

Here,

$$D \equiv \frac{\partial\omega}{\partial x}\frac{\partial}{\partial x} + \frac{\partial\omega}{\partial y}\frac{\partial}{\partial y}$$

is the differential operator that, at the boundary $\partial\Omega$, coincides with the operator of the differentiation with respect to the outer normal. In expression (18c), $w$ is continued from the boundary to the interior of the domain.

**Open cavity.** Let us consider diffraction by the dielectric body located in vacuum or in an open cavity. In this case, the scattered field $U - U^0$ must satisfy the radiation condition. Therefore, the modification of the $\varepsilon$ method for open problems is reduced to introducing the radiation conditions into the homogeneous problem. The mathematical formulation of the diffraction problem is the following. We need to find the function $U$ satisfying Eqs. (1), (2), and (3) within the region $\Omega^+$ (the interior of a dielectric body), infinite region $\Omega^-$, and at the boundary of the dielectric body, respectively. If the sources are situated at finite distances, the radiation condition at infinity is

$$U \sim \frac{e^{-ikr}}{\sqrt{r}}\Phi(\varphi). \qquad (19)$$

For a plane wave incident on the body, the radiation condition is imposed on the scattered field. As before, we seek the solution to the problem under consideration in the form of series (6), where $U^0$ is the field of the same sources $f$ in vacuum (primary or incident field); i.e., $U^0$ satisfies Eq. (5) in the entire volume. The eigenfunctions $u_n$ in the expansion of the diffracted field $U - U^0$ must obey Eqs. (7) and (8), boundary conditions (9) of the continuity of the field and its normal derivative on $\partial\Omega^+$, and the radiation conditions at infinity. The numbers $\varepsilon_n$ are eigenvalues of the formulated homogeneous problem. Since each eigenfunction outside the body satisfies the same equation as the scattered field, each term and all of series (6) satisfy the radiation condition. For a fixed frequency $k$, the homogeneous problem has a nontrivial solution only at certain values of $\varepsilon_n$ and the imaginary part of the eigenvalue must be positive, i.e., $\mathrm{Im}\varepsilon_n > 0$. This property of $\varepsilon_n$ has the same physical explanation as for a cavity with impedance walls: undamped eigenmodes in the presence of radiation can exist only when they are maintained by the energy released in an auxiliary body. It follows from the statement of the homogeneous problem that series (6) with arbitrary coefficients $A_n$ obeys Eq. (2) outside the body, the boundary conditions on $\partial\Omega^+$, and the radiation condition. The coefficients $A_n$ are of form (16).

Radiation condition (19) can be written as the asymptotic form of impedance condition (10c) for $w = -\frac{i}{k}$. Therefore, besides the radiation condition imposed on the admissible functions, it is necessary to add the integral of $u\frac{\partial u}{\partial \mathbf{n}}$ over an infinite sphere to Eq. (13). Indeed, it can be shown that the first variation of the functional

$$L_R(u) = \int\limits_{\Omega^+}[(\nabla u)^2 - k^2\varepsilon u^2]d\sigma$$

$$+ \int\limits_{\Omega^-}[(\nabla u)^2 - k^2u^2]d\sigma + \int\limits_{S_R}u\frac{\partial u}{\partial \mathbf{n}}d\sigma, \qquad (20)$$

where $\Omega^-$ is the domain externally bounded by the sphere $S_R$ of radius $R$, has the order $\frac{1}{R}$ on the eigenfunction of the homogeneous problem. Therefore, the first variation of the functional

$$L(u) = \lim_{R\to\infty} L_R(u) \qquad (21)$$

is zero; i.e., $L(u)$ is the desired functional. Instead of functional (20), we can minimize the simpler functional

$$L(u) = \int\limits_{\Omega^+}[(\nabla u)^2 - k^2\varepsilon u^2]d\sigma$$

$$+ \int\limits_{\Omega^-}[(\nabla u)^2 - k^2u^2]d\sigma, \qquad (22)$$

where $\Omega^-$ is the infinite region but for complex $k$ ($\mathrm{Im}k < 0$). After the integral over $\Omega^-$ has been calculated, $k$ must again be considered as real.

The method of $R$ functions in external diffraction problems is realized by approximately simulating the radiation conditions

$$\left(\frac{\partial u}{\partial \mathbf{n}} - iku + \frac{u}{2R}\right)_{S_R} = 0 \qquad (23)$$

on the auxiliary contour $S_R$. Taking into account that the normalized equation for the contour $S_R$ is of the form

$$\omega_R(x, y) = \frac{R^2 - x^2 - y^2}{2R},$$

we may write the following approximate structure of the solution to the diffraction problem for an open cavity:

$$u_n = \psi_n - \omega_R\left[D^R\psi_n - \left(\frac{1}{2R} - ik\right)\psi_n\right], \qquad (24)$$

where

$$D^R \equiv \frac{\partial\omega_R}{\partial x}\frac{\partial}{\partial x} + \frac{\partial\omega_R}{\partial y}\frac{\partial}{\partial y} = -\frac{1}{R}\left(x\frac{\partial}{\partial x} + y\frac{\partial}{\partial y}\right).$$

## AN EXAMPLE OF NUMERICAL REALIZATION

We now analyze the diffraction problem in a closed H-shaped cavity with metallic walls and a dielectric insert (Fig. 1). The eigenmodes of the homogeneous problem of the $\varepsilon$ method satisfy Eqs. (7) and (8) in the domain $\Omega^+$ occupied by a dielectric and the remaining domain of the cavity, respectively, as well as continuity condition (9) and boundary condition (10a) on the cavity walls ($E$ polarization). In order to realize the method of $R$ functions, we initially construct the boundary function of the $\Omega$ domain:

$$\omega(x, y)$$

$$= [(b^2 - x^2) \wedge_0 (L^2 - y^2)] \wedge_0 [(x^2 - a^2) \vee_0 (l^2 - y^2)], \qquad (25)$$

where $\wedge_0$ and $\vee_0$ are the symbols of the $\mathfrak{R}_0$ conjunction

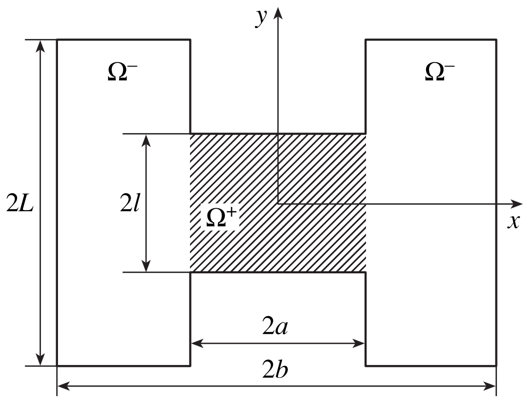

**Fig. 1.** Cross section of an H-shaped cavity.

and $\mathfrak{R}_0$ disjunction defined as

$$f_1 \wedge_0 f_2 \equiv f_1 + f_2 - \sqrt{f_1^2 + f_2^2}, \qquad (26)$$

$$f_1 \vee_0 f_2 \equiv f_1 + f_2 - \sqrt{f_1^2 + f_2^2}, \qquad (27)$$

respectively. Furthermore, we use the Ritz method for the minimization of functional (13) with basis functions (18a) in expansion (14). We take usual power

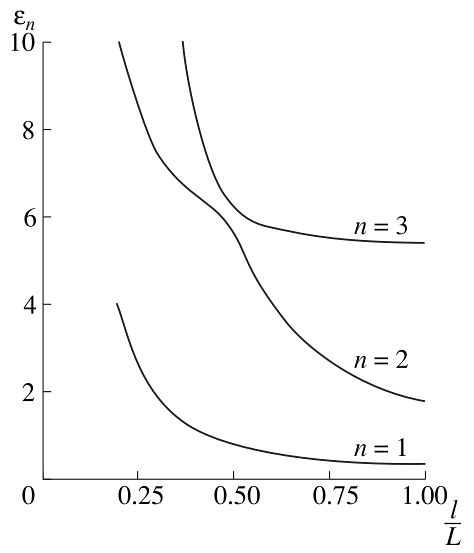

**Fig. 2.** Dependence of the first three eigenvalues $\varepsilon_n$ on the cavity geometric parameter.

polynomials as $\psi_n$ and consider only even powers in $x$ and $y$ (even oscillations). The convergence of the Ritz method was verified numerically by comparing the results obtained for different numbers of basis functions. In the case of 14 basis functions, the error was

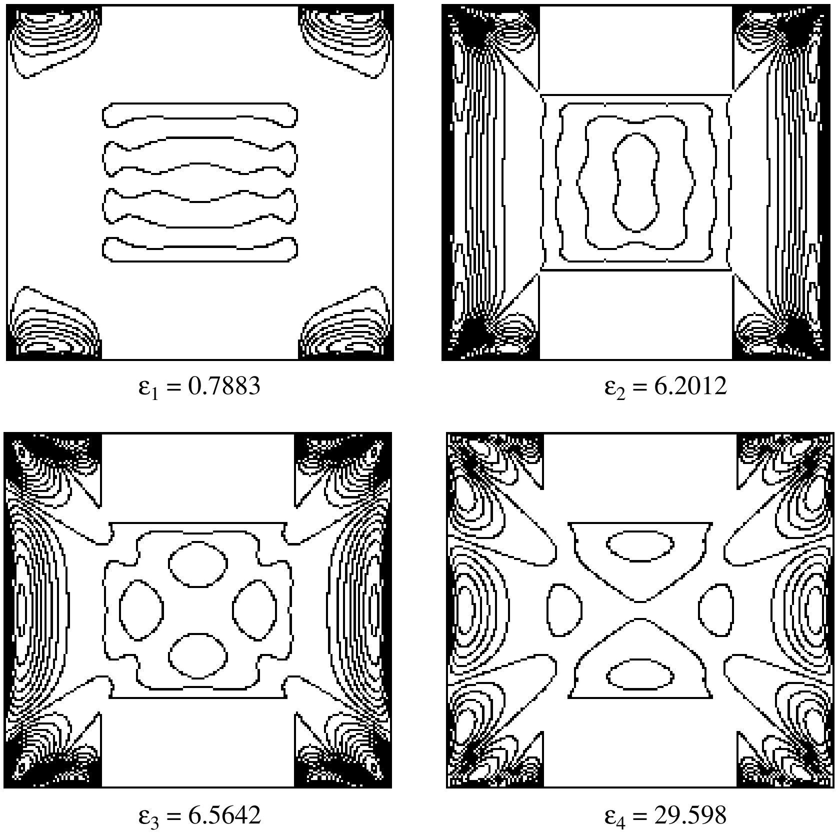

$\varepsilon_1 = 0.7883$ $\varepsilon_2 = 6.2012$

$\varepsilon_3 = 6.5642$ $\varepsilon_4 = 29.598$

**Fig. 3.** Contours of the first four eigenfunctions (for $\frac{l}{L} = 0.5$).

approximately equal to 1%. Figure 2 shows the dependence of the first three eigenvalues $\varepsilon_n$ on the relative width of the dielectric insert for $ka = \sqrt{2}$, $\frac{L}{a} = 3$, and $\frac{b}{a} = 2$. Figure 3 demonstrates contours for the first four eigenmodes corresponding to even (with respect to both coordinates) oscillations. The results agree well with the data of [5], where the solution was obtained by minimizing a functional more complicated than functional (13) on the basis of a variant of the partial-domain method.

Thus, the hybrid method that is proposed and substantiated in this study and involves the constructive possibilities of the *R*-function theory and the generalized eigenmode method is efficient in solving both internal and external diffraction problems. This method can also be applied to solve a wide range of boundary value problems in the electrodynamics of superconducting structures.

## REFERENCES

1. V. L. Rvachev, *Theory of R Functions and Its Certain Applications* (Naukova Dumka, Kiev, 1982).
2. V. F. Kravchenko, *Lectures on the Theory of Atomic Functions and Their Applications* (Radiotekhnika, Moscow, 2003).
3. V. F. Kravchenko and M. A. Basarab, *Boolean Algebra and Approximation Methods in Boundary Value Problems of Electrodynamics* (Fizmatlit, Moscow, 2004).
4. V. F. Kravchenko and M. A. Basarab, Usp. Sovrem. Radioélektron., No. 8, 77 (2003).
5. N. N. Voĭtovich, B. Z. Katsenelenbaum, and A. N. Sivov, *Generalized Method of Eigenmodes in Diffraction Theory* (Nauka, Moscow, 1977).
6. V. F. Kravchenko, Telecommun. Radio Eng. (Engl. Transl.) **54**, 85 (2000).
7. V. F. Kravchenko, in *Proceedings of the International Conference on Mathematical Methods in Electromagnetic Theory, Kharkov, 1998*, Vol. 1, pp. 228–230.
8. V. F. Kravchenko, Dokl. Akad. Nauk SSSR **309**, 594 (1989) [Sov. Phys. Dokl. **34**, 983 (1989)].

*Translated by G. Merzon*

Doklady Physics, Vol. 49, No. 5, 2004, pp. 275–278. Translated from Doklady Akademii Nauk, Vol. 396, No. 3, 2004, pp. 324–327.
Original Russian Text Copyright © 2004 by Nefedov, Yarzhemsky, Nefedova, Szargan.

## PHYSICS

# Determination of the Thickness of Ultrathin Films by X-ray Photoelectron Spectroscopy

**Academician V. I. Nefedov[1], V. G. Yarzhemsky[1,*], I. S. Nefedova[1], and R. Szargan[2]**

Received February 4, 2004

**1.** To modify the surface properties of materials, their surfaces are covered by films. When items made of these materials are used, a layer whose composition and properties differ from those of the respective bulk properties appears on their surface. It is difficult to determine the thickness of such films when they consist of two to ten monolayers. X-ray photoelectron spectroscopy or Auger electron spectroscopy is usually applied in this case. However, except for [1], the elastic scattering of photoelectrons was disregarded in this case. At the same time, this scattering strongly affects the path of a photoelectron in a film and substrate [2–5].

Recently [6–15], it was shown that nondipole transitions accompanying photoionization strongly affect the intensity and angular distribution of photoelectrons. Since the angular distribution is important for determining the thickness of thin films, the effect of nondipole transitions on the determination of the thickness of films is analyzed in this work. In addition, we compare two methods of measuring the photoelectron path in a film: first, by rotation of an analyzer when the angle between ionizing radiation and a sample is constant and, second, by rotation of the sample when the angle between ionizing radiation and photoelectron emission direction is constant.

**2.** To develop a method of determining the thickness of ultrathin films by x-ray photoelectron spectroscopy with allowance for both the elastic scattering of photoelectrons in a solid and nondipole transitions accompanying photoionization, we use the approach described in [1, 2] and complement it by taking into account nondipole transitions. We apply the method to the case of unpolarized ionizing radiation by including only the very important dipole–quadrupole transitions. We begin with the first variant, i.e., with a rotating analyzer, when ionizing radiation normally falls on the sample surface. The method is easily applied to polarized radiation.

In the case under consideration, the differential cross section for photoionization is given by the formula

$$\frac{d\sigma_{nl}}{d\Omega} = \frac{1 - 0.25\beta(3\cos^2\theta - 1) + [0.5\gamma(1-\cos^2\theta) + \delta]\cos\theta}{4\pi}, \qquad (1)$$

where $\Omega$ is the solid angle; $\beta$, $\gamma$, and $\delta$ are the parameters of the angular distribution; and $\theta$ is the angle between ionizing radiation and photoelectron emission direction.

In a pure theoretical approximation similar to [1] (theory I), the intensities from a semi-infinite homogeneous sample and a layer with thickness $d$ are determined as

$$P_\infty = c^2\left[\frac{H}{c} - 0.25\beta(3\mu^2 - 1) - 0.5\gamma(\sin^2\alpha + \delta)\mu\right] \qquad (2)$$

and

$$P_d = Hc\left\{0.5\left[1 - \exp\left(-\frac{d}{\mu c}\right)\right] + \left(\frac{0.5}{\nu - \mu}\right) \times\left[(\nu c - \mu)\left(1 - \exp\left(-\frac{d}{\mu c^2}\right)\right) + \nu(1 - c)\left(1 - \exp\left(-\frac{d}{\nu c^2}\right)\right)\right]\right\} - \left(1 - \exp\left(-\frac{d}{\mu c^2}\right)\right) \times [0.25\beta c^2(3\mu^2 - 1) + 0.5c^2\gamma(\sin^2\alpha + \delta)\mu], \qquad (3)$$

---

[1] *Kurnakov Institute of General and Inorganic Chemistry, Russian Academy of Sciences, Leninskiĭ pr. 31, Moscow, 117907 Russia*

[2] *Wilhelm-Ostwald Institut für Physikalische und Theoretische Chemie, Universirät Leipzig, Leipzig, Linnestr 2 D-04103, Germany*

* *e-mail: vgyar@igic.ras.ru*

1028-3358/04/4905-0275$26.00 © 2004 MAIK “Nauka/Interperiodica”

**Table 1.** Values of $f_1$ obtained for the Ag 3*d* line by the rotating-analyzer method

| $d$ | $f_1$ | | | | | | |
|---|---|---|---|---|---|---|---|
| | $\alpha = 2°$ | $\alpha = 14°$ | $\alpha = 32°$ | $\alpha = 50°$ | $\alpha = 62°$ | $\alpha = 74°$ | $\alpha = 80°$ |
| 0.05 | 0.99276 | 0.96828 | 0.90100 | 0.84700 | 0.82479 | 0.81320 | 0.81335 |
| 0.3 | 0.97697 | 0.95573 | 0.89696 | 0.85134 | 0.83745 | 0.85022 | 0.90350 |
| 0.75 | 0.95389 | 0.93706 | 0.89056 | 0.85927 | 0.86447 | 0.96310 | 1.25448 |
| 1.5 | 0.92569 | 0.91369 | 0.88182 | 0.87269 | 0.92084 | 1.23682 | 1.86489 |
| 2 | 0.91158 | 0.90175 | 0.87701 | 0.88167 | 0.96341 | 1.40231 | 2.15050 |
| 3 | 0.89044 | 0.88357 | 0.86920 | 0.89934 | 1.04713 | 1.64091 | 2.54043 |

respectively, where $H = \frac{1 + 1.908\mu}{1 + 1.908\mu c}$ is the Chandrasekhar function, $\mu = \cos\alpha$, $\alpha$ is the photoelectron emission angle, $c = (1 - \omega)^{0.5}$, $\omega$ is the single scattering albedo, $d$ is the layer thickness measured in the inelastic mean free path of a photoelectron in the surface layer and substrate, and $\nu = 1 + 2\exp\left(-\frac{2}{\omega}\right)$.

In the second case (rotating sample), the angle between ionizing radiation and photoelectron emission direction is taken to be 90°, which corresponds to the construction of most spectrometers, i.e., $\mu = 0$. Therefore, the contribution of nondipole parameters $\gamma$ and $\delta$ vanishes in this variant.

Let us determine the thickness of a film by a method similar to that described in [1]. It is based on measuring the ratio of $K_1$ intensities $I_s(d/s)$ from the substrate under the film to the intensity $I_\infty$ of the same x-ray photoelectron line in the pure (without film) semi-infinite sample. This ratio is determined by Eq. (4) with the use of partial contributions $P_d$ and $P_\infty$ to intensity:

$$K_1 = \frac{I_s(d/s)}{I_\infty} = 1 - \frac{P_d}{P_\infty}, \tag{4}$$

where $d$ is the thickness of the surface layer. Intensity $I_s(d/s)$ can be represented in the form

$$I_s(d/s) = I_\infty \exp\left(-\frac{d}{f_1\mu}\right). \tag{5}$$

Here, $\mu = \cos\alpha$, where $\alpha$ is the photoelectron emission angle with respect to the normal to the surface. The attenuation coefficient $f_1$ is not constant and depends on the physical characteristics of the sample and experimental conditions. In essence, Eq. (5) is a definition of the quantity $f_1$. Taking Eqs. (4) and (5) into account, we obtain

$$\frac{d}{f_1} = -\mu\ln\left(1 - \frac{P_d}{P_\infty}\right) = -\mu\ln K_1. \tag{6}$$

The self-consistent determination of layer thickness is carried out as follows. First, the ratio $K_1$ is experimentally determined, and the quantity $\frac{d}{f_1}$ is calculated by Eq. (6). Second, the quantity $f_1$ for a given $\omega$ value and certain estimate $d$ is calculated from the first of Eqs. (6). Third, the quantity $d$ is calculated by using the previously determined values $\frac{d}{f_1}$ and $f_1$. Fourth, similarly to the second step, the $f_1'$ value is calculated with the $d$ value obtained in the third step and, then, a new $d'$ value is determined by using the $f_1'$ value. Fifth, the self-consistent procedure continues until the $d'$ values obtained in steps similar to the third and fourth steps coincide with each other. One or two cycles are usually sufficient.

As was shown in [1], the $f_1$ value is independent of the type of calculation (theory I, II, or III). For this reason, theory I is taken for simplification of expressions. The quantities $P_d$ and $P_\infty$ can be determined not only by analytical calculation but also by the Monte Carlo method. We apply the Monte Carlo method described in [1]. The procedure of determining $d$ is demonstrated for the Ag 3*d* x-ray photoelectron line excited by the Mg$K_\alpha$ line. The parameters necessary for analytical calculation for the Ag 3*d* line are $\omega = 0.31$, $\delta = 0.0469$, $\gamma = 0.181$, and $\beta = 1.21$. The $\delta$, $\gamma$, and $\beta$ values are calculated in the relativistic approximation.

Tables 1 and 2 present $f_1$ values calculated analytically for various $d$ and $\alpha$ values. Experimental data are simulated by the Monte Carlo method. Table 3 presents the $d$ values determined by the three methods and $d$ val-

**Table 2.** Values of $f_1$ obtained for the Ag 3*d* line by the rotating-sample method

| $d$ | $f_1$ | | | | | | |
|---|---|---|---|---|---|---|---|
| | $\alpha = 2°$ | $\alpha = 14°$ | $\alpha = 32°$ | $\alpha = 50°$ | $\alpha = 62°$ | $\alpha = 74°$ | $\alpha = 80°$ |
| 0.05 | 0.80061 | 0.80065 | 0.80081 | 0.80130 | 0.80217 | 0.80488 | 0.80945 |
| 0.3 | 0.79947 | 0.79980 | 0.80145 | 0.80597 | 0.81377 | 0.84020 | 0.89764 |
| 0.75 | 0.79763 | 0.79842 | 0.80255 | 0.81472 | 0.83903 | 0.94950 | 1.24491 |
| 1.5 | 0.79511 | 0.79653 | 0.80425 | 0.83011 | 0.89364 | 1.22051 | 1.85361 |
| 2 | 0.79376 | 0.79551 | 0.80529 | 0.84075 | 0.93619 | 1.38612 | 2.13924 |
| 3 | 0.79170 | 0.79395 | 0.80718 | 0.86221 | 1.02192 | 1.62603 | 2.52994 |

**Table 3.** Values of *d* calculated for the Ag 3*d* line by (first rows) the rotating-analyzer method, (second rows) rotating-sample method, and (third rows) disregarding elastic scattering in comparison with the true *d* values

| True $d$ | $d$ | | | | | | |
|---|---|---|---|---|---|---|---|
| | $\alpha = 2°$ | $\alpha = 14°$ | $\alpha = 32°$ | $\alpha = 50°$ | $\alpha = 62°$ | $\alpha = 74°$ | $\alpha = 80°$ |
| 0.3 | 0.315 | 0.313 | 0.282 | 0.318 | 0.326 | 0.335 | 0.304 |
| | 0.31 | 0.30 | 0.27 | 0.3 | 0.3 | 0.31 | 0.28 |
| | 0.322 | 0.328 | 0.315 | 0.373 | 0.389 | 0.394 | 0.337 |
| 0.75 | 0.692 | 0.701 | 0.816 | 0.788 | 0.806 | 0.755 | 0.720 |
| | 0.67 | 0.67 | 0.75 | 0.73 | 0.75 | 0.69 | 0.65 |
| | 0.726 | 0.748 | 0.916 | 0.917 | 0.933 | 0.784 | 0.574 |
| 1.5 | 1.463 | 1.508 | 1.622 | 1.58 | 1.565 | 1.509 | 1.587 |
| | 1.42 | 1.42 | 1.50 | 1.46 | 1.42 | 1.38 | 1.47 |
| | 1.58 | 1.65 | 1.84 | 1.81 | 1.70 | 1.22 | 0.851 |
| 2 | 2.015 | 2.04 | 2.175 | 2.072 | 2.032 | 2.019 | 2.172 |
| | 1.95 | 1.92 | 2.01 | 1.93 | 1.87 | 1.86 | 1.97 |
| | 2.21 | 2.26 | 2.48 | 2.35 | 2.11 | 1.44 | 1.01 |
| 3 | 3.14 | 3.066 | 3.26 | 3.076 | 3.047 | 3.183 | 3.506 |
| | 3.11 | 2.94 | 3.07 | 2.89 | 2.86 | 2.84 | 3.01 |
| | 3.53 | 3.47 | 3.75 | 3.42 | 2.91 | 1.94 | 1.38 |

ues used in the Monte Carlo calculation, which below will be called true values. This table can be treated as a comparison between theory and experiment.

**3.** Analysis of Table 3 provides the following conclusions.

First, calculation disregarding elastic scattering (the third row for each *d* value in Table 3), which is called the straight line approximation (SLA), because the trajectories of photoelectrons in this case are straight lines, is noticeably less accurate than the first two approaches. Good agreement of the SLA with experimental data is observed only for small *d* values. The SLA overestimates the true *d* values for small α values and strongly underestimates them with an increase in *d*. This result is explained by the results obtained in [5].

Second, for experimental determination of *d*, α angles less than 60° are important, because sample roughness is important for larger α values. In this case, the rotating-analyzer method, where nondipole transitions are taken into account, overestimates both the true *d* values and values given by the rotating-sample method, which underestimates the true *d* values.

Third, deviations of *d* values obtained by the first and second methods from the true values are immaterial. Both methods reproduce the true *d* values well within an accuracy of 6%. Thus, the inclusion of nondipole transitions does not lead to considerable improvement of the results. This conclusion is associated with the structure of formula (6). The contribution of nondipole transitions to the quantities $P_d$ and $P_\infty$ are partially compensated, because only their ratio $\frac{P_d}{P_\infty}$ enters into formula (6).

Conclusions for the Al 2*s* line are similar.

## ACKNOWLEDGMENTS

This work was supported by the Russian Foundation for Basic Research (project no. 02-03-32693), by the Council of the President of the Russian Federation for Support of Young Russian Scientists and Leading Scientific Schools (project no. NSh-1763.2003.3), and by the Division of Chemistry and Material Sciences, Russian Academy of Sciences.

## REFERENCES

1. V. I. Nefedov, I. S. Nefedova, *et al.*, Neorg. Mater. **34**, 1295 (1998).
2. V. I. Nefedov, J. Electron Spectrosc. Relat. Phenom. **100**, 1 (1999).
3. V. I. Nefedov and I. S. Fedorova, J. Electron Spectrosc. Relat. Phenom. **85**, 221 (1997).
4. V. I. Nefedov and I. S. Fedorova, J. Electron Spectrosc. Relat. Phenom. **88–91**, 509 (1998).
5. V. I. Nefedov and I. S. Nefedova, J. Electron Spectrosc. Relat. Phenom. **96**, 135 (1998).
6. V. K. Dolmatov and S. T. Manson, Phys. Rev. A **63**, 022704 (2001).
7. A. Derevianko, O. Hemmers, S. Oblad, *et al.*, Phys. Rev. Lett. **84**, 2116 (2000).
8. W. R. Johnson and K. T. Cheng, Phys. Rev. A **63**, 022504 (2001).
9. M. B. Trzhaskovskaya, V. I. Nefedov, and V. G. Yarzhemsky, At. Data Nucl. Data Tables **77**, 97 (2001).
10. M. B. Trzhaskovskaya, V. I. Nefedov, and V. G. Yarzhemsky, At. Data Nucl. Data Tables **82**, 257 (2002).
11. V. I. Nefedov, V. G. Yarzhemsky, I. S. Nefedova, *et al.*, J. Electron Spectrosc. Relat. Phenom. **107**, 123 (2000).
12. V. I. Nefedov, V. G. Yarzhemsky, R. Hesse, *et al.*, J. Electron Spectrosc. Relat. Phenom. **125**, 153 (2002).
13. M. B. Trzhaskovskaya, V. I. Nefedov, V. G. Yarzhemsky, and R. Szargan, Dokl. Akad. Nauk **390**, 615 (2003) [Dokl. Phys. **48**, 274 (2003)].
14. M. B. Trzhaskovskaya, V. I. Nefedov, V. G. Yarzhemsky, and R. Szargan, Poverkhnost, No. 8, 23 (2003).
15. V. I. Nefedov, I. S. Nefedova, V. G. Yarzhemsky, *et al.*, J. Electron Spectrosc. Relat. Phenom. **131–132**, 61 (2003).

*Translated by R. Tyapaev*

*Doklady Physics, Vol. 49, No. 5, 2004, pp. 279–281. Translated from Doklady Akademii Nauk, Vol. 396, No. 1, 2004, pp. 41–43.*

# On a Structural Parameter Determining the Tendency to a Martensitic Transformation in Polycrystals

**A. M. Glezer and E. N. Blinova**

Presented by Academician Yu.A. Osip’yan December 24, 2003

Received December 29, 2003

At present, no physically substantiated theory describes the effect of the submicrocrystalline structure of materials on phase transformations occurring under thermal and deformation actions. This is primarily the case for martensitic transformations, which are rather sensitive to the structural characteristics of the initial phase [1, 2]. In this study, we consider the features of a martensitic transformation in Fe–Ni(29–30%)–C(0.02%) microcrystalline alloys, where the grain sizes of the initial $\gamma$ phase are varied by using intense plastic deformation followed by recrystallization annealing.

The concentration interval of compositions was chosen so that the start temperature $M_s$ of the martensitic transformation was below room temperature [3]. This made it possible to produce and study various structural states of the initial $\gamma$ phase and further to investigate the features of the martensitic transformation upon cooling to low temperatures. Intense shear plastic deformation was performed in a Bridgman chamber at a pressure of 2 GPa. Then, the deformed samples were subjected to isothermal vacuum annealing in the temperature range 600–1000°C for 0.25–6 h. To realize the $\gamma$–$\alpha$ martensitic transformation, the annealed samples were sharply cooled to 77 K. The structure of the samples was investigated by scanning and transmission electron microscopy, as well as by the method of quantitative x-ray diffraction analysis. Alloy samples were obtained with the average grain size $d_{av}$ between 0.3 and 8 μm.

After the samples were cooled to 77 K, the volume fraction of martensite was evaluated on both sample surfaces. Its value was proved to be the same within the experimental error. It was noted that a decrease in $d_{av}$ always reduced the volume fraction of martensite. For example, in the Fe–Ni(32%) alloy, a decrease in the grain size to 2.2 μm resulted in the complete suppression of the martensitic transformation upon cooling to 77 K. In other words, we observed the overcoming of a critical parameter of the crystalline structure, which is responsible for the realization of the martensitic transformation in an alloy of a certain chemical composition upon cooling at a given temperature regime.

Either the maximum or the average grain size in the polycrystalline ensemble can probably be proposed as such a structural parameter. In the former case, the transformation starts in the largest grains and expands throughout the environment polycrystalline matrix. In the latter case, the martensitic transformation in the polycrystal is developed in the statistical regime.

Figure 1 shows the histograms of the size distribution of $\gamma$-phase grains in the Fe–Ni(32%) alloy (a) before and (b) after the martensitic transformation upon cooling to 77 K. The fraction of the transformed volume was 22%. It is seen that the histogram describing the distribution of grains that have undergone the transformation is similar to that describing grains of the initial phase. Moreover, the average size of grains that have undergone the transformation ($D_{av}$ = 6.1 μm) virtually coincides with that of $\gamma$-phase grains ($d_{av}$ = 5.8 μm). If the transformation started in the largest grains, the histogram shown in Fig. 1b would be sharply asymmetric and the maximum of the transformed grains would lie in the region of the largest grains of the $\gamma$ phase. The similarity of the histograms shown in Fig. 1 clearly indicates that it is the average grain size of the polycrystalline ensemble that is responsible for the tendency of the material to the martensitic transformation.

Electron microscopic analysis of the structure of the samples after the martensitic transformation confirmed this conclusion. The martensitic transformation was frequently observed in smaller grains, whereas larger austenite grains remained unchanged. Figure 2 shows the transformed-volume fraction $M$ as a function of $d_{av}$ in the initial $\gamma$ phase for the alloys under investigation. It is clearly seen that a certain average grain size $d^*$ corresponding to “blocking” the martensitic transformation exists for each alloy. In the framework of the so-called “go-ahead” mechanism of the martensitic transformation [4, 5], $V_m$ as a function of $d_{av}$ and the expres-

---

*Kurdyumov Institute of Metal Physics and Functional Materials, Bardin Central Research Institute of Ferrous Metallurgy, Vtoraya Baumanskaya ul. 9/23,*
*Moscow, 107005 Russia*
*e-mail: glezer@imph.msk.ru*

1028-3358/04/4905-0279$26.00

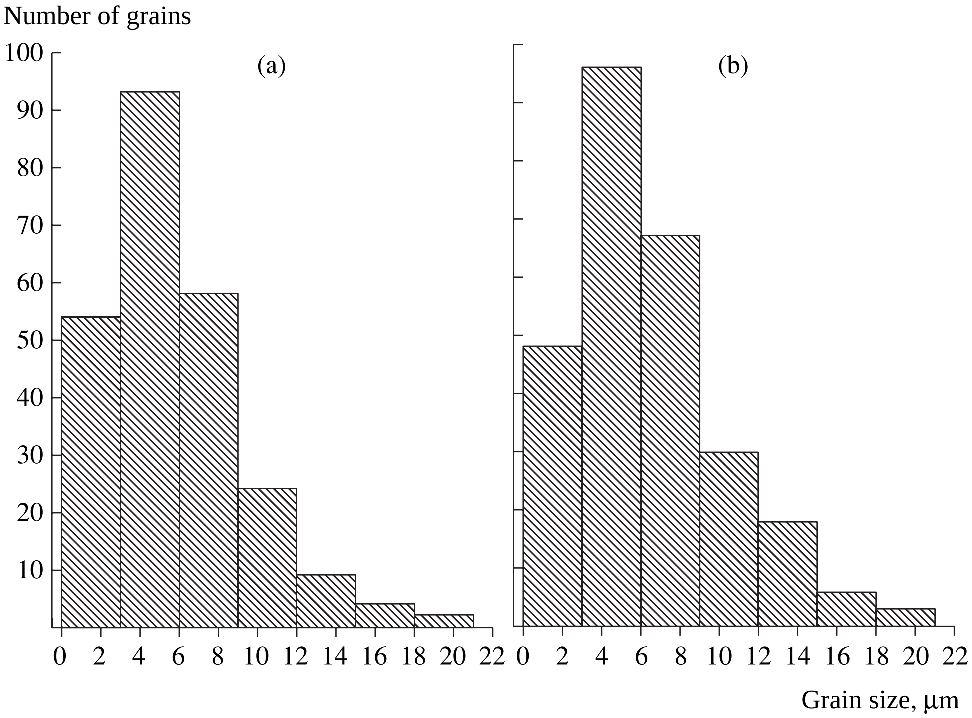

**Fig. 1.** Histograms of the size distribution of γ-phase grains in the Fe–Ni(32%) alloy (a) before and (b) after the martensitic transformation upon cooling to 77 K.

sion for $d^*$ can be analytically described by the relationships [6]

$$M = M_0 - K_m d_{av}^{-1/2}, \quad (1)$$

$$d^* = \left[\frac{K}{T^* - T_f}\right]^2. \quad (1a)$$

Here, $M_0 = K_1(T^* - T_f)$, where $T^*$ is the temperature of the thermodynamic equilibrium of the γ and α phases (up to a factor), $T_f$ is the final cooling temperature, and $K_1$ and $K_m$ are constants.

Relations (1) and (1a) adequately reproduce our experimental results presented in Fig. 2.[1] The physical meaning of the average critical grain size $d^*$ corresponding to the blocking of the transformation can be explained as follows. Only crystals that cannot initiate accommodate stresses high enough to form a martensite crystal in a neighboring grain can be formed in initial-phase grains, whose sizes are less than the critical size. In other words, the go-ahead process stops. The size distribution of grains in the polycrystalline ensemble and, accordingly, the probability of finding a grain of a rather large size in the go-ahead process are statistical. Therefore, it is the average grain size in the initial γ phase that serves as the critical parameter.

Thus, our investigations indicate that the main (but not the only) structural parameter responsible for the tendency to the nonthermoelastic martensitic transfor-

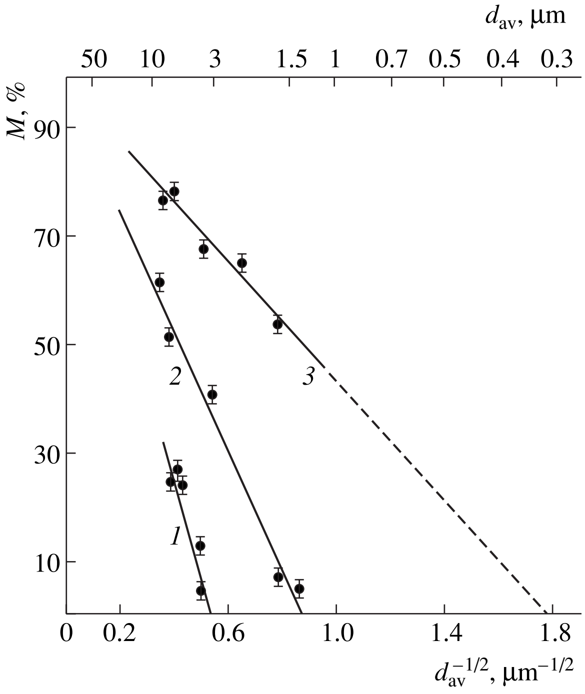

**Fig. 2.** Transformed-volume fraction $M$ vs. the average grain size $d_{av}$ of the initial phase in the alloys containing (*1*) 32, (*2*) 30, and (*3*) 29% Ni.

---

[1] Strictly speaking, the most frequent size (mode) rather than the average grain size must be considered in the framework of the go-ahead mechanism.

mation upon cooling Fe–Ni alloys is the average grain size in the polycrystalline ensemble of the initial (high-temperature) phase.

## ACKNOWLEDGMENTS

This work was supported by the Russian Foundation for Basic Research (project no. 03-02-17296).

## REFERENCES

1. G. V. Kurdyumov, R. I. Entin, and L. M. Utevskiĭ, *Transformations in Iron and Steel* (Metallurgiya, Moscow, 1977).
2. M. A. Shtremel’, Izv. Akad. Nauk, Ser. Fiz. **66**, 1280 (2002).
3. O. P. Maksimova and V. N. Zambrzhitskiĭ, Fiz. Met. Metalloved. **62**, 974 (1986).
4. É. P. Pechkovskiĭ and V. I. Trefilov, Preprint No. 71.4, IMF (Institute of Metal Physics, Kiev, 1971).
5. M. N. Pankova, V. A. Solov’ev, and S. G. Zaĭchenko, Fiz. Met. Metalloved. **55**, 576 (1983).
6. E. N. Blinova, A. M. Glezer, and V. A. Pozdnyakov, Izv. Akad. Nauk, Ser. Fiz. **66**, 1263 (2002).

*Translated by Yu. Vishnyakov*

*Doklady Physics, Vol. 49, No. 5, 2004, pp. 282–284. Translated from Doklady Akademii Nauk, Vol. 396, No. 1, 2004, pp. 44–46.*
*Original Russian Text Copyright © 2004 by Neganov, Kornev.*

## TECHNICAL PHYSICS

# Singular Integral Equations in the Problem of Diffraction of an Electromagnetic Plane Wave by a Perfectly Conducting Finite Hollow Cylinder

**V. A. Neganov and M. G. Kornev**

Presented by Academician Yu.V. Gulyaev October 22, 2003

Received November 17, 2003

### THE ESSENCE OF THE PROBLEM

The problem of diffraction of a plane electromagnetic wave by a finite metallic cylinder (linear electric vibrator) is one of the key problems in the theory of receiving antennas, and it is most difficult to determine the electric-current distribution over the cylinder. The method of calculating the electric-current distribution in a system of thin linear vibrators excited by a plane wave was developed in [1]. In that paper, the diffraction problem (in the thin-vibrator approximation) was reduced to an ill-posed problem [2] that was represented by a set of Fredholm integral equations of the first kind with logarithmic singularities in their kernels and was solved by the self-regularization method [3]. Symmetric vibrations (independent of the azimuth coordinate) of a perfectly conducting finite hollow cylinder were considered in [4]. However, Tikhonov and Dmitriev [3] stated that the solution obtained in [4] is incorrect. On the other hand, the two-dimensional problem of diffraction of a plane electromagnetic wave by an infinite perfectly conducting circular cylinder was solved long ago in [5] under the assumption of the absence of field variations along the axial cylindrical coordinate. In [6–8], the theory of singular equations was applied to develop the theory of a thin electric vibrator in the approximation of a perfectly conducting finite hollow circular cylinder by ignoring the azimuthal electric-current component. In the present study, the problem of the diffraction of a plane electromagnetic wave by a perfectly conducting finite hollow circular cylinder is analyzed with allowance for the azimuthal component of the electric current arising on the cylinder surface.

### STATEMENT OF THE PROBLEM. SINGULAR INTEGRAL EQUATIONS OF THE FIRST KIND

The statement of the problem is illustrated in Fig. 1. A perfectly conducting hollow circular cylinder of radius $a$ and length $2l$ is placed in a homogeneous medium with the parameters $\varepsilon$ and $\mu$. The cylinder axis is taken as the $z$ axis. An arbitrarily polarized plane wave with the electric field $\mathbf{E}^{\text{ext}}$ impinges on the cylinder and induces the surface electric current $\boldsymbol{\eta}(\varphi, z) = \{\eta_\varphi, \eta_z\}$ with the longitudinal $\eta_z$ and azimuthal $\eta_\varphi$ components on the conductor surface. To solve the diffraction problem, the distribution of the electric current $\boldsymbol{\eta}(\varphi, z)$ over the conductor surface must first be determined. In terms of antenna theory, this is the internal problem of the analysis. For the known current distribution over the cylinder surface, it is easy to determine the electromagnetic field (diffraction field) scattered by the cylinder, the directivity pattern for the scattering field of the conducting cylinder, etc.

In order to find the electric-current density $\boldsymbol{\eta}(\varphi, z)$ on the conducting-cylinder surface, we easily write the two-dimensional vector integral equation:

$$-i\omega\varepsilon_0\varepsilon\mathbf{E}_\tau^{\text{ext}}(\varphi, z) = \int_0^{2\pi}\int_{-l}^{l}\eta(\varphi', z')\mathbf{K}(\varphi, z; \varphi', z')d\varphi' dz', \quad (1)$$

where $\mathbf{K}(\varphi, z; \varphi', z')$ is the known tensor kernel.

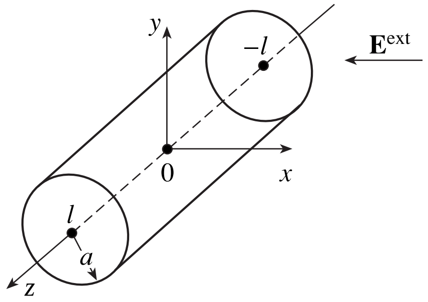

**Fig. 1.** Geometry of the problem for a perfectly conducting hollow circular cylinder.

---

*Volga State Academy of Telecommunication and Informatics, ul. L’va Tolstogo 23, Samara, 443010 Russia*
*e-mail: neganov-samara@mail333.com*

1028-3358/04/4905-0282$26.00 © 2004 MAIK “Nauka/Interperiodica”

Representing the vector $\boldsymbol{\eta}$ in the form of the Fourier series in terms of azimuthal harmonics

$$\boldsymbol{\eta}(\varphi, z) = \sum_{m=-\infty}^{\infty} \boldsymbol{\eta}_m(z)e^{-im\varphi}, \qquad (2)$$

we can write the infinite set of one-dimensional singular equations of the first kind ($m = 0, \pm 1, \pm 2, \ldots$)

$$\frac{1}{\pi}\int_{-1}^{1}\frac{\mathbf{f}_m(t')dt'}{t'-t} = -\sigma\mathbf{E}_m(t) + \int_{-1}^{1}\mathbf{f}_m\mathbf{P}_m(t, t')dt', \qquad (3)$$

$$t \in [-1, 1].$$

Here, $t = \frac{z}{l}$ and $t' = \frac{z'}{l}$ are dimensionless variables and $\mathbf{P}_m(t, t')$ are rather cumbersome known tensor functions for unknown vector functions $\mathbf{f}_m(t) = \{f_1^m(t),\ f_2^m(t)\}$ with the components

$$f_1^m(t) = \frac{l}{a}[m^2 - (ka)^2]\int_{-1}^{t} I_\varphi^m(t')dt' + imI_z^m,$$

$$f_2^m(t) = imI_\varphi^m(t) - \frac{a}{l}\frac{dI_z^m(t)}{dt}, \qquad (4)$$

where

$$I_\varphi^m = a\int_0^{2\pi}\eta_\varphi(\varphi', t)e^{im\varphi'}d\varphi',$$

$$I_z^m = a\int_0^{2\pi}\eta_z(\varphi', t)e^{im\varphi'}d\varphi',$$

$$\mathbf{E}_m(t) = \frac{1}{2\pi}\int_0^{2\pi}\mathbf{E}_\tau^{\mathrm{ext}}(\varphi', t)e^{im\varphi'}d\varphi'.$$

Vector singular equations (3) can be used to determine the $m$-azimuthal harmonics $\eta_m(z)$ of the current $\eta(\varphi, z)$ on the conducting-cylinder surface, which are excited by the $m$-azimuthal harmonics $\mathbf{E}_m(t)$ of the external electric field $\mathbf{E}^{\mathrm{ext}}(\varphi, z)$. The intrinsic feature of the new unknown vector functions $\mathbf{f}_m(t)$ in Eqs. (3) is that their components $f_1^m(t)$ and $f_2^m(t)$ vanish and have integrable singularities, respectively, at the ends of the interval [–1, 1]. This behavior of the functions $\mathbf{f}_m(t)$ is associated with the properties of the electromagnetic field near the edges of the perfectly conducting hollow cylinder [9]. For a thin electrical vibrator ($\eta_\varphi \equiv 0$), when the external electric field is independent of the azimuth coordinate $\varphi$ and $\mathbf{E}^{\mathrm{ext}}(z) = \mathbf{z}_0E^{\mathrm{ext}}(z)$, we arrive at one scalar singular equation for the zeroth azimuthal harmonic rather than at Eqs. (3). This equation describes symmetric oscillations of a perfectly conducting finite hollow cylinder [8].

## SOLVING THE SET OF SINGULAR EQUATIONS: NUMERICAL RESULTS

Vector singular equations (3) for the azimuthal harmonics of the electric current were solved by the method of partial inversion of the integral operator that was developed in [10, 11] for strip–gap waveguides. As a result, the determination of each $m$-azimuthal harmonic $\boldsymbol{\eta}_m$ of the electric current was reduced to solving the one-dimensional Fredholm integral equation of the second kind. The surface electric-current density $\boldsymbol{\eta}$ was calculated by formula (2).

Taking into account the physical features of the behavior of the surface current components at the ends of the conducting hollow cylinder, we find the unknown functions $f_1^m(t)$ and $f_2^m(t)$ in the form of the expansions

$$f_1^m(t) = \sqrt{1-t^2}\sum_{n=0}^{N}\frac{C_n^m}{n+1}U_n(t),$$

$$f_2^m(t) = -\frac{1}{\sqrt{1-t^2}}\sum_{n=0}^{N}C_n^mU_{n+1}(t). \qquad (5)$$

Here, $U_n(t)$ are the Chebyshev polynomials of the first kind and $C_n^m$ and $D_n^m$ are unknown constants to be determined.

As an example, the method was used to calculate the distributions of the current density components $j_z = 2\pi a\eta_z$ and $j_\varphi = 2\pi a\eta_\varphi$ over the conducting hollow cylinder. This current is induced by a plane wave propagating normally to the cylinder axis (along the $x$ direction, see Fig. 1). The calculations were performed for the parallel polarization of the incident wave (i.e., its electric field is parallel to the cylinder axis):

$$\mathbf{E}^{\mathrm{ext}}(\varphi, t) = \mathbf{z}_0E_0e^{-ika\cos\varphi}. \qquad (6)$$

Figure 2 shows the distributions of the current components $j_z$ and $j_\varphi$ for $\varphi = 0$ over the cylinder with the geometric parameters $\frac{l}{\lambda} = \frac{a}{\lambda} = \frac{1}{4}$ and $E_0 = 1$ V/m. The distributions Re$j_z$ and Im$j_z$ in the absence of the azimuthal component ($j_\varphi \equiv 0$) are shown by the dashed lines in Fig. 2a. Solid and dashed curves in Fig. 3 show the dependence of Re$j_z$ and Im$j_z$, respectively, on the azimuth angle $\varphi$ in the polar coordinate system for $t = 0$; the scale of 1 cm along the $\rho$ coordinate corresponds to $10^{-3}$ A. It is obvious that the azimuthal component of the electric current on the cylinder surface must be taken into account.

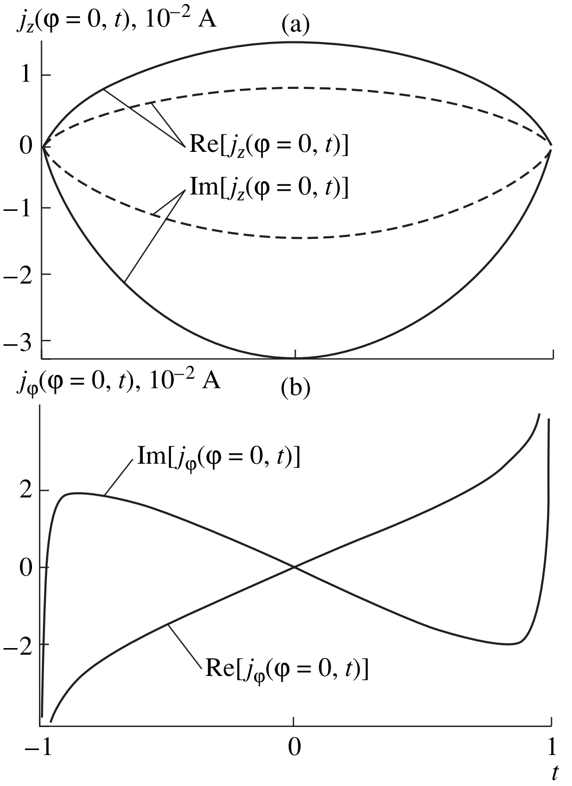

**Fig. 2.** Distributions of the electric-current components (a) $j_z$ and (b) $j_\varphi$ over the cylinder for $\frac{l}{\lambda} = \frac{a}{\lambda} = \frac{1}{4}$ and $E_0 =$ 1 V/m. The dashed lines show the distributions of Re$j_z$ and Im$j_z$ in the absence of the azimuthal component ($j_\varphi = 0$).

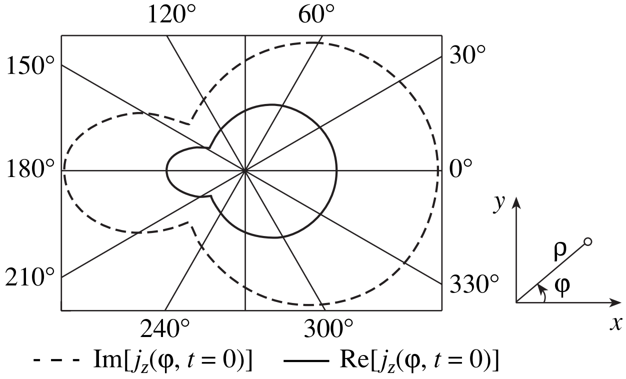

**Fig. 3.** (Solid curve) Re$j_z$ and (dashed curve) Im$j_z$ vs. the azimuth angle φ in the polar coordinate system for $t = 0$.

The method of calculating the diffraction of a plane electromagnetic wave by a cylinder has good internal convergence. In particular, the current magnitudes at a fixed point vary by no more than 0.1% when $M$ [the number limiting the summation in Eq. (2)] increases from 10 to 15. In this case, it is sufficient to take $N = 15$ terms in expansions (5).

## CONCLUSIONS

Thus, we have found the vector singular equations for the azimuthal harmonics of electric-current components on the surface of a finite cylinder. These equations are the generalization of the scalar singular equation that describes symmetric oscillations of a perfectly conducting thin cylindrical electric vibrator [8] to the case of a perfectly conducting thick hollow cylinder, where the azimuthal component of the surface electric current must be taken into account. The method can be easily generalized for a system of perfectly conducting finite cylinders.

## REFERENCES

1. A. S. Il’inskiĭ and I. V. Berezhnaya, Vychisl. Metody i Programmir., No. 20, 142 (1973).
2. A. N. Tikhonov and V. Ya. Arsenin, *Solution of Ill-Posed Problems* (Nauka, Moscow, 1986).
3. A. N. Tikhonov and V. I. Dmitriev, Vychisl. Metody i Programmir., No. 10, 3 (1968).
4. P. L. Kapitsa, V. K. Fock, and L. A. Vaĭnshteĭn, Zh. Tekh. Fiz. **29**, 1189 (1959) [Sov. Phys. Tech. Phys. **4**, 1088 (1959)].
5. V. V. Nikol’skiĭ and T. I. Nikol’skaya, *Electrodynamics and Propagation of Radio Waves* (Nauka, Moscow, 1989).
6. V. A. Neganov and I. V. Matveev, Fiz. Voln. Protsessov i Radiotekhn. Sistemy **2** (2), 27 (1999).
7. V. A. Neganov and I. V. Matveev, Dokl. Akad. Nauk **371**, 36 (2000) [Dokl. Phys. **45**, 317 (2000)].
8. V. A. Neganov, E. I. Nefedov, and G. P. Yarovoĭ, *Electrodynamic Methods in Designing Microwave Devices and Antennas* (Radio i Svyaz’, Moscow, 2002).
9. R. Mittra and S. W. Lee, *Analytical Techniques in Theory of Waveguides* (Macmillan, New York, 1971; Mir, Moscow, 1974).
10. V. A. Neganov, E. I. Nefedov, and G. P. Yarovoĭ, *Strip–Gap Lines for Microwave and Extremely High Frequencies* (Nauka, Moscow, 1996).
11. A. S. Aref’ev and V. A. Neganov, *Method of Partial Inversion of Operators in Problems of Natural Waves in Strip and Gap Transmission Lines* (Radio i Svyaz’, Moscow, 2002).

*Translated by G. Merzon*

*Doklady Physics, Vol. 49, No. 5, 2004, pp. 285–288. Translated from Doklady Akademii Nauk, Vol. 396, No. 2, 2004, pp. 183–186.*
*Original Russian Text Copyright © 2004 by Goman'kov, Kovalev, Vaĭnshteĭn, Zhigalina, Tret'yakova, Fykin.*

## TECHNICAL PHYSICS

# Fine Crystalline Structure of Microcrystalline Alloys

**V. I. Goman'kov*, A. I. Kovalev*, D. L. Vaĭnshteĭn*, O. M. Zhigalina,**
**S. M. Tret'yakova, and L. E. Fykin**

Presented by Academician Yu.A. Osip'yan December 24, 2003

Received December 29, 2003

The formation of microcrystalline alloys in the hardening process from a melt is accompanied by the formation of stable and metastable phases, whose atomic ordering is insufficiently studied. For certain systems, the phase diagrams including an intermetallic compound with transformation temperature $T_{cr}$ close to the melting point $T_m$ are of determining importance for explaining the long-range atomic order. To study the causes of the formation of an ordered state in microcrystalline alloys, we suggest analyzing the $Ni_3Mn$–$Ni_3Al$ quasi-binary system, where the isomorphic concentration transition $L1_2 \to L1_2$ from the $Ni_3Mn$ ordinary superstructure to the $Ni_3Al$ intermetallic compound is observed below 750 K. The states of massive annealed alloys of this system are present on the ordered phase diagram including the $\gamma + \gamma'$ two-phase region [1].

Strip samples 2–10 mm in width and 40–80 μm in thickness are obtained by hardening from a melt in an argon atmosphere. The table presents the compositions of the original massive samples. The size of crystallites in a microcrystalline strip lies in the range 8–10 μm. Samples for neutron diffraction analysis and electron microscopy are prepared from the strips.

Neutron-diffraction and small-angle neutron-scattering (SANS) analyses were carried out on neutron diffractometers with neutron wavelength $\lambda = 0.128$ and 0.236 nm, respectively [2]. Certain samples were analyzed with a TEMSCAN GEM 200 CP electron microscope with accelerating voltages 160 and 200 kV. The features of electronic and atomic structure of alloys 2, 4, and 9 were studied by x-ray photoelectron spectroscopy (XPS) and electron energy-loss spectroscopy (EELS) on an ESCALAB MK2 electron spectrometer produced by the VG firm (United Kingdom). The photoelectron spectra were excited by means of a monochromatized $AlK_\alpha$ source ($h\nu$ = 1486.6 eV for an instrumental resolution of 0.6 eV). The electron energy-loss spectra are analyzed near the 980-eV line of elastically scattered electrons in a 250-eV-wide energy range. The physical foundations of the method and its experimental features were reported in [3]. The electron spectra were detected under the physical and engineering conditions ensuring both the best energy resolution and best signal-to-noise ratio.

The chemical compositions of alloys 4 and 9 were determined also by Auger-electron spectroscopy and the results were compared with the chemical-analysis data. In these alloys, the heterogeneous distribution of Al and Mn over the surface of samples was detected with the Al-content variation ranges 7.0–22.0 and 9.0–23.5 at. %, respectively. It was found that heterogeneity was inherent in the surfaces of samples rather than in their volumes. These data testify to both the separation of the solid solution of microcrystals and formation of domains with different Al and Mn contents.

Figure 1 shows the parts of the neutron diffraction patterns of microcrystalline alloys that testify to the atomic ordering in samples despite the hardening of alloys from melts. The neutron diffraction patterns contain only one system of superstructure ($I_{100}$ and $I_{110}$) and main ($I_{111}$ and $I_{200}$) reflections that corresponds to the fcc crystal lattice ordered in the $L1_2$ type. The spread peaks $I_{100}$ and $I_{110}$ from samples 2 and 3 testify to the short-range atomic order, which coexists with the long-range order in alloy 3.

Narrowing of the $I_{100}$ and $I_{110}$ reflections from alloys 4–9 shows that the structure of antiphase domains of the long-range order is formed. The average sizes $\varepsilon$ of domains are determined from the widths of the $I_{100}$ reflections and are given in the table. The concentration dependence of $\varepsilon$ (table) may indicate that both the long-range order and volume fraction $V_{\gamma'}$ of the ordered $\gamma'$ phase increase with an increase in the Al concentration $c_{Al}$.

The fine crystalline structure of microcrystals is corroborated by the electron-microscopy results. The electron diffraction patterns of samples 5 and 7 exhibit the system of superstructure and main reflections that is evidence of the $L1_2$-type long-range order. Figure 2 shows the dark-field image of alloy 5 as obtained under

---

*Bardin Central Research Institute of Ferrous Metallurgy, Vtoraya Baumanskaya ul. 9/23, Moscow, 107005 Russia*
** e-mail: sprg@mail.sitek.ru*

1028-3358/04/4905-0285$26.00 © 2004 MAIK "Nauka/Interperiodica"

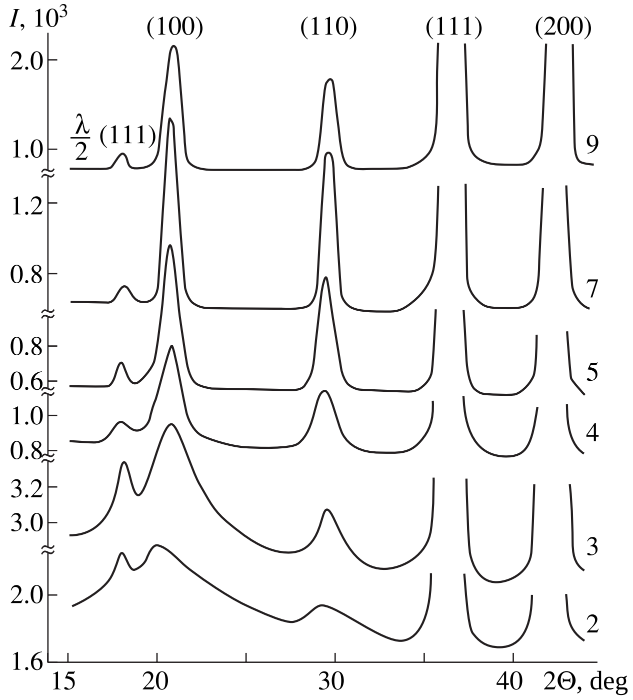

**Fig. 1.** Neutron diffraction patterns of microcrystalline alloys 2 (5.0% Al), 3 (7.5% Al), 4 (10.0% Al), 5 (12.5% Al), 7 (17.5% Al), and 9 (22.5% Al).

the action of superstructure reflections. The observed 5–10 nm spherical domains agree with the estimates of ε values in the table. The sizes and shape of domains enable one to assume that the ordered state in microcrystals is realized in the $\gamma + \gamma'$ two-phase region [1], which is structurally inhomogeneous. The dark-field image of sample 7 demonstrates the developed domain structure over almost the entire sample.

Small-angle neutron scattering measured on samples 4 and 5 indicates that the alloys are structurally inhomogeneous. The table presents the diameters of inhomogeneities that are calculated from the SANS intensities in the Guinier spherical approximation. These diameters are close to domain sizes ε and, therefore, inhomogeneities are formed by the $\gamma'$ phase in the disordered $\gamma$ matrix.

Thus, the structural states of microcrystalline alloys correspond to the structural states of alloys in the $\gamma + \gamma'$ two-phase region and are characterized by the coexistence of the disordered and ordered phases.

To determine the $V_{\gamma'}$ value of the $\gamma'$ phase and calculate the long-range order parameters $S$, the phase diagram is taken from [1], where the temperature $T_{cr}$ of the upper boundary of the $\gamma + \gamma'$ two-phase region are given (table). According to the phase diagram, the short-range order in sample 2 (Fig. 1) is formed above $T_{cr}$ in the $\gamma'$ phase. The short-range order parameters $\alpha_1 = -0.105$ and $\alpha_2 = 0.315$ of the first and second coordination spheres, respectively, are estimated as the maximum possible from the $I_{100}$ diffuse intensity (Fig. 1) [4]. The $\alpha_1$ value is close to the equilibrium value calculated for $T = 1425$ K in linear theory [5]. Therefore, the short-range order in the $\gamma$ phase is assumed to be formed at either the melting point or crystallization temperature.

The coexistence of the short- and long-range orders in alloy 3 (Fig. 1) indicates that the latter is realized in the $\gamma'$ phase of the two-phase region slightly below $T_{cr}$ (table). For this reason, the $V_{\gamma'}$ values and parameter $S$ are calculated on the phase diagram [1] by using the temperature section that corresponds to $T_{cr} = 915$ K of alloy 2 and for which the states of remaining samples are considered below their $T_{cr}$ values. In this case, the $\gamma$ and $\gamma'$ phases have the compositions 75.0% Ni–20.0% Mn–5.0% Al and 75% Ni–6.0% Mn–19.0% Al, respectively. The $\gamma'$ phase of this composition has values $T_{cr} = 1380$ K and $T_m = 1600$ K [1], and the $V_{\gamma'}$ values obtained by the section rule in the two-phase region are given in the table. According to the table, an increase in $V_{\gamma'}$ is accompanied by an increase in the domain size ε

**Table**

| Sample no. | Ni | Mn | Al | ε | $D$ | $T_{cr}$, K | $V_{\gamma'}$ | $S$ | $\Delta E_b$ | |
|---|---|---|---|---|---|---|---|---|---|---|
| | at. % | | | nm | | | | | Ni $2p_{3/2}$ | Mn $2p$ |
| 2 | 75.0 | 20.0 | 5.0 | – | – | 915 | 0 | 0 | 0.8 | –0.6 |
| 3 | 75.0 | 17.5 | 7.5 | 5.3 | – | 953 | 0.179 | 0.96 ± 0.1 | – | – |
| 4 | 75.0 | 15.0 | 10.0 | 6.8 | 8.0 | 1043 | 0.357 | 1.02 ± 0.1 | 0.9 | –0.4 |
| 5 | 75.0 | 12.5 | 12.5 | 9.7 | 13.2 | 1113 | 0.536 | 1.11 ± 0.1 | – | – |
| 7 | 75.0 | 7.5 | 17.5 | 19.2 | – | 1320 | 0.893 | 1.02 ± 0.1 | – | – |
| 9 | 75.0 | 2.5 | 22.5 | – | – | 1525 | 1.000 | 0.92 ± 0.1 | 1.3 | 0 |

and $D$ values. Alloy 9 on the phase diagram [1] belongs to the $\gamma'$ single-phase region.

The energy-loss spectra of electrons scattered on the microdomains of the $\gamma'$ phase are measured for alloy 4. The disordered $\gamma$ phase does not considerably contribute to the fine structure of the energy-loss spectra. Therefore, the gained information characterizes the distances of the first, second, and third coordination spheres in the $\gamma'$ phase. Figure 3 shows a Fourier transform of the spectrum that is similar to the radial distribution function and describes the distribution of atoms of all types in these spheres. From the positions of the peaks in Fig. 3, the Ni–(Mn, Al) interatomic distances are determined as 0.254, 0.354, and 0.431 nm, respectively, which are less than the corresponding values for the single-phase ordered sample of the original composition by 0.7% on average (table). A decrease in the interatomic distances is naturally attributed to the partial substitution of Mn atoms by Al atoms upon precipitation of nanocrystals of the $\gamma'$ phase. A similar effect was observed in [6] for massive alloys of the $Ni_3Fe$–$Ni_3Al$ system and was treated as the structural explanation of large lattice stresses.

The long-range order parameters $S$ are calculated by the following standard formula containing the $V_{\gamma'}$ values and compositions of the $\gamma$ and $\gamma'$ phases:

$$S^2 = k\frac{V_{\gamma'}\left|F^{\gamma'}_{200}\right|^2 + (1 - V_{\gamma'})\left|F^{\gamma}_{200}\right|^2}{V_{\gamma'}\left|F^{\gamma'}_{100}\right|^2}\frac{I_{100}}{I_{200}}.$$

Here, $k$ is the constant including Debye–Waller coefficients, absorption factor, and Lorentz factor, and $F^{\gamma'}_{100}$, $F^{\gamma'}_{200}$, and $F^{\gamma}_{200}$ are structure factors of the $\gamma$ and $\gamma'$ phases that describe the $I_{100}$ and $I_{200}$ reflections. The formula for the ratio $\frac{I_{110}}{I_{220}}$ with another $k$ value is similar.

The average $S$ values obtained from two ratios of the intensities are given in the table. It is seen that the $\gamma'$ phase is formed with maximum $S$ values. For these $S$ values, the average number of the Al–Ni and Mn–Ni bonds in the first coordination sphere around the Al and Mn atoms is equal to 12, and the number of the Al–Al, Al–Mn, and Mn–Mn bonds in the second coordination sphere is equal to 6 [4], which is shown in Fig. 3. In turn, the increase in $\varepsilon$ is likely caused by an increase in the $V_{\gamma'}$ values.

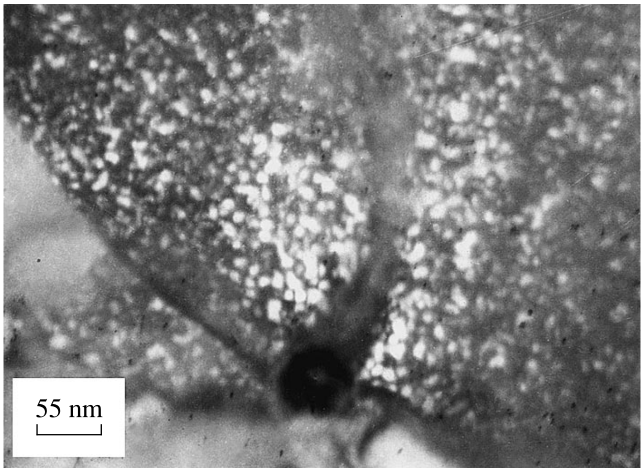

**Fig. 2.** Dark-field image of alloy 5.

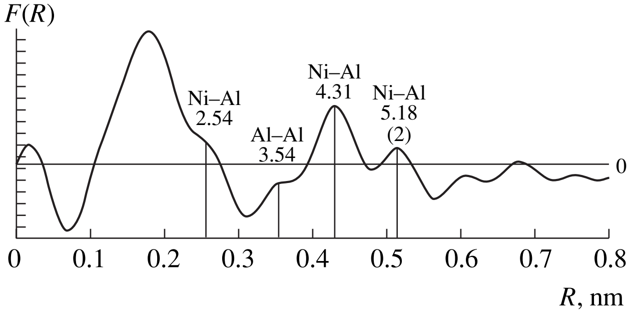

**Fig. 3.** Fourier transform of the energy-loss spectrum of electrons scattered on alloy 4. The Ni–Al, Al–Al, and Al–Mn bonds in the coordination spheres around Al atoms are indicated.

Analysis of the position of the Ni $2p_{3/2}$ and Mn $2p$ lines in the electron spectra of samples 2, 4, and 9 reveals the chemical shift $\Delta E_b$ with respect to the binding energies of the corresponding levels in the pure components. The $\Delta E_b$ values for the inner levels of Ni and Mn atoms are presented in the table. As is seen, with an increase in $c_{Al}$, the $\Delta E_b$ values for the Ni $2p_{3/2}$ line increase up to +1.3 eV, and the $\Delta E_b$ values for the Mn $2p$ line decrease to zero in absolute value. This effect is attributed to both an increase in the fraction of Ni–Al bonds and their strengthening as compared to Ni–Mn bonds, which corresponds to both an increase in the $V_{\gamma'}$ values (table) and the above compositions of the $\gamma$ and $\gamma'$ phases. For $c_{Al} > 17.5\%$, this effect correlates with the concentration dependence of the lower boundary $T_{cr}$ of the $\gamma' - \gamma$ two-phase region of the phase diagram [1].

Thus, changes in the electronic structures of the atoms of the ordered and disordered phases are accompanied by the formation of the long-range atomic order in microcrystals. The perfect long-range order in microcrystals of the $Ni_3Mn$–$Ni_3Al$ system is formed in the ordered $\gamma'$ phase near the crystallization temperatures, and the quantity $S$ is conserved upon forming the $\gamma + \gamma'$ two-phase region when the volume fraction $V_{\gamma'}$ of the $\gamma'$ phase varies. The revealed structural mechanism of the formation of the long-range order in microcrystals is likely inherent in other systems containing an intermetallic compound.

## ACKNOWLEDGMENTS

This work was supported by the Russian Foundation for Basic Research (project no. 03-02-16896). The neutron-diffraction part of the work was supported by the State Program “Neutron Investigations of Matter.”

## REFERENCES

1. V. I. Goman’kov, S. M. Tret’yakova, E. V. Monastyrskaya, *et al.*, Metally, No. 6, 104 (1998).
2. V. I. Goman’kov, A. D. Gezalyan, B. N. Tret’yakov, *et al.*, Fiz. Met. Metalloved., No. 10, 80 (1990).
3. D. L. Wainstein and A. I. Kovalev, Surf. Interface Anal. **34**, 230 (2002).
4. J. M. Cowley, Phys. Rev. **77**, 669 (1950).
5. P. C. Clapp and S. C. Moss, Phys. Rev. **142**, 418 (1966).
6. S. Pascarelli, F. Boscherini, S. Mobilio, *et al.*, Phys. Rev. B **49**, 14984 (1994).

*Translated by R. Tyapaev*

*Doklady Physics, Vol. 49, No. 5, 2004, pp. 289–291. Translated from Doklady Akademii Nauk, Vol. 396, No. 2, 2004, pp. 187–190.*

## TECHNICAL PHYSICS

# Solid-Phase Synthesis and Martensitic Transformations in Al/Ni Thin Films

**V. G. Myagkov and L. E. Bykova**

Presented by Academician V.V. Osiko February 9, 2004

Received November 6, 2003

The solid-phase synthesis in the AL/Ni system has been widely studied with massive samples. In particular, the synthesis between aluminum and nickel powders was observed in mechanochemical synthesis [1], self-propagating high-temperature synthesis [2], shock wave loading [3], and hot pressing [4] and cold rolling of a layered system containing pure aluminum and nickel foils [5]. Numerous works were devoted to solid-state reactions in Al/Ni thin film systems (see [6–9] and references cited therein). The solid-phase synthesis between nickel and aluminum in thin films begins at low temperatures. Most works show that the initiation temperature $T_0$ of solid-state reactions in Al/Ni bilayer films and multilayers lies in the range 160–275°C. The phase diagram of the Al–Ni system shows five stable intermetallic compounds: $Al_3Ni$, $Al_3Ni_2$, AlNi, $Al_3Ni_5$, and $AlNi_3$. However, it is not definitely clear which phase arises first.

The review of early works [6] implies that the $Al_3Ni$ phase is the first phase formed in the temperature range 250–275°C. Thermodynamic calculations based on the Gibbs free energy admit the formation of only the AlNi phase. The formation of the first B2-AlNi phase was observed upon annealing Al/Ni multilayers [7]. Further investigations [8, 9] implied the formation of amorphous and metastable $Al_9Ni_2$ phases.

In [10–12], the formation of the first phase and phase sequence in bilayer films and multilayers was attributed to the solid-phase transformations occurring in a given binary system. In particular, the solid-phase synthesis in the S/Fe thin-film system was associated with the structural transformations in iron monosulphide FeS that accompanied the metal–insulator phase transition. The order–disorder transition in the AuCu alloy is responsible for solid-state reactions in Cu/Au bilayer films. Solid-state reactions in the Se/Cu film system proceed in the mode of the self-propagating high-temperature synthesis (SHS) at the temperature of the superionic transition in the $Cu_2Se$ phase [10]. It was particularly surprising that diffusionless martensitic transformations could also be responsible for the solid-phase synthesis in thin layers [11]. The first-phase rule proposed in [10] is extended to martensitic transformations [11] and includes the following two statements.

(i) The initiation temperature $T_0$ of the solid-phase synthesis in bilayer thin-film samples and multilayers must coincide with the start temperature $A_S$ of the reverse martensitic transformation for a given binary system if other structural transformations do not precede the martensitic transformation.

(ii) Reaction products contain both austenite and martensite phases.

Indeed, as was shown in [11], the initiation temperature $T_0$ of the solid-phase synthesis in Ni/Ti and Cd/Au bilayer thin-film systems coincides with the martensitic-transformation temperature $A_S$ in the NiTi and AuCd alloys, respectively: $T_0(\mathrm{Ni/Ti}) = A_S(\mathrm{NiTi}) = 400$ K and $T_0(\mathrm{Cd/Au}) = A_S(\mathrm{AuCd}) = 340$ K.

The solid-phase synthesis in Al/Ni bilayer thin films for heating rates above 20°C/s proceeds in the SHS mode and its initiation temperature is $T_0 \sim 180°\mathrm{C}$. This temperature lies in the range 160–275°C of the initiation of the solid-phase synthesis in Al/Ni thin films that was determined in previous works (see [6–9] and references cited therein). Therefore, it is reasonable to assume that the initiation temperature $T_0 \sim 180°\mathrm{C}$ is characteristic of the solid-phase synthesis, independent of the heating rate and film thickness, and constant for a given pair of reagents.

Martensitic transformations in the Ni–Al binary system are associated with the transition of the B2-NiAl austenite phase either to the $L1_0$ martensitic structure with the ABC (3*R*) packing or to the ABCABAC (7*R*) packing. The concentration range for the martensitic transformations $B2 \rightarrow L1_0$ (3*R*) and $B2 \rightarrow 7R$ lies from 63 to 68 at. % Ni and from 60 to 63 at. % Ni, respectively. Certain characteristics of the reversible shape memory effect that is manifested upon bending a massive sample and associated with the martensitic transformation were presented in [12]. The start temperature

---

*Kirenskiĭ Institute of Physics, Siberian Division, Russian Academy of Sciences, Akademgorodok, Krasnoyarsk, 660036 Russia*
*e-mail: miagkov@iph.krasn.ru*

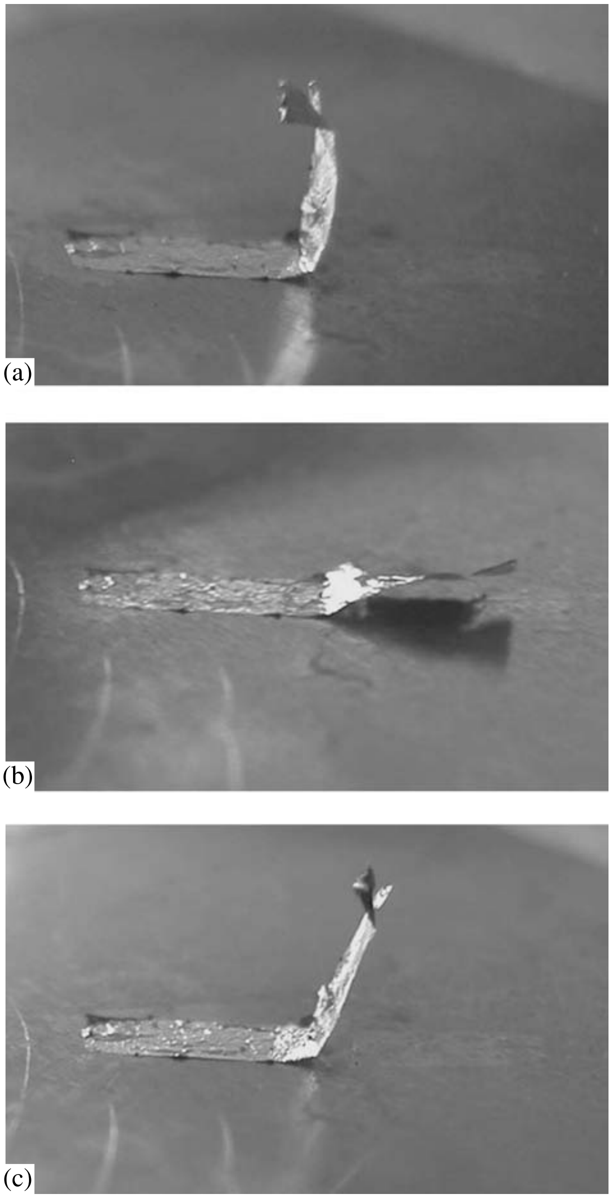

**Fig. 1.** Demonstration of the reversible shape memory effect in Al/Ni thin films: (a) the original Al/Ni film sample after the solid-phase synthesis that is deformed at a temperature of 20°C, (b) the sample after heating up to a temperature of about 250°C, and (c) the sample after further cooling to a temperature of 20°C.

$M_S$ of the martensitic transformation depends strongly on the composition and decreases from 400 to 200°C with a decrease in the Ni content. However, only a small amount of data have been determined for the start $A_S$ and finish $A_f$ temperatures of the reverse martensitic transformation. Determination of the temperatures $A_S$ and $A_f$ from change in the intensity of the (211) peak of the B2 phase in the 63.8 Ni–Al alloy yields $A_S = 130°C$ and $A_f = 190°C$ [12]. In view of the experimental spread in the initiation temperatures $T_0$ of the solid-phase synthesis in Al/Ni multilayers and bilayer thin films and strong dependence of the martensitic temperatures on defects and residual stresses, it is reasonable to assume that the first condition of the first-phase rule is valid for the Ni–Al system. According to the second part of the first-phase rule, the austenite and martensite phases are expected to dominate in the reaction products. As is known, an exclusive feature of alloys capable of martensitic transformations is the shape memory effect. This feature provides a simple method of determining the presence of the austenite and martensite phases in a sample without structural investigations.

This works aims to observe the shape memory effect in Al/Ni thin films after the initiation of the solid-phase synthesis and thereby to experimentally corroborate the dominating formation of the austenite and martensite phases in the reaction products.

A solid-state reaction between aluminum and nickel layers can be initiated by two methods. First, samples were obtained by sequential deposition of nickel and aluminum layers on the (001)NaCl surface at a temperature of 250°C, which exceeds the initiation temperature $T_0$. Second, the Ni film is deposited on the (001)NaCl surface at a temperature of 250°C, and the Al film is deposited at room temperature with the further heating of the bilayer film system up to a temperature exceeding the initiation temperature $T_0$. In this case, the reaction at heating rates above 20°C/s proceeds in the SHS mode. The resulting samples with a width of 2–3 mm and length of 8–12 mm are removed from the NaCl substrate and set down on the preliminarily oxidized surface of a copper foil. After removal of moisture at room temperature, one edge of the film is carefully raised by a razor and deformed up to a direction close to a perpendicular to the foil plane (Fig. 1a). An increase in the temperature of the sample above the initiation temperature, $T = 250°C > T_0$ (Fig. 1b), and further cooling to room temperature (Fig. 1c) reveal the reversible shape memory effect. The shape of the sample is completely recovered upon one-hour aging at room temperature (Fig. 1a). The reversible shape memory effect was observed in samples where the synthesis was initiated upon codeposition, as well as after the SHS in bilayer films, and did not disappear in the aging process at room temperature for one month.

Motion of the film edge is intermittent during both direct and reverse transitions. Such jump motion is likely associated with the avalanche formation or disappearance of martensitic domains. In particular, such a phenomenon accompanies the emission of sound upon martensitic transformations and can be considered in the model of self-organized criticality [13].

The shape memory effect in reacted samples (Fig. 1) convincingly shows that the first phases formed at the aluminum–nickel interface in Al/Ni thin films when temperature increases are the B2-NiAl and martensite phases. In addition to martensitic structures with typical packings 3*R* and 7*R*, packings with ten periodic layers can be observed. The variety of structural modifications of the $LI_0$ and $7R$ martensite phases gives rise to numerous diffraction reflections, which hinders the unambiguous determination of the phase composition of films on the basis of diffraction reflections. Therefore, the ambiguous determination of the first phase in the solid-phase synthesis in Al/Ni thin films in previous works (see [6–9] and references cited therein) may be attributed to the formation of martensite phases in the reaction products.

The shape memory effect is also expected after the solid-phase synthesis in the Ni/Ti and Au/Cd bilayer and multilayer film systems, because the Ni–Ti and Au–Cd binary systems are capable of low-temperature martensitic transformations. These conditions satisfy the above first-phase rule. Indeed, the solid-phase transformation of Ni/Ti multilayers to an intermetallic alloy exhibiting the reversible shape memory effect when the annealing temperature increased was demonstrated in [14]. In this case, it was implied that the synthesis includes the amorphization process at a temperature of 330°C and further crystallization at 420°C. However, as was shown in [11], the solid-state reaction in Ni/Ti bilayer thin films begins at a temperature of about 120°C, which is close to the temperature of the reverse martensitic transformation in titanium nickelide.

The connection of the solid-phase synthesis in thin films with martensitic transformations is allowed by the martensitic mechanism of the atomic transfer through a reaction product. This mechanism is based on the directed motion of reagent atoms over planes and directions coinciding with the planes and directions of the martensitic shift. As a result, reagent atoms are rapidly transferred through a reaction product with the formation of orientational connections between the reaction products and reagents [11]. The martensitic mechanism implies the exceptional role of shear deformations in the initiation of solid-state reactions at the interface between reagents. Therefore, the formation of the austenite and martensite phases in the mechanical synthesis due to the action of shock waves is expected at the initial stage. Indeed, the mechanical alloying of the aluminum–nickel mixture leads to the formation of the B2-NiAl [1, 15] and $L1_0$ phases [15].

Thus, the shape memory effect is convincing evidence that the first phase formed in Al/Ni thin films when temperature increases after the solid-phase synthesis is the B2-NiAl phase, which is transformed to martensite phases when temperature decreases below $M_S$. A consequence of the proposed martensitic mechanism of the atomic transfer through the reaction-product layer is the same phase formation at the initial stage for different methods of initiating the solid-phase synthesis.

## ACKNOWLEDGMENTS

This work was supported by the OAO MMK Foundation, Ausferr Engineering Center, and Intels Foundation for Science and Education (project no. 10-03-02).

## REFERENCES

1. M. Atzmon, Phys. Rev. Lett. **64**, 487 (1990).
2. A. Biswas, S. K. Roy, K. R. Gurumurthy, *et al.*, Acta Mater. **50**, 757 (2002).
3. E. Dunbar, N. N. Thadhani, and R. A. Graham, J. Mater. Sci. **28**, 2903 (1993).
4. K. Morsi, H. McShane, and M. McLean, Scr. Mater. **37**, 1839 (1997).
5. H. Sieber, J. S. Park, J. Weissmuller, and J. H. Perepezko, Acta Mater. **49**, 1139 (2001).
6. M. Nastasi, L. S. Hung, and J. W. Mayer, Appl. Phys. Lett. **43**, 831 (1983).
7. C. Michaelsen, K. Barmak, and G. Lucadamo, J. Appl. Phys. **80**, 6689 (1996).
8. E. Rimini, M. Nastasi, J. Liu, *et al.*, Appl. Phys. Lett. **48**, 303 (1986).
9. K. J. Blobaum, D. Van Heerden, A. J. Gavens, and T. P. Weihs, Acta Mater. **51**, 3871 (2003).
10. V. G. Myagkov, L. E. Bykova, and G. N. Bondarenko, Dokl. Akad. Nauk **390**, 35 (2003) [Dokl. Phys. **48**, 206 (2003)].
11. V. G. Myagkov, L. E. Bykova, and G. N. Bondarenko, Dokl. Akad. Nauk **388**, 46 (2003) [Dokl. Phys. **48**, 30 (2003)].
12. P. L. Potapov, N. A. Poliakova, and V. A. Udovenko, Scr. Mater. **35**, 423 (1996).
13. S. M. Shapiro, B. X. Yang, G. Shirane, *et al.*, Phys. Rev. Lett. **62**, 1298 (1989).
14. V. K. Portnoĭ, A. M. Blinov, I. A. Tomilin, *et al.*, Fiz. Met. Metalloved. **93** (4), 42 (2002).
15. T. Lehnert, H. Grimmer, P. Boni, *et al.*, Acta Mater. **48**, 4065 (2000).

*Translated by R. Tyapaev*

*Doklady Physics, Vol. 49, No. 5, 2004, pp. 292–295. Translated from Doklady Akademii Nauk, Vol. 396, No. 3, 2004, pp. 328–331.*
*Original Russian Text Copyright © 2004 by Dmitriev, Evteev, Ievlev, Kosilov.*

## TECHNICAL PHYSICS

# Structural Self-Organization in a (Crystal–Monolayer Film) Metallic Heterogeneous System with Large Dimensional Discrepancy between the Components

**A. A. Dmitriev*, A. V. Evteev, Corresponding Member of the RAS V. M. Ievlev, and A. T. Kosilov**

Received February 11, 2004

Molecular dynamic simulation with multiparticle potentials calculated by the embedded-atom method shows that a [(001)Pd–75% Pd–25% Ni solid-solution monolayer–79% Pd–21% Ni solid-solution monolayer] heterostructure is formed due to structural–morphological transformations and diffusion exchange between Ni and Pd atoms in a system of the Ni monolayer on the (001)Pd singular surface. The formation of two adjacent solid-solution monolayers ensures their coherent connection by means of elastic deformation and explains the pseudomorphism of subnanofilms with large dimensional discrepancy between the components of the original heterostructure.

## INTRODUCTION

The structural self-organization of subnanofilms in metallic heterogeneous systems with relatively large dimensional discrepancy was studied in numerous experimental works with the use of methods of analyzing the structure and electron properties of surfaces (see, e.g., [1–5]). The problem of structural and morphological stability of such systems is of current interest due to both the development of the methods of modifying the properties of surfaces (catalysis, micro- and nanoelectronics) and the creation of multilayer short-period heterostructures for various purposes.

Although current diffraction, spectroscopic, and microscopic methods are undoubtedly highly informative, they cannot follow the dynamics of structural, substructural, and morphological transformations in nanoflims at the level of displacements of individual atoms. The molecular dynamic method can fill this gap at the current stage.

In this work, we apply the molecular dynamic method to analyze the properties of the structural–morphological evolution of a monolayer film of one metal (Ni) on the singular surface of another metal (Pd) and to estimate the possibility of coherent connection (pseudomorphism) for a system with dimensional discrepancy close to the theoretical limit $\left(f_0 = \frac{a_2 - a_1}{a_1} = -0.094\right)$. This system is taken because it has no fundamental limitations on the mutual solvability of the components in massive samples [6].

## COMPUTER EXPERIMENT PROCEDURE

A substrate is simulated in the form of a calculation cell consisting of 8 atomic layers each with 900 atoms. Periodic boundary conditions are imposed on the system in the [110] and $[1\bar{1}0]$ directions. Three lower and five subsequent layers from the bottom of the calculation cell are treated as static and dynamic, respectively. An original Ni monolayer is simulated by randomly placing 900 atoms on the substrate surface. After check-up of distances between them, the largest overlappings are removed step by step, and the static relaxation of the system is induced. Interaction between atoms is described by multiparticle potentials calculated by the embedded atom method [7].

Further, the velocities of Ni and Pd atoms (in dynamic layers) are specified according to the Maxwell distribution for a temperature of 20 K, and successive molecular dynamic annealings of the system are carried out at ambient temperatures $T_e$ = 20, 200, 400, 600, 800, 1000, 1200, 1400, and 1600 K. Molecular dynamic calculation is performed by integrating the equations of motion of atoms with time step $\Delta t = 1.5 \times 10^{-15}$ following the Verlet algorithm [8]. Molecular dynamic annealings are carried out as follows: the system is first under isothermal conditions (at given $T_e$) for $1000\Delta t$ and, then, under adiabatic conditions for $19\,000\Delta t$. Thus, molecular dynamic annealing at each ambient temperature takes $20000\Delta t$ or $3 \times 10^{-11}$ s. After each molecular dynamic annealing, the system is transferred to the state with $T$ = 0 K by the static relaxation

---

*Voronezh State Technical University,*
*Moskovskiĭ pr. 14, Voronezh, 394026 Russia*
** e-mail: mfm@fm.vorstu.ac.ru*

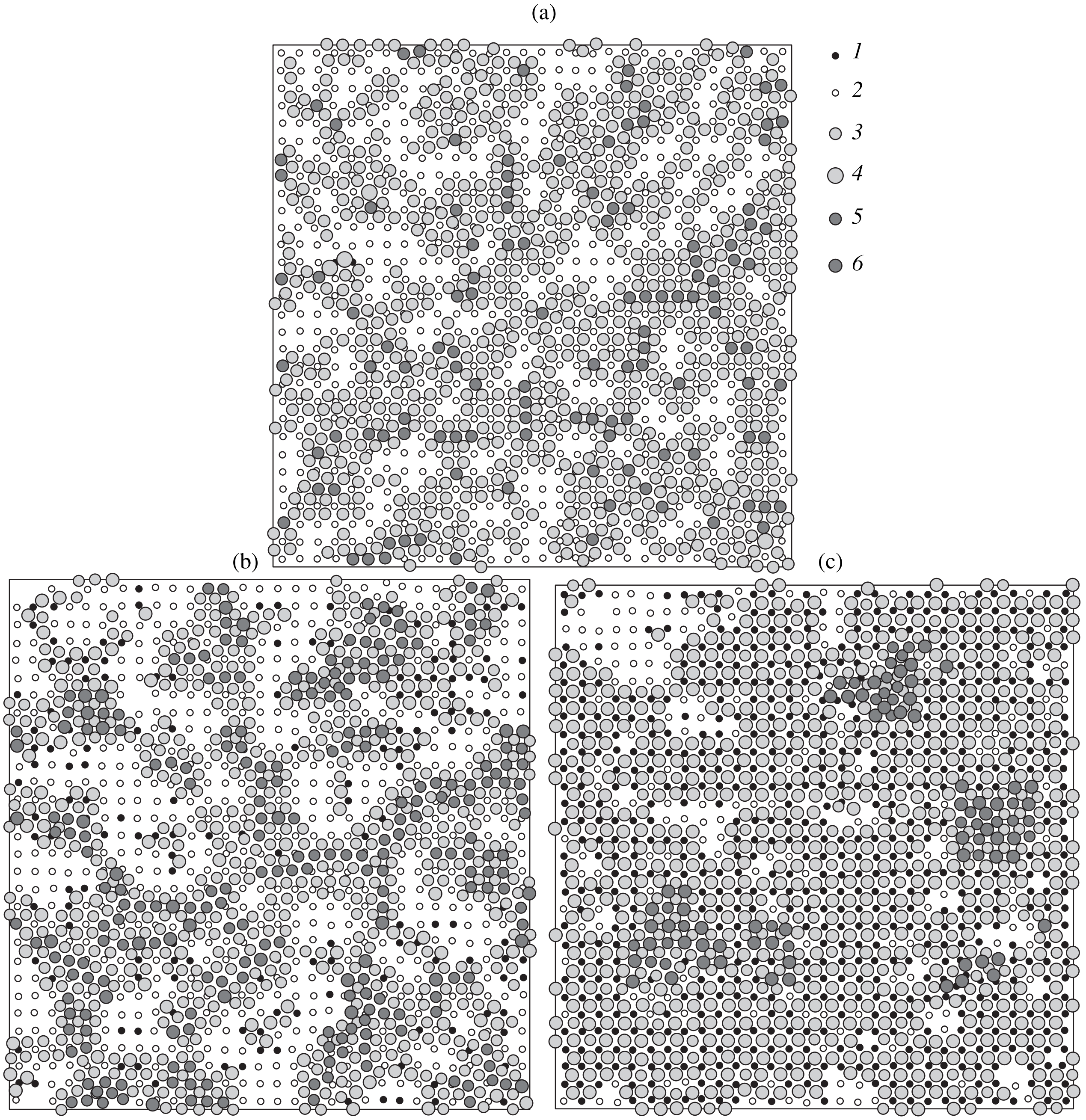

**Fig. 1.** Structural transformations in the Ni monolayer–(001)Pd system: (a) substrate–film heterostructure after the formation and static relaxation of the model and after isothermal annealing at an ambient temperature of 1000 K for (b) $3 \times 10^{-11}$ and (c) $51 \times 10^{-11}$ s; (*1*) Ni and (*2*) Pd atoms in the upper layer of the substrate, (*3*) Ni and (*4*) Pd atoms in the first layer of the film, and (*5*) Ni and (*6*) Pd atoms in the second and third layers of the film.

method in order for atoms to take equilibrium positions in local potential wells. This procedure provides detailed analysis of atomic configurations without thermal background.

## RESULTS AND DISCUSSION

Visual analysis of the Ni layer immediately after its formation and static relaxation shows that atoms are irregularly distributed over the substrate surface and form a ramified cluster structure consisting of atomic groups united into mono- and bilayer island clusters. Clusters in the form of pentagonal rings that are sometimes completed up to pentagonal pyramids are observed on the substrate surface (see Fig. 1a).

When temperature $T_e$ increases to 400 K, Ni atoms of monolayer fragments of the structure are grouped

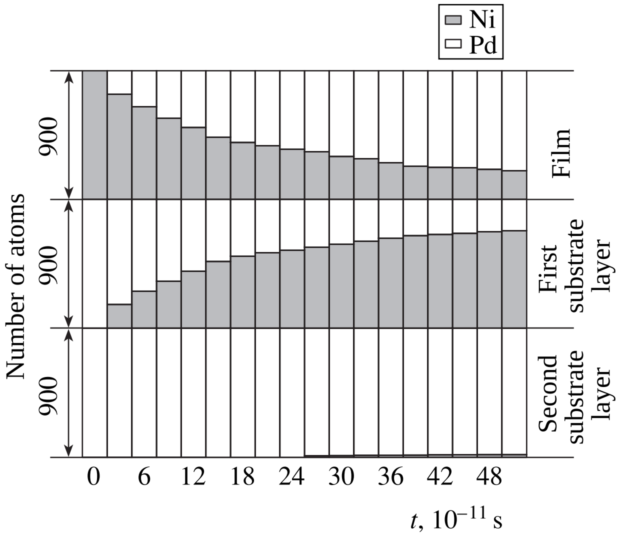

**Fig. 2.** Time dependence of the concentration of Ni and Pd atoms in the substrate and film upon isothermal annealing at an ambient temperature of 1000 K.

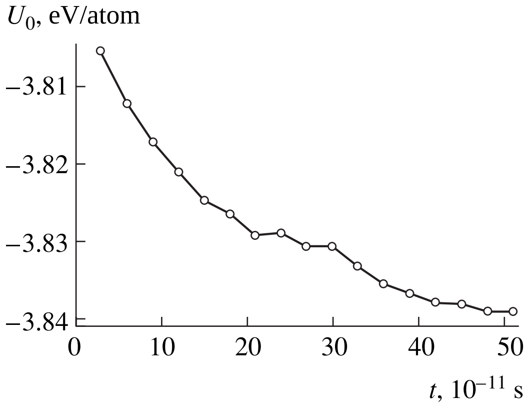

**Fig. 3.** Time dependence of the potential energy of the model after static relaxation in the process of isothermal annealing at an ambient temperature of 1000 K.

into new bi- and trilayer clusters. Atoms of the second and third layers are rearranged with the formation of planar close-packed (hexagonal symmetry) structures, whereas the first layer remains oriented parallel to the substrate. With an increase in temperature, mutual exchange proceeds between Ni atoms of clusters and Pd atoms of the first substrate layer. The number of such exchanges increases sharply beginning with 800 K.

To study the properties of the diffusion rearrangement of the cluster structure, the original system is annealed at 1000 K. The structure is periodically analyzed with a step of $3 \times 10^{-11}$ s (300–350 oscillations of atoms). Similarly to isochron annealing, the monolayer disperses at the initial stage with the formation of new bi- and trilayer clusters (Fig. 1b), whose number increases for the first $6 \times 10^{-11}$ s. The intense exchange between Ni atoms from clusters and Pd atoms from the first layer of the substrate is observed for $39 \times 10^{-11}$ s. Nickel atoms located only at the periphery of clusters and in the first layer of clusters are involved in the exchange. Nickel atoms of the first layer that are surrounded by neighbors are not involved in diffusion exchange with substrate atoms. Diffusion exchange increases the concentration of Ni atoms in the first layer of the substrate and Pd atoms in clusters. Palladium atoms coming from the substrate diffuse into the second layer of clusters and cover the first Ni layer. After $39 \times 10^{-11}$ s, the 900 atoms that are located on the substrate surface and form the cluster structure include 666 Pd atoms and 234 Ni atoms. In this case, among the 666 Ni atoms leaving clusters, 651 atoms get the first layer of the substrate and only 15 atoms get the second layer.

With an increase in the Pd concentration in clusters, their morphology changes. Owing to lateral development, multilayer island clusters are successively united due to a decrease in the number of atoms in the second and third layers and form a monolayer structure in parallel orientation. The monolayer is uniformly filled with Pd (79%) and Ni (21%) atoms (disregarding a few atoms remaining in the second and third layers of clusters) and the upper layer of the substrate is uniformly filled with Ni (75%) and Pd (25%) atoms without indications of the structural ordering of solutions. The concentration of Ni atoms in the second layer of the substrate does not exceed 2.22% (Fig. 2). All stages of the self-organization of the system into such a heterostructure are accompanied by a monotonic decrease in its potential energy (Fig. 3).

The driving force of such an efficient atomic rearrangement of the heterostructure is associated with dimensional discrepancy between the components. The final result, i.e., atomic mixing in two monolayers, partially compensates discrepancy. According to [6], the discrepancy between the Pd crystal and modified upper layer of the substrate (consisting of 75% Ni and 25% Pd) is equal to –0.065, whereas the discrepancy between the monolayers of solid solutions is equal to 0.05. A decrease in the discrepancy between monolayers provides the possibility of their elastic accommodation and coherent connection (as is seen in Fig. 1c) at both interfaces (which is enhanced by the second-layer effect with the opposite discrepancy sign). The revealed diffusion rearrangement of the original heterostructure that ensures coherent connection in the film heterogeneous system with large dimensional discrepancy can provide a basis for explaining pseudomorphism in similar systems (e.g., Pt–Cu [3], Pt–Ni [4], etc.) by the low-energy electron diffraction method.

The above results show that oriented monolayer heterostructures with a pronounced gradient of the composition can be realized even in systems with the unlimited mutual solvability of the components.

## REFERENCES

1. C. Boeglin, B. Carriere, J. P. Deville, *et al.*, Surf. Sci. **211–212**, 767 (1989).
2. S. S. Chao, E. A. Knabbe, and R. W. Vook, Surf. Sci. **100**, 581 (1980).
3. G. W. Graham, P. J. Schmitz, and P. A. Thiel, Phys. Rev. B **41**, 3353 (1990).
4. J. A. Barnard and J. J. Ehrhardt, J. Vac. Sci. Technol. A **8**, 4061 (1990).
5. Y. S. Li, J. Quinn, H. Li, *et al.*, Phys. Rev. B **44**, 8261 (1991).
6. O. M. Barabash and Yu. N. Koval’, *Handbook on the Structure and Properties of Metals and Alloys* (Naukova Dumka, Kiev, 1986).
7. S. M. Foiles, Phys. Rev. B **32**, 3409 (1985).
8. L. Verlet, Phys. Rev. **159**, 98 (1967).

*Translated by R. Tyapaev*

*Doklady Physics, Vol. 49, No. 5, 2004, pp. 296–302. Translated from Doklady Akademii Nauk, Vol. 396, No. 3, 2004, pp. 332–338.*
*Original Russian Text Copyright © 2004 by Chuvil'deev, Kopylov, Nokhrin, Makarov, Lopatin.*

**TECHNICAL PHYSICS**

# Dispersion Limit upon Equal-Channel Angular Pressing. Temperature Effect

**V. N. Chuvil'deev*, V. I. Kopylov**, A. V. Nokhrin*,**
**I. M. Makarov*, and Yu. G. Lopatin***

Presented by Academician O.A. Bannykh January 22, 2004

Received January 22, 2004

Experimental and theoretical results concerning the deformation refining of grains upon intense plastic deformation are reported. Experimental results on deformation dispersion of pure metals and alloys based on magnesium and aluminum are summarized. A model is developed to calculate the minimum grain size that can be obtained by the method of equal-channel angular pressing (ECAP). Expressions describing the grain refining limit as a function of material properties and temperature of intense plastic deformation are obtained.

## INTRODUCTION

As is known, developed plastic deformation is accompanied by intense fragmentation, i.e., by the formation of disoriented microdomains, or fragments, in a material. With the development of deformation, the disorientation of fragments increases and their sizes decrease gradually to a certain minimum $d^*$, usually called the deformation refining or dispersion limit. This limiting value depends on the material properties, deformation temperature, and kind and method of deformation. Although the formation of microcrystalline structures by the methods of intense plastic deformation was studied in numerous experimental works, the origin of the refining limit has not yet been revealed, and this limit has not yet been calculated theoretically. In this work, the deformation-temperature dependence of $d^*$ is studied both experimentally and theoretically and a model is developed to calculate the dispersion limit.

The work is based on, first, experimental results concerning the structure and properties of numerous metals and alloys subjected to ECAP [1] and, second, the theories of large plastic deformations [2] and nonequilibrium grain boundaries [3, 4].

## MODEL

In the process of intragrain plastic deformation under external stresses, defects are accumulated at the internal boundaries of a polycrystal. The defect layer arising at boundaries is generally a complicated system of dislocation and disclination defects [3, 4]. In the first approximation, this defect layer is treated as a system of independent plane distributions of dislocations and a system of junction disclinations [3, 5].

Defects, primarily junction disclinations, formed at boundaries generate intense internal stress fields $\sigma_i$, inducing accommodation intragrain slip. It is important that fields generated by junction disclinations for large plastic deformations are so strong that the accommodation motion of dislocations in grains becomes collective. These collective motions are described by using the concept of nucleation of peculiar defects, so-called broken dislocation boundaries, and their motion through a crystal [2, 5]. Broken dislocation boundaries, intersecting with each other, are responsible for the gradual fragmentation of the crystal.

In view of the above discussion, the force condition of fragmentation can be represented as the condition on the intensity of internal stress fields $\sigma_i$ generated by junction disclinations. These stresses must be enough to induce plastic deformation in grains, i.e., $\sigma_i \geq \sigma_1$.

In a rough approximation, stress $\sigma_1$ can be taken to be proportional to the yield strength of the material: $\sigma_1 \sim \psi\sigma_y$. In this case, using the standard expression $\sigma_y = \sigma_0 + \frac{K}{\sqrt{d}}$, where $\sigma_0$ is the stress induced by obstacles for slip of dislocations in the lattice, $K$ is the Hall–Petch coefficient, and $d$ is the grain size, we obtain $\sigma_1 =$

---

* *Research Physicotechnical Institute,*
*Nizhni Novgorod State University, pr. Gagarina 23,*
*Nizhni Novgorod, 603950 Russia*
*e-mail: chuvildeev@nifti.unn.ru, nokhrin@nifti.unn.ru,*
*makarov@nifti.unn.ru, lopatin@nifti.unn.ru*

** *Institute of Physics and Technology,*
*Belarussian Academy of Sciences,*
*ul. Surganova 6, Minsk, 220012 Belarus*
*e-mail: kpl@hmti.ac.by*

1028-3358/04/4905-0296$26.00 © 2004 MAIK "Nauka/Interperiodica"

$\psi\left(\sigma_0 + \frac{K}{\sqrt{d}}\right)$. In the first approximation, $\sigma_i = \phi G\omega$ [6], where $\omega$ is the intensity of junction disclinations, $\phi$ is a geometric factor of about unity, and $G$ is the shear modulus. In this case, the force condition of fragmentation has the form $\omega \geq \frac{\sigma_1}{\phi G}$, or

$$\omega \geq \omega^* = \chi\left(\frac{\sigma_0}{G} + \frac{K}{G\sqrt{d}}\right) \approx \frac{1}{\sqrt{d}}, \qquad (1)$$

where $\chi = \frac{\psi}{\phi}$ is the geometric factor and $\omega^*$ is the critical intensity of junction disclinations at which the emission of broken dislocation walls from junctions (fragmentation) begins. In microcrystal materials, the term $\frac{K}{\sqrt{d}}$ is usually much larger than $\sigma_0$ and the fragmentation condition takes the form

$$\omega \geq \omega^* = \frac{\chi K}{G\sqrt{d}} \sim \frac{1}{\sqrt{d}}.$$

It is fundamentally important that fragmentation is treated as an accommodation process, i.e., a process that is generated by internal stresses $\sigma_i$ and ensures the relaxation of elastic energy accumulated upon deformation (in this model, this energy is primarily accumulated in junction disclinations). Such a representation can be obviously extended, because accommodation process other than fragmentation can exist upon developed plastic deformation. Under certain conditions, these processes can be more effective (i.e., proceed with a higher rate) than fragmentation. In this case, refining of the grain structure can stop despite continuing deformation.

The diffusion mass transfer was considered in [3, 4] as a mechanism of the accommodation of junction disclinations that differs from fragmentation. The problem of the kinetics of varying the intensity of a disclination dipole was solved in [3] both with allowance for variation in its arm $d$ and in the simplest approximation $d$ = const. It was shown that, in the first approximation, the kinetics of varying the intensity of junction disclinations upon intragrain deformation with rate $\dot{\varepsilon}_V$ is described by the equation $\dot{\omega} = \xi\dot{\varepsilon}_V - \frac{\omega}{t_r}$, where $\xi$ is the geometric factor characterizing the degree of deformation homogeneity [3] and $t_r$ is the characteristic time of diffusion accommodation. In the dipole approximation ($d$ = const), we have [3]

$$t_r = \frac{A_1 d^3}{\delta D_b^*}\frac{kT}{G\Omega}.$$

The parameters are given in Table 1.

In the first approximation for $D_b^*$ = const, $\omega(t)$ has the simple form

$$\begin{gathered}\omega(t) = \omega^{st}\left(1 - \exp\left(-\frac{t}{t_r}\right)\right), \\ \omega^{st} = \xi\dot{\varepsilon}_V t_r \approx A_1\frac{\xi\dot{\varepsilon}_V d^3}{\delta D_b^*}\frac{kT}{G\Omega}.\end{gathered} \qquad (2)$$

For small times ($t \ll t_r$), the intensity of disclinations increases with strain as $\omega(t) - \xi\dot{\varepsilon}_V t \approx \xi\varepsilon_V$. For large times ($t \geq t_r$), the intensity reaches a stationary value $\omega^{st}$ that depends on the dipole arm $d$, i.e., the grain (fragment) size; temperature; strain rate; and grain-boundary diffusion coefficient $D_b^*$ determined by the activation energy $Q_b^*$ and pre-exponential factor $D_{b0}^*$. It is worth noting that the determination of the diffusion coefficient $D_b^* = D_{b0}^*\exp\left(-\frac{Q_b^*}{kT}\right)$ in boundaries with a high density of introduced defects is a nontrivial problem which can be solved by using the theory of nonequilibrium boundaries of grains [4].

As was shown in [4], the activation energy of grain-boundary diffusion in nonequilibrium boundaries of grains depends strongly on the excess free volume associated with defects introduced into the boundary. For low densities of introduced defects, we have ordinary values $Q_b \sim 9kT_m$. For high densities of defects, the excess free volume can be so large that the activation energy of grain-boundary diffusion becomes equal to the activation energy of diffusion in a melt $Q_L \sim 3kT_m$ [4].

Substituting the maximum intensity of disclinations $\omega = \omega^{st}$ given by Eqs. (2) into Eq. (1), we represent the fragmentation condition in the form $A_1\frac{d^3\xi\dot{\varepsilon}_V}{\delta D_b^*}\frac{kT}{G\Omega} \geq \omega^*$. According to this condition, fragmentation is possible only for certain relations between the parameters $d$, $\dot{\varepsilon}_V$, and $D_b^*$. We represent this relation in the form of the condition for the fragment size:

$$(d^*)^{3.5} \geq \chi\frac{K}{G}\frac{\delta D_b^*}{A_1\xi\dot{\varepsilon}_V}\frac{G\Omega}{kT}. \qquad (3)$$

According to this condition, when a certain size $d \sim d^*$ is reached, fragmentation becomes impossible, because the rate of the accommodation of junction disclinations for small fragments becomes so high that the intensity of junction disclinations cannot reach the critical value $\omega^*$ necessary for the emission of a broken dislocation wall, i.e., for fragmentation.

**Table 1.** Parameters used in calculations [4, 7]

| Parameter | Cu | Mg | Al |
|---|---|---|---|
| Activation energy of self-diffusion in a melt $Q_L$, $kT_m$ | 3.6 | – | 3.8 |
| Activation energy of self-diffusion in the equilibrium boundaries of grains $Q_b$, $kT_m$ | 9.2 | 11.9 | 10.7 |
| Pre-exponential factor of the grain-boundary diffusion coefficient $\delta D_{b0}$, $10^{15}$ m$^3$/s | 5.0 | $5 \times 10^3$ | 50 |
| Pre-exponential factor of the diffusion coefficient in a melt $D_{L0}$, cm$^2$/s | $8 \times 10^{-4}$ | | |
| Burgers vector $b$, $10^{10}$ m | 2.56 | 3.21 | 2.86 |
| Boundary width $\delta$ | $2b$ | | |
| Atomic volume $\Omega$, $10^{23}$ cm$^3$ | 1.18 | 2.33 | 1.66 |
| Melting point $T_m$, K | 1356 | 924 | 933 |
| Shear modulus $G$, GPa | 42 | 17 | 25 |
| Relative free volume of the boundary $\alpha$ | 0.35 | | |
| Critical free volume of the boundary $\alpha^*$ | 0.5 | | |
| Excess free volume of the boundary $\Delta\alpha$ | 0.02; 0.01 | | |
| Specific melting heat $\lambda$ | $\lambda\rho b^3 = 1.5kT_m$ | | |
| Density $\rho$ | | | |
| Enthalpy of the liquid–crystal interface $\gamma^0_{S/L}$ | $\gamma^0_{S/L}b^2 = 1kT_m$ | | |
| Entropy of the liquid–crystal interface $S_{S/L}$ | $S_{S/L}b^2 = 0.8\,k$ | | |
| Free energy of the $S$ phase of the boundary $\gamma_0$ | $\gamma_0 b^2 \simeq 1.4kT_m$ | | |
| Hall–Petch coefficient $K$, MPa mm$^{1/2}$ | 1.5 | 3.0 | 3.0 |
| Plastic deformation homogeneity coefficient $\xi$ | $10^{-4}$ | | |
| Numerical parameter $A_1$ | 10 | | |

Thus, the development of the diffusion accommodation of junction disclinations leads to the existence of the limit of the deformation refining of grains, i.e., the minimum size of grains that cannot be reduced under given conditions ($\dot{\varepsilon}$, $T$) of plastic deformation of the material. This minimum size of grains is given by Eq. (3).

## TEMPERATURE DEPENDENCE OF $d^*$

We consider the temperature effect on each parameter entering into Eq. (3).

### *Temperature Dependence of the Strain Rate*

According to the description of ECAP [1], Eq. (3) involves the local rate of intragrain strain $\dot{\varepsilon}_v$, which depends on local internal stresses $\sigma^*$ arising in the deformation center, as well as on deformation temperature. According to [7], for relatively low temperatures and high stresses, the intragrain-strain rate $\dot{\varepsilon}_v$ is determined by slip of dislocations that is limited by their interaction with obstacles [7]:

$$\dot{\varepsilon}_v^{\mathrm{I}} = \dot{\varepsilon}_0 \exp\left[-\frac{\Delta F}{kT}\left(1-\frac{\sigma^*}{\sigma_0}\right)\right], \qquad (4)$$

where $\dot{\varepsilon}_0 = \rho_v b V_0$, $\Delta F$ is the free energy necessary for overcoming obstacles, $\sigma_0$ is the stress necessary for overcoming obstacles at zero temperature, $\rho_v$ is the density of lattice dislocations, $b$ is the Burgers vector, and $V_0$ is the characteristic velocity of dislocations. The $\Delta F$ and $\sigma_0$ values depend on the origin of obstacles and, in pure metals, are primarily determined by the type of the interatomic bond. We emphasize that, according to [7], the $\Delta F$ and $\sigma_0$ values in fcc metals ($\frac{\Delta F}{kT_m} < 10^{-5}$ and $\frac{\sigma_0}{G} < 10^{-5}$) considerably differ from the respective values in transition bcc metals ($\frac{F}{kT_m} = 3.2 \pm 0.7$ and

$\frac{\sigma_0}{G} = (1 \pm 0.4) \times 10^{-2}$) [7]. This difference is one of the main reasons why fcc and bcc metals are classified among different isomechanical groups [7].

For high temperatures, the intragrain strain rate $\dot{\varepsilon}_v^{\mathrm{II}}$ is determined by the diffusion accommodation rate and is expressed as [7]

$$\dot{\varepsilon}_v^{\mathrm{II}} = A\frac{G\Omega}{kT}\left(\frac{\sigma^*}{G}\right)^n \times\left[\frac{D_{v0}}{b^2}\exp\left(-\frac{Q_v}{kT}\right)+\frac{\rho_c a^2}{b^2}D_{c0}\exp\left(-\frac{Q_c}{kT}\right)\right]. \qquad (5)$$

Here, $D_{v0}$ and $D_{c0}$, as well as $Q_v$ and $Q_c$, are the pre-exponential factors, as well as the activation energies, for the volume diffusion and diffusion through dislocation center, respectively; $n$ characterizes the sensitivity of the strain rate to stress $\sigma$, is noticeably different for different materials, and usually lies from 3 to 10; and $A$ is the Dorn constant [7].

The equality $\dot{\varepsilon}_v^{\mathrm{I}} = \dot{\varepsilon}_v^{\mathrm{II}}$ is used to calculate the temperature for pure metals at which the dependence of $\dot{\varepsilon}_v^{\mathrm{I}}$ is replaced by the dependence of $\dot{\varepsilon}_v^{\mathrm{II}}$. Under the assumption $a^2\rho_c D_c \gg D_v$, the transition temperature is expressed as

$$\frac{T_1}{T_{\mathrm{m}}} = Q_c - \frac{\Delta F\left(1-\frac{\sigma^*}{\sigma_0}\right)}{\ln ZkT_{\mathrm{m}}},$$

where

$$Z = A\frac{G\Omega}{kT}\left(\frac{\sigma^*}{G}\right)^n\left(\frac{D_{c0}}{V_0 b}\right).$$

For the ordinary parameters $A$ = (fcc) $10^6$ and (bcc) $10^8$ [7], $\frac{G\Omega}{kT_{\mathrm{m}}} = 50$, $n = 5$, $D_{c0} = 10^{-2}$ cm$^2$/s, $V_0 = 10^{-2}$ cm/s, $Q_c = 10kT_{\mathrm{m}}$, and $\frac{\sigma^*}{G} = 10^{-2}$ typical for ECAP, the transition temperature for fcc (where $\Delta F\left(1-\frac{\sigma}{\sigma_0}\right) \ll Q_c$) and bcc (where $\Delta F\left(1-\frac{\sigma}{\sigma_0}\right) \sim 3$) metals is equal to $0.65T_{\mathrm{m}}$ and $0.33T_{\mathrm{m}}$, respectively.

### Temperature Dependence of the Coefficient K

The temperature dependence of the Hall–Petch coefficient is virtually unstudied. Certain data indicate that $K$ varies slightly with temperature in the range $(0.1–0.5)T_{\mathrm{m}}$. Below, the temperature dependence $K(T)$ will be disregarded when estimating $d^*$.

**Table 2.** Temperature effect on the minimum grain size upon equal-channel angular pressing of pure metals for $T_{\mathrm{def}}$ = 293 K (according to V.I. Kopylov)

| Metal | $T_{\mathrm{m}}$, K | $T_{\mathrm{def}}/T_{\mathrm{m}}$ | $N$ | $d^*$, μm |
|---|---|---|---|---|
| Al | 933 | 3.18 | 8 | 1.3 |
| Cu | 1356 | 4.63 | 12 | 0.3 |
| Ni | 1726 | 5.89 | 12 | 0.1 |
| Fe | 1808 | 6.17 | 10 | 0.1 |

### Effect of Deformation-Stimulated Growth of Grains

With an increase in the temperature of ECAP, the deformation-stimulated growth of grains is possible (see, e.g., [3]). This process can significantly affect the $d^*$ value measured after the completion of deformation and thereby distort the $d^*(T)$ dependence. To exclude the effect of the deformation-stimulated growth of grains, deformation must be carried out at temperatures lower than the recrystallization temperature of a small-crystal material. Approaches to calculation of this temperature were given in [8]. Below, comparing the results with experimental data, we consider (when it is possible) only materials and conditions for which the deformation temperature does not exceed the recrystallization temperature.

## COMPARISON WITH EXPERIMENTAL DATA

### Pure Metals

Detailed data on the deformation-temperature effect on the size of grains are given only in a few papers. However, the results of investigations of intense plastic deformation to the dispersion limit in various pure metals at room temperature $T$ = 293 K are available. Since the melting points $T_{\mathrm{m}}$ of these materials are different, the dependence of the grain refining limit reached in them on the inverse homological temperature $\frac{T_{\mathrm{m}}}{T}$ can be used to preliminarily estimate the temperature dependence $d^*(T)$. Table 2 presents the refining limits $d^*$ reached in various pure metals subjected to ECAP at room temperature. Figure 1 shows $d^*$ values obtained upon torsion under quasi-hydrostatic pressure when deforming bcc metals [9–13].

We analyze these results by using the above model of the refining limit and plot the quantity $y = 3.5\ln\frac{d^*}{b}$ as a function of the inverse homological temperature $x = \frac{T_{\mathrm{m}}}{T}$ (Fig. 1). As is seen, this function for each group

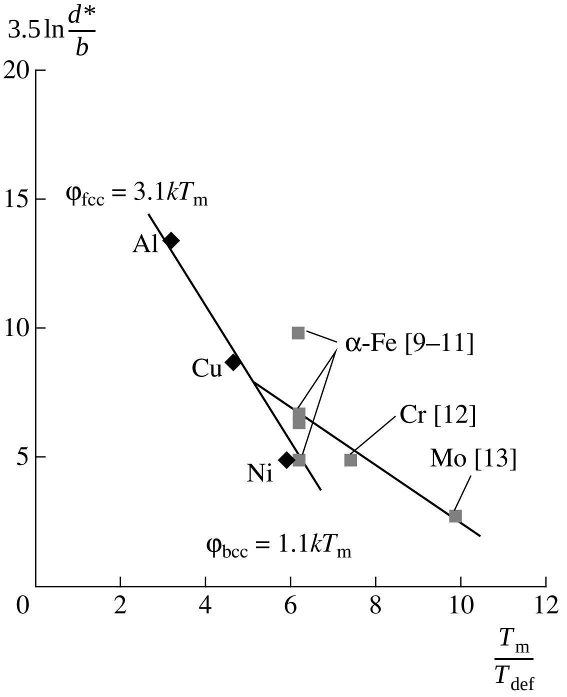

**Fig. 1.** Minimum grain size vs. the deformation temperature for pure fcc (equal-channel angular pressing, Table 2) and bcc (quasi-hydrostatic pressure) metals [9–13] for $T = 20°\mathrm{C}$.

of materials is a linear function $y = A - \varphi x$ with a slope of $\varphi_1 \sim 3.1$ for fcc metals and $\varphi_2 \sim 1.1$ for bcc metals. According to the above theory,

$$\varphi = \frac{Q_b^*}{kT_m} - \frac{\Delta F}{kT_m}1 - \frac{\sigma^*}{\sigma_0}. \tag{6}$$

(Room temperature at which deformation was carried out for these materials is obviously below the transition temperature $T_1$. Therefore, the temperature dependence of $\dot{\varepsilon}_v$ in Eq. (3) must be described by the expression for $\dot{\varepsilon}_v^{\mathrm{I}}$.) For fcc metals, according to the theory developed in [7], the second term in the expression for $\varphi$ is small and $\varphi_1 \approx Q_{\mathrm{b}}^*$, i.e., $\frac{Q_{\mathrm{b}}^*}{kT_m} \approx 3.1$. For bcc metals, where $\frac{\Delta F}{kT_m} \approx 3$ and $\left(1 - \frac{\sigma}{\sigma_0}\right) \sim 1$ according to [7] and $\varphi_2 \approx Q_{\mathrm{b}}^* - 3$, we have $Q_{\mathrm{b}}^* \sim 4.1kT_m$. Thus, $Q_{\mathrm{b}}^* = (3.1\text{–}4.1)kT_m$ for both groups of metals.

The $Q_{\mathrm{b}}^*$ values obtained above are very close to the activation energy $Q_L \sim (3\text{–}4)kT_m$ of diffusion in melts. This striking result is easily interpreted in the framework of the theory of nonequilibrium boundaries of grains [4] and means that, due to the excess content of defects, the free volume of boundaries in metals subjected to ECAP reaches the limiting value $\alpha^*$. According to [4], the diffusion activation energy in such boundaries becomes comparable with the activation energy of diffusion in melts.

### *Alloys Containing the Al–Mg System*

Below, we will discuss the results of direct investigations of the deformation-temperature effect on the dispersion limit in alloys containing the Al–Mg system.

**Al–Mg–Sc–Zr alloys.** Table 3 presents data on the temperature dependence of the dispersion limit in the alloys Al–*x*Mg–0.22% Sc–0.15% Zr (with magnesium content $x = 0$, 1.5, and 3%). Six cycles of ECAP were carried out at 100, 160, and 200°C. Experimental val-

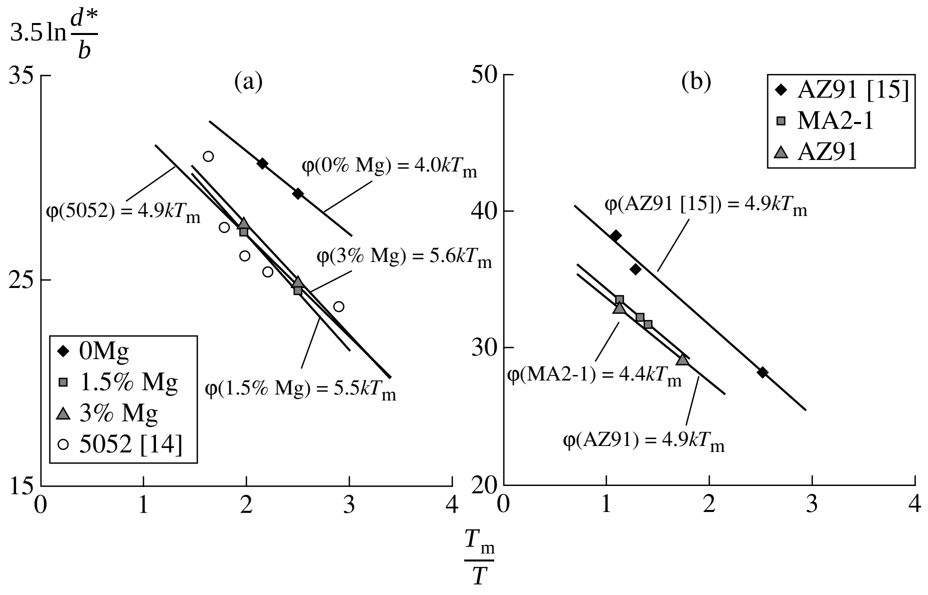

**Fig. 2.** Minimum grain size vs. the deformation temperature for (a) Al–Mg and (b) Mg–Al alloys.

**Table 3.** Effect of the deformation temperature on the grain refining limit for Al–Mg and Mg–Al alloys subjected to equal-channel angular pressing

| Alloy | Experiment | | | | Calculation | | |
|---|---|---|---|---|---|---|---|
| | $T_{\mathrm{def}}$, °C | $T_{\mathrm{m}}/T_{\mathrm{def}}$ | $d^*$, μm | $Q_{\mathrm{b}}^*$, $kT_{\mathrm{m}}$ | $\dot{\varepsilon}_v$, $\mathrm{s}^{-1}$ | $Q_{\mathrm{b}}^*$, $kT_{\mathrm{m}}$ | $d^*$, μm |
| Al–22% Sc–0.15% Zr (V.I. Kopylov) | 100 | 2.50 | 1.2 | 4.0 | $5 \times 10^{-2}$ | 3.8 | 1.04 |
| | 160 | 2.15 | 1.8 | | | | 1.46 |
| Al–1.5% Mg–0.22% Sc–0.15% Zr (Kopylov) | 100 | 2.50 | 0.3 | 5.5 | $5 \times 10^{-2}$ | 5.5 | 0.33 |
| | 200 | 1.97 | 0.7 | | | | 0.72 |
| Al–3% Mg–0.22% Sc–0.15% Zr (Kopylov) | 100 | 2.50 | 0.35 | 5.6 | $5 \times 10^{-2}$ | 5.5 | 0.38 |
| | 200 | 1.97 | 0.8 | | | | 0.81 |
| 5052 [14] | 50 | 2.89 | 0.25 | 4.9 | $2 \times 10^{-1}$ | 5.5 | 0.14 |
| | 100 | 2.50 | 0.30 | | | | 0.25 |
| | 150 | 2.21 | 0.40 | | | | 0.39 |
| | 200 | 1.97 | 0.50 | | | | 0.55 |
| | 250 | 1.78 | 0.75 | | | | 0.71 |
| | 300 | 1.63 | $2.0^{(*)}$ | | | | 0.88 |
| MA2-1 | 200 | 1.95 | 1.7 | 4.4 | $3 \times 10^{1}$ | 4.5 | 1.78 |
| | 250 | 1.77 | 2.4 | | | | 2.38 |
| | 280 | 1.67 | 2.8 | | | | 2.77 |
| | 380 | 1.40 | 4.0 | | | | 4.07 |
| AZ91 | 150 | 2.18 | 1.3 | 4.9 | $1 \times 10^{2}$ | 4.5 | 1.03 |
| | 380 | 1.42 | $3.4^{(*)}$ | | | | 2.45 |
| AZ91 [15] | 20 | 3.15 | 1.0 | 4.9 | $1 \times 10^{0}$ | 4.5 | 1.23 |
| | 300 | 1.61 | 7.6 | | | | 7.37 |
| | 400 | 1.37 | $15.4^{(*)}$ | | | | 9.57 |
| | 480 | 1.22 | $66.1^{(*)}$ | | | | 11.18 |

* Parameters for processes where the deformation-stimulated growth of grains is observed.

ues of the parameter φ $\left(\text{proportional to the activation energy of grain-boundary diffusion } \varphi \sim \frac{Q_{\mathrm{b}}^*}{kT_{\mathrm{m}}}\right)$ lie in the range (4–5.6)$kT_{\mathrm{m}}$ and depend on the magnesium content. The activation energy $Q_{\mathrm{b}}^*$ of grain-boundary diffusion in the alloy without magnesium is close to $Q_{\mathrm{L}} = 3.8kT_{\mathrm{m}}$ for pure aluminum. The energy $Q_{\mathrm{b}}^*$ in alloys containing 1.5 and 3% magnesium is higher by 1.7$kT_{\mathrm{m}}$ (this increase is attributed to the effect of magnesium on $Q_{\mathrm{b}}^*$). Theoretical $d^*$ values calculated with parameters presented in Table 1 agree well with experimental data (Table 3).

**5052 alloy (Al–2.65% Mg).** The temperature effect on the dispersion limit is most studied in the 5052 alloy [14]. Equal-channel angular pressing was carried out at temperatures from 50 to 300°C with a step of 50°C. Experimental results are presented in Table 3. The parameter φ in the temperature range 50–250°C is equal to 4.9$kT_{\mathrm{m}}$, which differs from the above $Q_{\mathrm{b}}^*$ value for alloys with 1.5–3% Mg only by 0.5$kT_{\mathrm{m}}$. For $T >$ 200°C, a sharp rise is observed on the $Q_{\mathrm{b}}^*(T)$ curve. This rise is associated with the distortion of the dispersion pattern by the deformation-stimulated growth of grains for high temperatures (this circumstance was also noted by the authors of [14]). The $d^*$ values calculated for temperatures 50–300°C with parameters presented in Table 1 are given in Table 3. These values agree well with experimental data except for $T$ = 300°C, at which the dispersion pattern is distorted by the intense growth of grains.

### *Magnesium Alloys*

Table 3 presents the data on the deformation-temperature effect on the dispersion limit in the following magnesium alloys: (i) MA2-1 alloy, $N = 6$ cycles, ECAP temperatures 200, 250, 280, and 380°C; (ii) AZ-91 alloy, ECAP temperatures 150 and 380°C; and (iii) AZ-91 alloy [15], ECAP temperatures 20, 300, 400, and 480°C. Experimental values of the average activation energy $Q_b^*$ of grain-boundary diffusion are presented in Table 3. The $Q_L$ value is taken to be equal to $4.5kT_m$. The $d^*$ values calculated by Eq. (3) with the parameters given in Table 1 are presented in Table 3. As is seen, theoretical $d^*$ values agree well with experimental data.

## ACKNOWLEDGMENTS

This work was supported by the Russian Foundation for Basic Research (project nos. 02-03-33043, 03-02-16923, MAS 03-03-06196); the Ministry of Education of the Russian Federation (project nos. E02-4.0-131, A03-3.17-214); the program "Fundamental Problems of Physics and Chemistry of Nanosystems and Nanomaterials," Russian Academy of Sciences; the Research and Education Center "Physics of Solid Nanostructures" at Nizhni Novgorod University; and the program "Basic Research in Higher Education."

## REFERENCES

1. V. M. Segal, V. I. Reznikov, V. I. Kopylov, *et al.*, *Processes of Metal Forming* (Nauka i Tekhnika, Minsk, 1994).
2. V. V. Rybin, *High Plastic Strain and Fracture of Metals* (Metallurgiya, Moscow, 1986).
3. V. N. Perevezentsev, V. V. Rybin, and V. N. Chuvil'deev, Acta Metall. Mater. **40**, 887 (1992).
4. V. N. Chuvil'deev, Fiz. Met. Metalloved. **81** (5), 5 (1996); **81** (6), 5 (1996); **82** (1), 106 (1996).
5. V. V. Rubin, Vopr. Materialoved., No. 1, 11 (2002).
6. V. A. Likhachev and R. Yu. Khaĭrov, *Introduction into the Theory of Disclinations* (Leningr. Gos. Univ., Leningrad, 1975).
7. H. J. Frost and M. F. Ashby, *Deformation-Mechanisms Maps* (Pergamon, Oxford, 1982; Metallurgiya, Chelyabinsk, 1989).
8. A. V. Nokhrin, E. S. Smirnova, V. N. Chivil'deev, and V. I. Kopylov, Metally, No. 3, 27 (2003).
9. R. Z. Valiev, Yu. V. Ivanisenko, E. F. Rauch, and B. Baudelet, Acta Mater. **44**, 4705 (1996).
10. Yu. V. Ivanisenko, A. A. Sirenko, and A. V. Korznikov, Fiz. Met. Metalloved. **87** (4), 78 (1999).
11. T. I. Chashchukhina, M. V. Degtyarev, L. M. Voronova, *et al.*, Fiz. Met. Metalloved. **91** (5), 75 (2001).
12. N. A. Krasil'nikov, Fiz. Met. Metalloved. **91** (3), 81 (2001).
13. A. V. Korznikov, S. Idrisova, and N. I. Noskova, Fiz. Met. Metalloved. **85** (3), 113 (1998).
14. Y. C. Chen, Y. Y. Huang, C. P. Chang, and P. W. Kao, Acta Mater. **51**, 2005 (2003).
15. K. Kubota, M. Mabuchi, and K. Higashi, J. Mater. Sci. **34**, 2255 (1999).

*Translated by R. Tyapaev*

*Doklady Physics, Vol. 49, No. 5, 2004, pp. 303–307. Translated from Doklady Akademii Nauk, Vol. 396, No. 1, 2004, pp. 47–51.*
*Original Russian Text Copyright © 2004 by Vigdorovich.*

## MECHANICS

# Relation between the Hydrodynamic Parameters of Two Different Turbulent Wall Flows

**I. I. Vigdorovich**

Presented by Academician G.G. Chernyĭ December 3, 2003

Received December 10, 2003

A simple relation between the profiles of the hydrodynamic parameters in a boundary layer on an impermeable plate and those in an asymptotic boundary layer with suction is found for large Reynolds numbers. The profiles of the mean velocity in the outer region (beyond the viscous sublayer) of two flows are related to each other in terms of quadratures. The distributions of shear stress are determined from the velocity profile of one of the flows. Turbulent normal stresses are calculated from the corresponding component of the Reynolds tensor and velocity profile of the other flow.

It is shown that the rms transverse pulsation of the velocity in the intermediate wall region of the boundary layer with suction is proportional to the logarithm of the distances from the wall, whereas the rms longitudinal pulsations, to this logarithm in a power of 3/2.

The results are obtained only from the equations of motion and analysis of dimensions.

**1.** Let us consider a uniform flow of an incompressible fluid in a turbulent boundary layer on a flat smooth plate. The velocity $U_e$ of the flow is constant along the plate length at the outer boundary of the layer and the suction velocity $v_w$ directed along the normal to the surface is also constant.

The gradient of the mean longitudinal velocity and turbulent shear stress are functions of the Cartesian coordinates $x$ and $y$ and determining parameters of the problem:

$$\begin{aligned} \frac{\partial u}{\partial y} &= F_1(x, y, \nu, v_w, U_e), \\ \langle u'v' \rangle &= F_2(x, y, \nu, v_w, U_e). \end{aligned} \tag{1.1}$$

Here, $\nu$ is the kinematic viscosity and the origin of the Cartesian coordinate system is at the leading edge of the plate.

Let

$$\Delta = F_3(x, \nu, v_w, U_e), \tag{1.2}$$

where $F_3$ is a certain function, be the thickness of the boundary layer, i.e., the quantity characterizing the transverse scale of the flow. In what follows, it is convenient to consider various particular definitions of $\Delta$.

Substituting $x$ and $U_e$ expressed from the first of Eqs. (1.1) and Eq. (1.2) into the second of Eqs. (1.1), we arrive at the relation

$$\langle u'v' \rangle = F_4\left(y, \nu, v_w, \Delta, \frac{\partial u}{\partial y}\right), \tag{1.3}$$

where $F_4$ is a certain function. Applying the dimensional analysis to Eq. (1.3), we obtain

$$\begin{gathered} \langle u'v' \rangle = -\left(y\frac{\partial u}{\partial y}\right)^2 S(\mathrm{R_l}, \beta, \eta), \quad \mathrm{R_l} = \frac{y^2}{\nu}\frac{\partial u}{\partial y}, \\ \beta = \frac{v_w}{\mathrm{R_l}\, y\dfrac{\partial u}{\partial y}}, \quad \eta = \frac{y}{\Delta}. \end{gathered} \tag{1.4}$$

The local Reynolds number $\mathrm{R_l}$ is the characteristic turbulent-to-molecular viscosity ratio. The function $S$ appearing in Eqs. (1.4), as well as the functions $F_1, \ldots, F_4$, is a universal function for the class of flows depending on the three parameters $\nu$, $v_w$, and $U_e$. Let it be continuous and differentiable for $0 \le \mathrm{R_l} \le \infty$, $-\infty \le \beta \le 0$, and $0 \le \eta \le \infty$ and satisfy the condition $S(\infty, 0, 0) \ne 0$. These conditions are ordinary physical assumptions that viscosity is substantial only in the thin wall region (viscous sublayer), where the outer scale (boundary layer thickness) does not affect the flow.

Relation (1.4) expresses the shear stress in terms of the gradient of the mean velocity. Since the effect of the suction velocity on this relation must weaken with the distance from the wall, the parameter $\beta$ is taken such that the denominator includes the local Reynolds number $\mathrm{R_l}$.

---

*Central Institute of Aviation Motors,*
*ul. Aviamotornaya 2, Moscow, 111116 Russia*
*e-mail: ivigdorovich@ciam.ru*

1028-3358/04/4905-0303$26.00 © 2004 MAIK “Nauka/Interperiodica”

For the normal Reynolds stresses, we similarly obtain

$$\langle u'^2\rangle = \left(y\frac{\partial u}{\partial y}\right)^2 S_1(\mathrm{R}_l, \beta, \eta),$$

$$\langle v'^2\rangle = \left(y\frac{\partial u}{\partial y}\right)^2 S_2(\mathrm{R}_l, \beta, \eta), \qquad (1.5)$$

$$\langle w'^2\rangle = \left(y\frac{\partial u}{\partial y}\right)^2 S_3(\mathrm{R}_l, \beta, \eta),$$

where $S_1$, $S_2$, and $S_3$ are universal functions.

The flow is described by the boundary-layer equations with zero pressure gradient:

$$u\frac{\partial u}{\partial x} + v\frac{\partial u}{\partial y} = -\frac{\partial\langle u'v'\rangle}{\partial y} + \nu\frac{\partial^2 u}{\partial y^2},$$

$$\frac{\partial u}{\partial x} + \frac{\partial v}{\partial y} = 0, \qquad (1.6)$$

$$x > 0\colon\; u(x, 0) = 0, \quad v(x, 0) = v_w, \quad u(x, \infty) = U_e,$$

which, along with closing relation (1.4), specify the boundary value problem for the mean velocity field.

Below, we consider only the outer region of the flow, where molecular viscosity can be disregarded in momentum equation (1.6).

**2.** Let us consider the boundary layer on an impermeable plate. In this case, the velocity defect in the outer region (beyond the viscous sublayer) for large Reynolds numbers satisfies the Karman law [1, 2]

$$\sqrt{\frac{2}{c_\mathrm{f}}}\frac{U_e - u}{U_e} = f(\eta) + O(\sqrt{c_\mathrm{f}}). \qquad (2.1)$$

Here, $c_\mathrm{f}$ is the skin-friction coefficient and $f$ is a certain function.

Let us substitute Eq. (2.1) into Eqs. (1.6) closed with Eq. (1.4) and take the limit $\mathrm{R}_\Delta \equiv \frac{\Delta U_e}{\nu} \to \infty$, $\frac{1}{\eta} = O(1)$. Retaining only leading terms in the momentum equation in view of $c_\mathrm{f} = O(\mathrm{R}_\Delta^{-2})$ according to the Karman friction law [1], we arrive at the equation

$$\frac{d\Delta}{dx}\sqrt{\frac{2}{c_\mathrm{f}}}\eta f' = [(\eta f')^2 S(\infty, 0, \eta)]'.$$

Taking into account the boundary condition $f(\infty) = 0$ and integrating this equation across the layer, we obtain

$$\frac{d\Delta}{dx}\sqrt{\frac{2}{c_\mathrm{f}}}\left(\eta f + \int_\eta^\infty f\,d\eta\right) = (\eta f')^2 S(\infty, 0, \eta). \qquad (2.2)$$

The improper integral on the left-hand side of Eq. (2.2) converges because the right-hand side includes turbulent shear stress vanishing at $\eta = \infty$. The right-hand side of Eq. (2.2) on the wall is equal to unity. Therefore,

$$\frac{d\Delta}{dx}\sqrt{\frac{2}{c_\mathrm{f}}}\int_0^\infty f\,d\eta = 1.$$

Thus, the velocity profile in the outer region satisfies the equations

$$\eta f' = [(\eta f')^2 S(\infty, 0, \eta)]'\int_0^\infty f\,d\eta, \qquad (2.3)$$

$$\eta f + \int_\eta^\infty f\,d\eta = (\eta f')^2 S(\infty, 0, \eta)\int_0^\infty f\,d\eta. \qquad (2.4)$$

Solving Eq. (2.3) as the first-order equation for $\eta f'$, we obtain

$$\eta f'\sqrt{S(\infty, 0, \eta)}\int_0^\infty f\,d\eta = -\int_\eta^\infty \frac{d\eta}{2\sqrt{S(\infty, 0, \eta)}}.$$

Therefore, for $\eta = 0$,

$$\int_0^\infty f\,d\eta = \int_0^\infty \frac{d\eta}{2\sqrt{S(\infty, 0, \eta)}}. \qquad (2.5)$$

The function $f$ behaves logarithmically near the wall:

$$f = -\frac{1}{\kappa}\ln\eta + O(1), \quad \eta \to 0,$$

where the von Karman constant $\kappa = 0.41$ is the quantity $\sqrt{S(\infty, 0, 0)}$.

From Eqs. (1.5), (2.1), and (2.4), the Reynolds tensor components in the outer region of the boundary layer are expressed as

$$-2\frac{\langle u'v'\rangle}{U_e^2 c_\mathrm{f}} = 1 + \frac{\eta f(\eta)}{\int_0^\infty f(\eta)\,d\eta} + O(\sqrt{c_\mathrm{f}}),$$

$$2\frac{\langle u'^2\rangle}{U_e^2 c_\mathrm{f}} = [\eta f'(\eta)]^2 S_1(\infty, 0, \eta) + O(\sqrt{c_\mathrm{f}}),$$

$$2\frac{\langle v'^2\rangle}{U_e^2 c_\mathrm{f}} = [\eta f'(\eta)]^2 S_2(\infty, 0, \eta) + O(\sqrt{c_\mathrm{f}}), \qquad (2.6)$$

$$2\frac{\langle w'^2\rangle}{U_e^2 c_\mathrm{f}} = [\eta f'(\eta)]^2 S_3(\infty, 0, \eta) + O(\sqrt{c_\mathrm{f}}).$$

According to the theoretical investigations [3, 4] corroborated by measurements, the Reynolds tensor component $\langle v'^2\rangle$ related to the transverse pulsations of the velocity behaves near the wall as shear stress. This means that the quantity $S_2(\infty, 0, 0) = \left(\frac{\kappa}{\sigma_2}\right)^2$ exists and is nonzero. According to experimental data, $\sigma_2 = 0.95$ [1].

The behavior of the components $\langle u'^2\rangle$ and $\langle w'^2\rangle$ related to velocity pulsations in the directions parallel to the wall is more complicated:

$$S_1(\infty, 0, \eta) = -A_1\kappa^2\ln\eta + O(1),$$
$$S_3(\infty, 0, \eta) = -A_3\kappa^2\ln\eta + O(1), \quad \eta \to 0, \tag{2.7}$$

where $A_1$ and $A_3$ are universal constants. According to the direct numerical simulation of the flow in the turbulent boundary layer on the plate up to the Reynolds number corresponding to the displacement thickness [5], $R_{\delta^*} = 2000$, $A_1 = 1.1$, and $A_3 = 0.36$.

The velocity profile on the impermeable plate is well known from experimental data and can be specified by the Coles empirical formula [6]

$$f = -\frac{1}{\kappa}[\ln\eta - 0.55(1 + \cos(\pi\eta))],$$
$$0 < \eta \le 1, \quad \int_0^\infty f\,d\eta = \frac{1.55}{\kappa}. \tag{2.8}$$

Here, $\Delta$ is the distance from the wall at which the longitudinal component of the mean velocity differs from $U_e$ by 0.5%.

**3.** As was shown in [7], the limiting form of the flow in the boundary layer with uniform suction in the far downstream region is the asymptotic boundary layer, i.e., a one-dimensional flow, where all mean parameters are functions of only the transverse coordinate.

In this case, the first integral of momentum equation (1.6) has the form

$$-v_w(U_e - u) = \left(y\frac{du}{dy}\right)^2 S(R_l, \beta, \eta) + \nu\frac{du}{dy}. \tag{3.1}$$

From this relation, we obtain $c_f = -\frac{2v_w}{U_e}$ for the skin-friction coefficient.

The solution of Eq. (3.1) in the outer region of the boundary layer is sought in the form

$$\frac{U_e - u}{-v_w} = g(\eta) + O(R_w^{-1}), \quad R_w = -\frac{v_w\Delta}{\nu}. \tag{3.2}$$

Substituting Eq. (3.2) into Eq. (3.1) and taking the limit $R_w \to \infty$ and $\frac{1}{\eta} = O(1)$, we arrive at the equation

$$g = (\eta g')^2 S(\infty, 0, \eta), \quad g(\infty) = 0, \tag{3.3}$$

whose solution has the form

$$2\sqrt{g} = \int_\eta^\infty \frac{d\eta}{\eta\sqrt{S(\infty, 0, \eta)}}. \tag{3.4}$$

Integral (3.4), as well as the function $f$, behaves logarithmically near the wall:

$$2\sqrt{g} = -\frac{1}{\kappa}\ln\eta + O(1), \quad \eta \to 0.$$

Solutions of ordinary differential equations (2.4) and (3.3) are related to each other. Substituting the function $S(\infty, 0, \eta)$ expressed from Eq. (2.4) into Eq. (3.4), we arrive at the relation

$$2\sqrt{g} = -\left(\int_0^\infty f\,d\eta\right)^{1/2} \int_\eta^\infty \left(\eta f + \int_\eta^\infty f\,d\eta\right)^{-1/2} f'\,d\eta. \tag{3.5}$$

Integration of Eq. (3.4) across the layer yields

$$2\int_0^\infty \sqrt{g}\,d\eta = \int_0^\infty d\eta \int_\eta^\infty \frac{d\eta_1}{\eta_1\sqrt{S(\infty, 0, \eta_1)}}$$
$$= \int_0^\infty \frac{d\eta}{\sqrt{S(\infty, 0, \eta)}} = 2\int_0^\infty f\,d\eta. \tag{3.6}$$

The latter equality is obtained by taking Eq. (2.5) into account.

Thus, the velocity profiles of two different turbulent wall flows are related to each other by simple exact expression (3.5).

As the transverse scale for the asymptotic boundary layer with suction, it is convenient to use the integral parameter

$$\Delta_* = 2\int_0^\infty \sqrt{\frac{U_e - u}{-v_w}}\,dy,$$

which, in view of Eqs. (3.2) and (3.6), takes the form

$$\Delta_* = 2\Delta\int_0^\infty f\,d\eta.$$

Figures 1a and 1b show the velocity profiles in the asymptotic boundary layer with suction in the linear

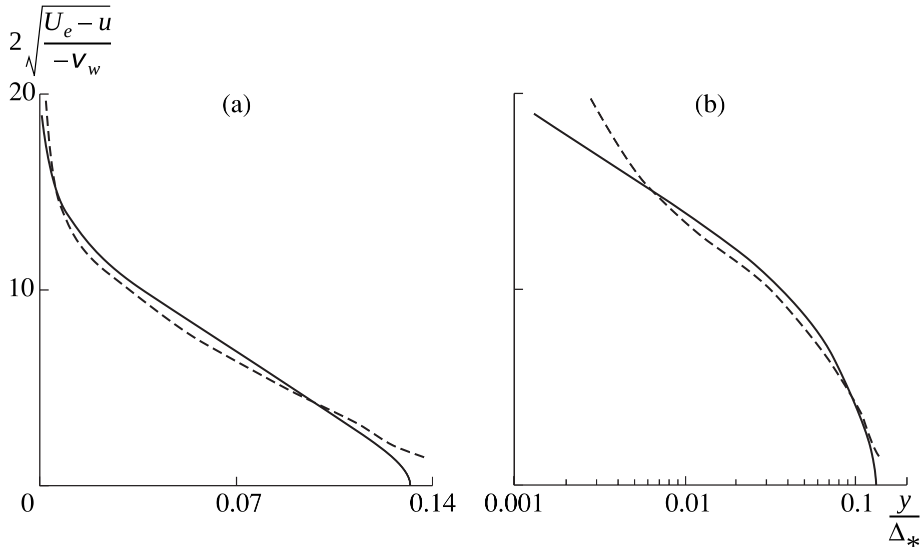

**Fig. 1.** Velocity profiles in the asymptotic boundary layer with suction in the scaling variables in the (a) linear and (b) semilogarithmic scales. Solid lines are calculations by Eq. (3.5) and dashed lines are obtained by the direct numerical simulation carried out in [8, 9].

and semilogarithmic scales, respectively. The solid lines are calculations by Eq. (3.5), where the function $f$ is specified by Coles formula (2.8). The dashed lines are obtained by the direct numerical simulation of the flow for $\frac{v_w}{U_e} = -0.00361$ and $R_{\delta*} = 1000$ [8, 9]. Although the simulation was carried out for a low Reynolds number, the lines in Fig. 1 are close to each other. It is seen in Fig. 1b that, in agreement with the theoretical conclusions, the dashed line has a logarithmic section that is relatively short due to a low Reynolds number. The slope of this section is approximately equal to the slope of the solid line.

According to Eqs. (1.5), (3.2), and (3.3), the Reynolds tensor components in the outer region of the asymptotic boundary layer with suction have the form

$$-\frac{\langle u'v'\rangle}{v_w^2} = g(\eta) + O(\mathrm{R}_w^{-1}),$$

$$\begin{aligned}\frac{\langle u'^2\rangle}{v_w^2} &= [\eta g'(\eta)]^2 S_1(\infty, 0, \eta) + O(\mathrm{R}_w^{-1}),\\ \frac{\langle v'^2\rangle}{v_w^2} &= [\eta g'(\eta)]^2 S_2(\infty, 0, \eta) + O(\mathrm{R}_w^{-1}),\end{aligned} \tag{3.7}$$

$$\frac{\langle w'^2\rangle}{v_w^2} = [\eta g'(\eta)]^2 S_3(\infty, 0, \eta) + O(\mathrm{R}_w^{-1}).$$

Thus, Reynolds stress profiles for two flows are also related to each other. Using Eq. (2.7) and the asymptotic form of the function $g$, we obtain the expressions

$$\begin{aligned}\frac{\sqrt[3]{\langle u'^2\rangle}}{(-v_w)^{2/3}} &= -\left(\frac{A_1}{4\kappa^2}\right)^{1/3}\ln\eta + O(1),\\ \frac{\sqrt{\langle v'^2\rangle}}{-v_w} &= -\frac{1}{2\kappa\sigma_2}\ln\eta + O(1),\\ \frac{\sqrt[3]{\langle w'^2\rangle}}{(-v_w)^{2/3}} &= -\left(\frac{A_3}{4\kappa^2}\right)^{1/3}\ln\eta + O(1), \quad \eta \to 0\end{aligned} \tag{3.8}$$

for rms velocity pulsations.

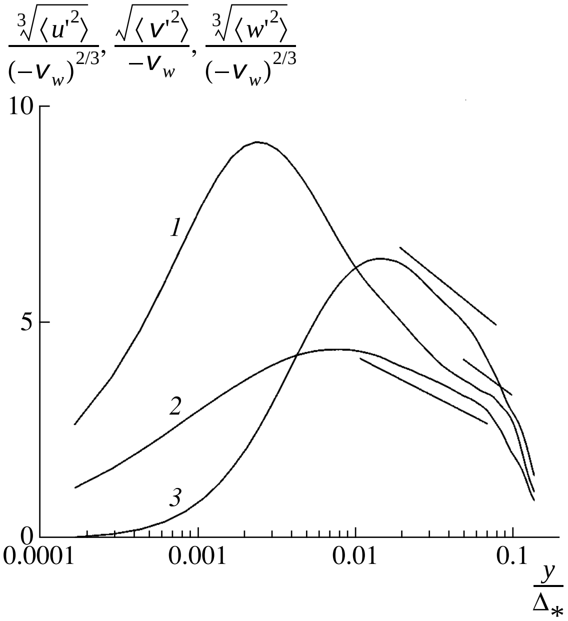

**Fig. 2.** Profiles of the rms pulsations of (*1*) $u'$, (*2*) $v'$, and (*3*) $w'$ in the asymptotic boundary layer with suction according to the data taken from [8, 9].

Figure 2 shows the profiles of rms velocity pulsations in the asymptotic boundary layer with suction according to the data taken from [8, 9]. For comparison, segments with slopes corresponding to the right-hand sides of asymptotic functions (3.8), where all constants are taken from the data for the impermeable plate are also shown. As is seen in Fig. 2, at least lines *2* and *3* corresponding to pulsations along the $y$ and $z$ axes have pronounced logarithmic sections.

## ACKNOWLEDGMENTS

This work was supported by the Council of the President of the Russian Federation for Support of Young Russian Scientists and Leading Scientific Schools (project no. NSh-1635.2003.1).

## REFERENCES

1. B. A. Kader and A. M. Yaglom, Itogi Nauki Tekh., Ser.: Mekh. Zhidk. Gaza **15**, 81 (1980).
2. I. I. Vigdorovich, Izv. Ross. Akad. Nauk, Mekh. Zhidk. Gaza, No. 4, 106 (1993).
3. A. A. Townsend, *The Structure of Turbulent Shear Flow* (Cambridge Univ. Press, Cambridge, 1976).
4. A. E. Perry, S. Henbest, and M. S. Chong, J. Fluid Mech. **165**, 163 (1986).
5. P. R. Spalart, J. Fluid Mech. **187**, 61 (1988).
6. D. Coles, J. Fluid Mech. **1**, Part 2, 191 (1956).
7. I. I. Vigdorovich, Izv. Ross. Akad. Nauk, Mekh. Zhidk. Gaza, No. 3, 61 (1999).
8. P. Mariani, P. Spalart, and W. Kollmann, in *Proceedings of the International Conference on Near-Wall Turbulent Flows, Tempe, 1993* (Elsevier, Amsterdam, 1993), pp. 347–356.
9. R. A. Antonia, P. R. Spalart, and P. Mariani, Phys. Fluids **6**, 430 (1994).

*Translated by R. Tyapaev*

*Doklady Physics, Vol. 49, No. 5, 2004, pp. 308–310. Translated from Doklady Akademii Nauk, Vol. 396, No. 1, 2004, pp. 52–55.*
*Original Russian Text Copyright © 2004 by Zubov.*

**MECHANICS**

# Continuously Distributed Dislocations and Disclinations in Nonlinearly Elastic Micropolar Media

**L. M. Zubov**

Presented by Academician V.A. Babeshko December 18, 2003

Received January 9, 2004

A nonlinear theory is proposed for dislocations and disclinations distributed with a certain density in an elastic medium with internal rotational degrees of freedom and couple stresses. A mathematical model of moment (micropolar) media can be used to describe the deformations of structurally inhomogeneous bodies [1], liquid crystals, and composite and magnetic materials. The resolving equations of the continual theory of defects are obtained by the limiting transition from the discrete set of isolated dislocations and disclinations to their continuous distribution. The general theory is illustrated by solving a problem of natural stresses induced in an elastic disc by a given distribution of wedge disclinations. Continuously distributed disclinations were previously considered in the model of a simple nonlinearly elastic medium disregarding the microstructure of a material [2]. The nonlinear theory of isolated dislocations and disclinations in micropolar media was given in [3].

**1.** According to [3, 4], the system of equations of the nonlinear statics of a micropolar elastic medium, which is also called the Cosserat continuum, in the absence of mass forces and moments consists of the equations of equilibrium for stresses

$$\operatorname{div}(\mathbf{P}\cdot\mathbf{H}) = 0, \quad \operatorname{div}(\mathbf{K}\cdot\mathbf{H}) + (\mathbf{C}^T\cdot\mathbf{P}\cdot\mathbf{H})_\times = 0, \quad (1)$$

the equations of state

$$\mathbf{P} = \frac{\partial W}{\partial \mathbf{Y}}, \quad \mathbf{K} = \frac{\partial W}{\partial \mathbf{L}}, \quad W = W(\mathbf{Y}, \mathbf{L}), \qquad (2)$$

and the geometric relations

$$\mathbf{Y} = \mathbf{C}\cdot\mathbf{H}^T, \quad \mathbf{C} = \operatorname{grad}\mathbf{R}, \quad \mathbf{R} = X_k\mathbf{i}_k, \qquad (3)$$

$$\mathbf{L}\times\mathbf{E} = -(\operatorname{grad}\mathbf{H})\cdot\mathbf{H}^T. \qquad (4)$$

Here, **P** and **K** are the stress tensor and couple stress tensor, respectively, both of the Kirchhoff type; **C** is the strain gradient (distortion tensor); **H** is the properly orthogonal tensor field of microrotations characterizing the rotational degrees of freedom of Cosserat-continuum particles; $W$ is the specific free energy of the medium; **Y** is the deformation measure; **L** is the bending strain tensor; **E** is the identity tensor; $X_k$, $k = 1, 2, 3$, are the Cartesian coordinates of the particles of the deformed body (Eulerian coordinates); $\mathbf{i}_k$ are the coordinate unit vectors; div and grad are the divergence and gradient operators, respectively, in the reference configuration of the material body (i.e., in the Lagrangian coordinates); and $\mathbf{A}_\times$ means the vector invariant of the second-rank tensor **A**. The Cartesian $x_s$ or curvilinear $q^s$, $s = 1, 2, 3$, coordinates of the reference configuration of the elastic body may be used as the Lagrangian coordinates.

To introduce the density of dislocations in a micropolar medium, let us consider the problem of determining the field of displacements in the medium $\mathbf{u} = (X_k - x_k)\mathbf{i}_k$ by using the tensor fields of deformation measure $\mathbf{Y}(q^s)$ and microrotations $\mathbf{H}(q^s)$ that are assumed to be continuously differentiable and single-valued in the multiply connected domain $\sigma$. Taking into account that $\operatorname{grad}\mathbf{u} = \mathbf{Y}\cdot\mathbf{H} - \mathbf{E}$ and following [2], we arrive at the expression

$$\mathbf{b}_N = \oint_{\gamma_N} \mathbf{i}_k\cdot\mathbf{Y}\cdot\mathbf{H}\,dx_k \qquad (5)$$

for the Burgers vectors of dislocations that are responsible for the lack of uniqueness of the displacement field in the multiply connected domain. Here, $\gamma_N$ is a simple closed contour enveloping the line of only the $N$th dislocation. Taking Eq. (5) into account, we apply the method proposed in [2] to move from the discrete set of translational defects, or dislocations, to their continuous distribution. Using the known definition of the density of dislocations as the tensor $\mathbf{d}_0$ [5] whose flux through any surface is equal to the total Burgers vector of dislocations crossing this surface, we arrive at the equation

$$\operatorname{curl}(\mathbf{Y}\cdot\mathbf{H}) = \mathbf{d}_0, \qquad (6)$$

where curl is the curl operator in the Lagrangian coordinates. For a given dislocation density tensor $\mathbf{d}_0$,

---

*Rostov State University,*
*pr. Stachki 194, Rostov-on-Don, 344104 Russia*
*e-mail: zubov@math.rsu.ru*

which must satisfy the condition $\mathrm{div}\mathbf{d}_0 = 0$, Eqs. (1), (2), (4), and (6) form a complete system of equations with unknowns $\mathbf{Y}$ and $\mathbf{H}$.

**2.** Under certain assumptions about the dislocation density, the system of Eqs. (1), (2), (4), and (6) can be transformed by excluding the microrotation tensor $\mathbf{H}$ from the unknown functions and taking the tensor fields $\mathbf{Y}$ and $\mathbf{L}$ as unknowns. Multiplying Eqs. (1) and (6) by the $\mathbf{H}^T$ tensor from the right and taking representation (4) into account, we obtain the system of equations

$$\begin{aligned} &\mathrm{div}\mathbf{P} - (\mathbf{P}^T \cdot \mathbf{L})_\times = 0, \\ &\mathrm{div}\mathbf{K} - (\mathbf{K}^T \cdot \mathbf{L} + \mathbf{P}^T \cdot \mathbf{Y})_\times = 0, \end{aligned} \tag{7}$$

$$\mathrm{curl}\mathbf{Y} + \mathbf{Y} \times\times \mathbf{L} = \mathbf{d}, \quad \mathbf{d} \equiv \mathbf{d}_0 \cdot \mathbf{H}^T. \tag{8}$$

Here, the invariant fiber bundle of second-rank tensors is defined in terms of the vector products of the basis vectors $\mathbf{r}_s$ as follows:

$$\begin{aligned} \mathbf{Y} \times\times \mathbf{L} &= (Y^{mn}\mathbf{r}_m \otimes \mathbf{r}_n) \times\times (L^{ks}\mathbf{r}_k \otimes \mathbf{r}_s) \\ &= Y^{mn}L^{ks}(\mathbf{r}_m \times \mathbf{r}_k) \otimes (\mathbf{r}_n \times \mathbf{r}_s). \end{aligned}$$

Below, the modified dislocation density tensor $\mathbf{d}$ will be treated as given.

The microrotation tensor must also be excluded from relation (4), specifying the bending strain tensor of the micropolar medium. To this end, we consider the problem of determining the microrotation tensor field $\mathbf{H}$ in the micropolar medium with continuously distributed dislocations in terms of a given bending strain tensor field $\mathbf{L}$. We now remove the requirement of the uniqueness of the tensor field $\mathbf{H}$ in the multiply connected domain $\sigma$ and use the condition of uniqueness and differentiability of the tensor $\mathbf{L}$ in this domain. Using Eq. (4), we compose the following system of equations for the tensor $\mathbf{H}$:

$$\frac{\partial \mathbf{H}}{\partial q^s} = -\mathbf{L}_s \times \mathbf{H}, \quad \mathbf{L}_s = \mathbf{r}_s \cdot \mathbf{L}, \quad \mathbf{r}_s = \frac{\partial x_k}{\partial q^s}\mathbf{i}_k. \tag{9}$$

Excluding the unknown orthogonal tensor $\mathbf{H}$ from system (9), we arrive at the tensor solvability condition

$$\mathrm{curl}\mathbf{L} + \frac{1}{2}\mathbf{L} \times\times \mathbf{L} = 0. \tag{10}$$

This condition is a necessary and sufficient condition for the existence of the unique microrotation field in the simply connected domain $\sigma$ when the tensor $\mathbf{H}$ is given in a certain point of the domain. If the $\sigma$ domain is multiply connected, the solution of the Cauchy problem for system (9) is generally multivalued. The possible multivaluedness of the solution is removed after the transformation of the multiply connected domain to simply connected one by introducing the necessary number of cuts $\tau_M$, $M = 1, 2, \ldots$. The microrotation tensor takes different values $\mathbf{H}_+$ and $\mathbf{H}_-$ at the different edges of the cut. The relation $\mathbf{H}_+ = \mathbf{H}_- \cdot \Phi_M$, where $\Phi_M$ is the properly orthogonal tensor that is constant for a given cut $\tau_M$, is proved by using the continuity and uniqueness of the bending strain tensor $\mathbf{L}$ in the $\sigma$ domain and applying the method proposed in [3]. The existence of the above jump of the microrotation tensor at the cut $\tau_M$ means the existence of isolated rotational defects, or disclinations, in an elastic micropolar body with distributed dislocations. As well as in the Cosserat continuum without dislocations [3], the Frank vector of each isolated disclination is expressed in terms of the bending strain tensor field through the multiplicative contour integral. These integral relations, together with Eqs. (7), (8), and (10) and the boundary conditions on the body surface, provide the formulation of the boundary value problem concerning the equilibrium of the micropolar medium with continuously distributed dislocations and isolated disclinations.

Since the properties of multiplicative line integrals are complicated [3], the limiting transition from a discrete set of isolated disclinations to their continuous distribution is generally impossible. Nevertheless, as will be shown below, this transition is possible in the plane problem for the micropolar elastic medium.

**3.** We consider plane deformation in the $(x_1, x_2)$ plane. In this case, the dislocation density tensor has the form $\mathbf{d}_0 = \mathbf{i}_3 \otimes \mathbf{a}_0$ $(\mathbf{a}_0 \cdot \mathbf{i}_3 = 0)$ [2], where $\mathbf{a}_0$ is the edge dislocation density vector, and the distortion tensor $\mathbf{C}$ satisfies the incompatibility equation

$$\begin{aligned} &\nabla \cdot (\mathbf{e} \cdot \mathbf{C}) = \mathbf{a}_0, \quad \mathbf{e} = -\mathbf{i}_3 \times \mathbf{E}, \\ &\nabla = \mathbf{i}_1\frac{\partial}{\partial x_1} + \mathbf{i}_2\frac{\partial}{\partial x_2}. \end{aligned} \tag{11}$$

Here, $\nabla$ is the two-dimensional gradient operator and $\mathbf{e}$ is the discriminant tensor. The $\mathbf{H}$ tensor for plane deformation is expressed in terms of the angle $\chi$ of microrotation about the $x_3$ axis through the formula

$$\mathbf{H} = \mathbf{g}\cos\chi + \mathbf{e}\sin\chi + \mathbf{i}_3 \otimes \mathbf{i}_3, \quad \mathbf{g} = \mathbf{E} - \mathbf{i}_3 \otimes \mathbf{i}_3. \tag{12}$$

Using Eqs. (4) and (12), we obtain

$$\mathbf{L} = \mathbf{l} \otimes \mathbf{i}_3, \quad \mathbf{l} = \nabla\chi. \tag{13}$$

In view of Eqs. (3) and (12), Eq. (11) is transformed as

$$\nabla \cdot (\mathbf{e} \cdot \mathbf{Y} \cdot \mathbf{g}) + \mathbf{l} \cdot (\mathbf{e} \cdot \mathbf{Y} \cdot \mathbf{e}) = \mathbf{a}, \tag{14}$$

where $\mathbf{a} = \mathbf{a}_0 \cdot \mathbf{H}^T$.

According to Eq. (13), the microrotation field is determined in terms of the bending strain field through the quadratures

$$\chi = \int_{\mathbf{r}_0}^{\mathbf{r}} \mathbf{l} \cdot d\mathbf{r} + \chi(\mathbf{r}_0), \quad \mathbf{r} = x_1\mathbf{i}_1 + x_2\mathbf{i}_2. \tag{15}$$

When the condition $\nabla \cdot \mathbf{e} \cdot \mathbf{l} = 0$ is valid, the line integral in Eq. (15) is independent of the integration path if the $\sigma$ domain is simply connected. For the multiply connected plane domain homeomorphic to the circle with circle holes, expression (15) generally specifies a multivalued function. Transforming the multiply connected domain to the simply connected one by means of cuts, we find that the values $\chi_\pm$ at the opposite edges of each cut may differ by a constant:

$$\chi_+ - \chi_- = \theta_S, \quad S = 1, 2, \ldots .$$

Constants $\theta_S$ are independent of the choice of the system of cuts and are expressed in terms of the bending strain field through an ordinary (not multiplicative) contour integral. The existence of nonzero constants $\theta_S$ means that isolated wedge disclinations exist in a multiply connected micropolar body. Using the method described in [2] for the transformation of a discrete set of disclinations to their continuous distribution, we arrive at the following incompatibility equation for bending strains of the plane medium:

$$\nabla \cdot \mathbf{e} \cdot \mathbf{l} = \beta, \tag{16}$$

where $\beta$ is the scalar density of edges disclinations. For the plane case, equilibrium equations (7) take the form

$$\nabla \cdot \mathbf{P} + \mathbf{l} \cdot \mathbf{P} \cdot \mathbf{e} = 0, \quad \nabla \cdot \mathbf{K} \cdot \mathbf{i}_3 = \mathrm{tr}(\mathbf{P} \cdot \mathbf{e} \cdot \mathbf{Y}^T \cdot \mathbf{g}) \tag{17}$$

and, together with incompatibility equations (14) and (16), form the complete system of nonlinear equations determining the natural stresses in the plane medium with distributed dislocations and disclinations.

**4.** We illustrate the above theory by solving the problem of determining natural stresses induced in an elastic disc by the axisymmetrically distributed edges disclinations. Let us use the model of the physically linear micropolar medium [3]

$$\begin{gathered} 2W = \lambda \mathrm{tr}^2\mathbf{U} + (\mu + \psi)\mathrm{tr}(\mathbf{U} \cdot \mathbf{U}^T) + (\mu - \psi)\mathrm{tr}\mathbf{U}^2 \\ + \delta \mathrm{tr}^2\mathbf{L} + (\gamma + \eta)\mathrm{tr}(\mathbf{L} \cdot \mathbf{L}^T) + (\gamma - \eta)\mathrm{tr}\mathbf{L}^2, \\ \mathbf{U} = \mathbf{Y} - \mathbf{E}, \end{gathered} \tag{18}$$

where $\lambda$, $\mu$, $\delta$, $\gamma$, $\psi$, and $\eta$ are Young's moduli. Let $\mathbf{a} = 0$ and $\beta = \beta(r)$. We seek the strain field in the form

$$\begin{gathered} \mathbf{Y} = Y_1(r)\mathbf{e}_r \otimes \mathbf{e}_r + \frac{h(r)}{r}\mathbf{e}_\varphi \otimes \mathbf{e}_\varphi + \mathbf{i}_3 \otimes \mathbf{i}_3, \\ \mathbf{l} = l_1(r)\mathbf{e}_r + l_2(r)\mathbf{e}_\varphi, \end{gathered} \tag{19}$$

$$\mathbf{e}_r = \mathbf{i}_1 \cos\varphi + \mathbf{i}_2 \sin\varphi, \quad \mathbf{e}_\varphi = -\mathbf{i}_1 \sin\varphi + \mathbf{i}_2 \cos\varphi,$$

where the polar coordinates $r$ and $\varphi$ on the disc plane vary in the intervals $r_1 \le r \le r_2$ and $0 \le \varphi \le 2\pi$. In view of Eqs. (2), (18), and (19), the system of Eqs. (14), (16), and (17) is reduced to the equation

$$h'' - \frac{g'}{g}h' - g^2 h = \frac{(1 - rg)g}{1 - \nu}, \tag{20}$$

$$\nu = \frac{\lambda}{2(\lambda + \mu)}, \quad rg(r) = \int_{r_1}^{r} \beta(\rho)\rho d\rho + 1.$$

The strain components and couple stresses are expressed in terms of the functions $h(r)$ and $g(r)$ as

$$\begin{gathered} Y_1 = \frac{h'(r)}{rg(r)}, \quad l_1 = 0, \quad l_2 = g(r) - \frac{1}{r}, \\ \mathbf{K} = [g(r) - r^{-1}][(\gamma + \eta)\mathbf{e}_\varphi \otimes \mathbf{i}_3 + (\gamma - \eta)\mathbf{i}_3 \otimes \mathbf{e}_\varphi]. \end{gathered} \tag{21}$$

Equation (20) has the general solution

$$h(r) = C_1 e^{t(r)} + C_2 e^{-t(r)} + \frac{1}{1 - \nu}\left[r - e^{-t(r)}\int e^{t(r)} dr\right],$$

$$t(r) = \int g(r) dr.$$

The constants $C_1$ and $C_2$ are found from the condition that the disc edges $r = r_1$ and $r_2$ are unloaded.

## ACKNOWLEDGMENTS

This work was supported by the Competition Center of Fundamental Natural Sciences, St. Petersburg State University (project no. E 02-4.0-91).

## REFERENCES

1. V. E. Panin, V. A. Likhachev, and Yu. V. Grinyaev, *Structural Levels of Deformation of Solids* (Nauka, Novosibirsk, 1985).
2. S. V. Derezin and L. M. Zubov, Dokl. Akad. Nauk **366**, 762 (1999) [Dokl. Phys. **44**, 391 (1999)].
3. L. M. Zubov, *Nonlinear Theory of Dislocations and Disclinations in Elastic Bodies* (Springer, Berlin, 1997).
4. E. Nikitin and L. M. Zubov, J. Elast. **51** (1), 1 (1998).
5. A. A. Vakulenko, Itogi Nauki Tekh., Ser.: Mekh. Deform. Tverd. Tela **22**, 3 (1991).

*Translated by R. Tyapaev*

*Doklady Physics, Vol. 49, No. 5, 2004, pp. 311–314. Translated from Doklady Akademii Nauk, Vol. 396, No. 1, 2004, pp. 56–59.*
*Original Russian Text Copyright © 2004 by Mukhamediev, Galybin.*

**MECHANICS**

# Solution of a Plane Elastic Problem with Given Trajectories of the Principal Stresses

**Sh. A. Mukhamediev* and A. N. Galybin****

Presented by Academician S.S. Grigoryan November 4, 2003

Received November 6, 2003

The problem of determining a plane stress-tensor field (**T** field) with given principal stress trajectories (PSTs) was originated in photoelasticity as early as the beginning of the twentieth century [1]. Principal stress trajectories are curves the tangents to which are directed along one of the directions of the two principal stresses $T_1$ and $T_2$. In a loaded transparent plane model, $T_1$–$T_2$ contour lines, as well as isoclinics (curves along which $T_1$ and $T_2$ preserve their directions), are directly observed. An orthogonal curvilinear net of PSTs is graphically drawn from the pattern of isoclinics [1]. Despite the assumption that the model is elastic, an incomplete set of governing equations of the theory of elasticity is traditionally used in photoelasticity. Thus, the **T** field is determined by integrating the equations of equilibrium (or one of them) with the inclusion of information about $T_1$–$T_2$ and boundary stresses [1], i.e., by solving a boundary value problem.

The problem of determining the **T** field from the principal stress directions has recently become very important in geodynamics. Observations indicate that two of the three principal stresses are subhorizontal [2]. When the spatial density of discrete data on the principal stress directions is sufficient, a plane horizontal pattern of PSTs can be accurately constructed by a number of known methods [3]. Therefore, the problem of determining the **T** field in stable blocks of the lithosphere (considered as elastic plates) is similar to that in photoelasticity. However, the method used in photoelasticity is inapplicable to geodynamics due to the absence of both $T_1$–$T_2$ data and, more importantly, reliable boundary conditions: different model estimates of plate-driving forces differ from each other by the order of their magnitudes.

This paper presents a method for determining the **T** field in a homogeneous isotropic elastic domain by using only the pattern of PSTs without information on the boundary conditions and $T_1$–$T_2$ value. The symmetric stress tensor **T** in a plane can be represented in terms of real $P$ and complex $D$ functions as

$$P = \frac{1}{2}(T_1 + T_2), \quad D = |D|e^{i\alpha},$$
$$|D| = \tau_{\max} = \frac{1}{2}|T_2 - T_1|. \tag{1}$$

Here, the absolute value $|D|$ of the stress deviator $D$ is the maximum shear stress in the plane and its argument $\alpha$ is expressed in the form

$$\alpha = \arg D = -2\varphi, \tag{2}$$

where the angle $\varphi$ (which specifies the principal direction) is measured counterclockwise from the positive $x$ semiaxis of the Cartesian $xy$ plane to the direction of the minor principal stress. The determination of the **T** field is equivalent to the determination of the real functions $P(z, \bar{z})$, $\tau_{\max}(z, \bar{z})$, $\alpha(z, \bar{z})$, where $z = x + iy$, $\bar{z} = x - iy$. The function $\alpha$ is known for a given PST field. In this case, the problem is reduced to the determination of bounded functions $P$ and $\tau_{\max}$ in the closed (generally, multiply connected) domain $\Omega$ under study. It is assumed that the function $\alpha(z, \bar{z})$ is twice differentiable everywhere in $\Omega$ except possibly the singular points of the PST field, where $\tau_{\max} = 0$, the argument $\alpha$ is undefined, and the curvature of stress trajectories is infinite [1, 4].

When in-plane body forces are absent in a homogeneous isotropic elastic medium, the complete set of governing equations of plane elasticity has the form

$$\frac{\partial P}{\partial z} = \frac{\partial D}{\partial \bar{z}}, \quad \Delta P = 0, \tag{3}$$

where $\Delta = 4\frac{\partial^2}{\partial z \partial \bar{z}}$ is the Laplacian. Here, the first equation represents two scalar equations of equilibrium and

---

* *Gamburtsev Institute of Physics of the Earth,*
*Russian Academy of Sciences,*
*ul. Bol'shaya Gruzinskaya 10, Moscow, 123995 Russia*
*e-mail: shamil@ifz.ru*

** *University of Western Australia,*
*35 Stirling Highway, Crawley, WA 6009, Australia*
*e-mail: galybin@cyllene.uwa.edu.au*

1028-3358/04/4905-0311$26.00 © 2004 MAIK “Nauka/Interperiodica”

the second one follows from elastic relationships. The general solution of set (3) is expressed in the form [5]

$$P(z, \bar z) = \Phi(z) + \overline{\Phi(z)}, \quad D(z, \bar z) = \bar z\Phi'(z) + \Psi(z), \quad (4)$$

where the potentials $\Phi$ and $\Psi$ are holomorphic functions, while $D$ is a biholomorphic function. A real biholomorphic function $D = D_{\text{real}}$ can be represented in the general form

$$D_{\text{real}}(z, \bar z) = c_2\bar z z + \overline{c_1 z} + c_1 z + c_0, \qquad (5)$$
$$\operatorname{Im} c_0 = \operatorname{Im} c_2 = 0,$$

containing four arbitrary real constants $c_0$, $c_{11} = \operatorname{Re} c_1$, $c_{12} = \operatorname{Im} c_1$; and $c_2$.

If an arbitrary function $\alpha(z, \bar z)$ is given in the domain $\Omega$, then, in general, the functions $P(z, \bar z)$ and $\tau_{\max}(z, \bar z)$ cannot simultaneously satisfy all three scalar equations (3). Therefore, an arbitrary PST field cannot be realized in an elastic domain. For instance, the function $\alpha = \alpha_0 + (z\bar z - 1)^2$, $\alpha_0 = \text{const}$, is not admissible in plane elasticity. In view of Eqs. (1) and (4), the PST field is admissible if and only if $\alpha(z, \bar z)$ is the argument of a biholomorphic function $D_1$, i.e., if the following representation is valid

$$e^{i\alpha} = \frac{D_1(z, \bar z)}{|D_1(z, \bar z)|} \quad \text{or} \quad \alpha(z, \bar z) = \frac{1}{2i}\ln\frac{D_1(z, \bar z)}{\overline{D_1(z, \bar z)}}, \qquad (6)$$

where $D_1(z, \bar z) = \bar z\Phi_1'(z) + \Psi_1(z)$ and $\Phi_1'(z)$, $\Psi_1(z)$ are holomorphic functions in the domain $\Omega$.

The verification of admissibility of a prescribed PST field is the first step in the determination of the **T** field in an elastic medium. This can be achieved by a number of methods. In particular, if the function $\alpha(z, \bar z)$ is harmonic ($\Delta\alpha = 0$) and represents the argument of a holomorphic function $A(z)$, then the verified PST field is admissible, because $\arg A$ is simultaneously the argument of a biholomorphic function $D = D_{\text{real}}(z, \bar z)A(z)$ ($D_{\text{real}} > 0$). In the general case, the admissibility of the PST field can be examined by representing a given biholomorphic function $D_1 = \bar z\Phi_1'(z) + \Psi_1(z)$ in terms of its argument $\alpha$. Let us find the desired representation on the disk $\mathfrak{R}$: $|z| < R = \text{const}$ that does not contain singular points. In this case, $|\Psi_1(0)| \neq 0$. Two possible cases are considered below.

**1.** $|\Phi_1'(0)| = 0$. In this case, $D_1 = \bar z zX(z) + \Psi_1(z)$, where $X(z)$ is a known holomorphic function. Let the holomorphic function $V(r_*; z) = r_*^2X(z) + \Psi_1(z)$ (which depends on the parameter $r_*$, $0 \le r_* < R$) be introduced in the domain $\mathfrak{R}$. This function coincides with $D_1$ on the circle $\gamma_*$: $|z| = r_*$ and is expressed in the subdomain $\mathfrak{R}_*$: $|z| < r_*$ as

$$V(r_*; z) = \left|r_*^2X(0) + \Psi_1(0)\right|\exp(i\mathbf{S}(r_*; \alpha)), \qquad (7)$$

$$\mathbf{S}(r_*; \alpha) = \frac{1}{2\pi i}\int\limits_{\gamma_*}\frac{2\alpha(\xi)}{\xi - z}d\xi - \frac{1}{2\pi i}\int\limits_{\gamma_*}\frac{\alpha(\xi)}{\xi}d\xi, \qquad (8)$$
$$\xi \in \gamma_*,$$

where $\mathbf{S}(r_*; \alpha)$ is the Schwarz operator that is defined in the domain $\mathfrak{R}_*$ and applied to the function $\alpha$ defined on the contour $\gamma_*$ [6]. Since the parameter $r_*$ is arbitrary, the function $D_1$ in the domain $\mathfrak{R}$ can be represented in terms of the function $V(r_*; z)$ [and, therefore, in terms of $\alpha = \arg(D_1)$] as follows:

$$D_1(z, \bar z) = V(r_*; z) - (z\bar z - r_*^2)\frac{1}{2r_*}\frac{dV(r_*; z)}{dr_*}. \qquad (9)$$

**2.** $|\Phi_1'(0)| \neq 0$. In this case, the function $r_*^2z^{-1}\Phi_1'(z) + \Psi_1(z)$ has a root in the domain $\mathfrak{R}_*$ at a point $z = b(r_*)$ ($0 < |b| < r_*$), which is found from the equation $b = -\frac{r_*^2\Phi_1'(b)}{\Psi_1(b)}$. Meanwhile, the function

$$V(r_*; z) = (z - b(r_*))^{-1}(r_*^2\Phi_1'(z) + z\Psi_1(z))$$

is holomorphic and has no zeros in the domain $\mathfrak{R}_*$. This function coincides with the function $\frac{zD_1}{z - b(r_*)}$ on the contour $\gamma_*$: $|z| = r_*$ and is expressed in the domain $\mathfrak{R}_*$ in terms of the argument $\alpha$ as

$$V(r_*; z) = |\Phi_1'(0)|\frac{r_*^2 - z\overline{b(r_*)}}{|b(r_*)|r_*^2}\exp(i\mathbf{S}(r_*; \alpha)). \qquad (10)$$

The desired representation for the function $D_1$ in the domain $\mathfrak{R}$ can be written as

$$D_1(z, \bar z) = \frac{z - b(r_*)}{z}V(r_*; z)$$
$$- \frac{r_*^2 - \bar z z}{2r_*z}\frac{d}{dr_*}((z - b(r_*))V(r_*; z)). \qquad (11)$$

It is readily seen that the substitution of the function $\alpha(z, \bar z)$ from Eq. (6) into Eqs. (7) and (9) (for $|\Phi_1'(0)| = 0$) or into Eqs. (10) and (11) (for $|\Phi_1'(0)| \neq 0$) turns Eqs. (9) and (11) into identities. However, if $\alpha(z, \bar z)$ is not representable in the form of Eq. (6), then the parameter $r_*$ remains in Eqs. (9) and (11) regardless of the choice of the constants $X(0)$ and $\Psi_1(0)$ in Eq. (7) and both the constant $\Phi_1'(0)$ and function $b(r_*)$ in Eq. (10).

If it is impossible to exclude the parameter $r_*$ from Eqs. (9) and (11), the given PST field is not permitted for the elastic medium in accordance with this verification method.

If a PST field is admissible, then the above methods and their generalization allow the determination of the stress deviator function

$$D_1(z, \bar{z}) = \bar{z}\Phi_1'(z) + \Psi_1(z).$$

However, this function should be considered only as a particular solution of the problem, because, e.g., the function $c_3 D_1(z, \bar{z})$ ($c_3 > 0$ is an arbitrary real constant) is also a solution. The problem is reduced to the determination of the general form of the biholomorphic function $D = \bar{z}\Phi'(z) + \Psi'(z)$ that is regular in $\Omega$ and has the same argument field $\alpha(z, \bar{z})$ as the function $D_1$.

The transformation $D_1(z, \bar{z}) \to D(z, \bar{z})$ that preserves the argument has the general form

$$D(z, \bar{z}) = M(z, \bar{z}) D_1(z, \bar{z}), \quad \operatorname{Im} M(z, \bar{z}) = 0, \quad M(z, \bar{z}) > 0. \tag{12}$$

The following two alternative cases **A** and **B** are possible.

**A.** The argument of the function $D_1(z, \bar{z})$ is a harmonic function [$\Delta\alpha(z, \bar{z}) = 0$ in $\Omega$]. Therefore, it is easy to find a holomorphic function $A(z)$ with the given argument $\alpha$ and associate it with the function $D_1$. Since the function $M(z, \bar{z})$ in Eq. (12) satisfies the condition $\frac{\partial^2 M}{\partial \bar{z}^2} = 0$ in this case, it is a real biholomorphic function $D_{\text{real}}$ [see Eq. (5)], and, in view of Eqs. (3), the general solution of the problem is expressed in the form

$$\begin{aligned} D(z, \bar{z}) &= (c_2 \bar{z} z + \overline{c_1 z} + c_1 z + c_0) A(z), \\ P(z, \bar{z}) &= 2\operatorname{Re}\int (c_2 z + \bar{c}_1) A(z) dz + c, \\ \arg A(z) &= \alpha. \end{aligned} \tag{13}$$

Solution (13) depends on five arbitrary real constants: four constants $c_0$, $\operatorname{Re} c_1$, $\operatorname{Im} c_1$ and $c_2$ that must provide the condition $D_{\text{real}} > 0$ and the constant $c$ appearing due to the integration of $\Phi'(z)$. It should be noted that the solution obtained above remains valid when the function $a_2 z\bar{z} + \overline{a_1 z} + a_1 z + a_0)A(z)$ is taken as $D_1$, where real constants $a_0$, $\operatorname{Re} a_1$, $\operatorname{Im} a_1$, and $a_2$ are prescribed. In particular, the cases $\Phi_1'(z) \equiv 0$ and $\Psi_1(z) \equiv 0$ are included in general solution (13).

**B.** The argument $\alpha(z, \bar{z})$ of the function $D_1(z, \bar{z})$ is a nonharmonic function [$\Delta\alpha(z, \bar{z}) \neq 0$] and, therefore, neither $\Phi_1'(z)$ nor $\Psi_1(z)$ is identically zero. Let $\Phi_1'(z) \neq 0$ within the circle

$$\gamma\colon (z - e)(\bar{z} - \bar{e}) = R^2, \tag{14}$$

with the center at the point $z = e \in \Omega$. Let the disk $\Re$: $|z - e| < R$ belong entirely to the investigated domain $\Omega$ ($\Re \subset \Omega$). Then, by substituting the variable $\bar{z}$ expressed in terms of $z$ according to Eq. (14) into the expressions for the desired ($D$) and known ($D_1$) functions, one can readily see that the function $M(z, \bar{z})$ [see Eq. (12)] on the circle $\gamma$ is the boundary value of the function $B(z)$

$$B(z) = \frac{(R^2 + \bar{e}(z - e))\Phi'(z) + (z - e)\Psi(z)}{(R^2 + \bar{e}(z - e))\Phi_1'(z) + (z - e)\Psi_1(z)}. \tag{15}$$

Owing to the inequality $\Phi_1'(e) \neq 0$, the radius $R$ can be chosen such that the denominator in Eq. (15) is not equal to zero on the disk $\Re$. Then, $B(z)$ is holomorphic on the disk $\Re$. Since $\operatorname{Im} B(z) = 0$ on $\gamma$, $B(z)$ is an arbitrary real constant, e.g., $c_3$. In view of this circumstance, from Eq. (15) one obtains the following relation on the disk $\Re$:

$$\Psi(z) = \left(\frac{R^2}{z - e} + \bar{e}\right)(c_3\Phi_1'(z) - \Phi'(z)) + c_3\Psi_1(z). \tag{16}$$

The substitution of Eq. (16) into Eq. (12) followed by simple transformations results in the relationship

$$\frac{M(z, \bar{z}) - c_3}{R^2 - (z - e)(\bar{z} - \bar{e})} = \frac{C(z)}{D_1(z, \bar{z})}, \quad C(z) = \frac{c_3\Phi_1'(z) - \Phi'(z)}{z - e}. \tag{17}$$

The left-hand side of Eq. (17) is real and, therefore, its argument is equal to 0 or $\pi$. At the same time, the argument of the right-hand side of Eq. (17) cannot be constant when $C(z) \neq 0$, because the argument of the function $C(z)$ is harmonic and the argument $\alpha$ of the function $D_1$ is nonharmonic by hypothesis. Equation (17) can be satisfied only if $C(z) = 0$, which results in $\Phi'(z) = c_3\Phi_1'(z)$ within $\Re$. In accordance with the uniqueness theorem, the latter equality is valid everywhere in the investigated domain $\Omega$. Thus, it follows from Eq. (16) that the equality $\Psi(z) = c_3\Psi_1(z)$ is also satisfied in $\Omega$. Hence, if argument $\alpha$ is nonharmonic, the ratio $M = \frac{D}{D_1}$

is an arbitrary constant $c_3$ in $\Omega$, and the general solution of the problem takes the form

$$
\begin{aligned}
D(z, \bar{z}) &= c_3(\bar{z}\Phi_1'(z) + \Psi_1(z)),\\
P(z, \bar{z}) &= c_3(\Phi_1(z) + \overline{\Phi_1(z)}) + c, \qquad (18)\\
\operatorname{Im} c_3 &= 0, \quad \operatorname{Re} c_3 > 0, \quad \operatorname{Im} c = 0.
\end{aligned}
$$

Let us consider simple examples of the determination of the **T** field when $\alpha(z, \bar{z})$ is harmonic and the function $\Psi_1(z)$ is substituted as the function $A(z)$ in Eq. (13).

**1.** Both PST families are represented by straight lines, and one of these families is inclined at angle $\varphi_0$ to the $x$ axis. Then, $\alpha = \alpha_0 = -\frac{\varphi_0}{2}$ and, according to Eq. (6), $\exp(i\alpha) = \exp(i\alpha_0) = \Psi_1(z)$. It follows from Eq. (13) that

$$
\begin{aligned}
D &= (c_2\bar{z}z + \overline{c_1 z} + c_1 z + c_0)e^{i\alpha_0},\\
P &= \operatorname{Re}(e^{i\alpha_0}(c_2 z^2 + 2\bar{c}_1 z)) + c, \qquad (19)\\
\operatorname{Im} c_0 &= \operatorname{Im} c_2 = \operatorname{Im} c = 0.
\end{aligned}
$$

Solution (19) that was obtained earlier in a different way in [7] was used in [8] for the determination of tectonic stresses in regions with homogeneous PSTs.

**2.** Principal stress trajectories coincide with the coordinate lines of polar coordinates $r$ and $\theta$. One of the PST families is represented by a set of rays inclined at angles $\varphi = \theta$. It follows from Eq. (2) that $\alpha = -2\theta$ and, therefore, $\exp(i\alpha) = \frac{|z^2|}{z^2}$. Then, $\Psi_1(z) = z^{-2}$ according to Eq. (6), and Eq. (13) leads to the general solution

$$
\begin{aligned}
D &= z^{-2}(c_2\bar{z}z + \overline{c_1 z} + c_1 z + c_0),\\
P &= c_2\ln(\bar{z}z) - \bar{c}_1 z^{-1} - c_1\bar{z}^{-1} + c, \qquad (20)\\
\operatorname{Im} c_0 &= \operatorname{Im} c_2 = \operatorname{Im} c = 0.
\end{aligned}
$$

Formulas (20) represent a bounded general solution of the problem in any simply connected domain not containing the origin. The Lamé solution for a circular ring under internal and external pressure [5] is obtained by setting $c_1 = c_2 = 0$ in Eq. (20).

**3.** Principal stress trajectories coincide with the coordinate lines of the parabolic coordinates $\xi$ and $\eta$ introduced by the relationships $z = \frac{\zeta^2}{2}$, where $\zeta = \xi + i\eta$. For trajectories $\eta$ = const, one has

$$
\begin{aligned}
\frac{dy}{dx} &= \tan\varphi = -\tan\left(\frac{1}{2}\alpha\right) = \frac{\eta}{\xi} = \tan(\arg\zeta)\\
&= \tan\left(\frac{1}{2}\theta\right) \to \alpha = -\theta \to e^{i\alpha} = \frac{|z|}{z}. \qquad (21)
\end{aligned}
$$

Since $\Psi_1(z) = z^{-1}$ in accordance with Eq. (6), the general solution is found from Eq. (13) as follows:

$$
\begin{aligned}
D &= z^{-1}(c_2\bar{z}z + \overline{c_1 z} + c_1 z + c_0),\\
P &= 2\operatorname{Re}(c_2 z + \bar{c}_1 \ln z) + c, \qquad (22)\\
\operatorname{Im} c_0 &= \operatorname{Im} c_2 = \operatorname{Im} c = 0.
\end{aligned}
$$

Formulas (22) present a general solution bounded in any domain not containing the origin. A bounded solution for a domain containing $z = 0$ can be obtained by setting $c_0 = c_1 = 0$ in Eqs. (22) and describes stresses near singular points of one particular kind where the curvature of PSTs is infinite [4].

In conclusion, we emphasize that, in contrast to the concept widely used in photoelasticity, the problem of determining the **T** field from the prescribed PST field is not a boundary value problem. If the slope $\varphi(z, \bar{z})$ of the PST to the $x$ axis is a harmonic function, the stress tensor field is expressed in terms of $\varphi(z, \bar{z})$ through the above formulas containing five arbitrary real constants. If $\varphi(z, \bar{z})$ is a nonharmonic function (but admissible in elasticity), the solution involves two such constants. In geodynamic applications, these constants can be determined from local *in situ* stress measurements.

## ACKNOWLEDGMENTS

This work was supported by the Russian Foundation for Basic Research, Division of Earth Sciences, Russian Academy of Sciences (fundamental program no. 5), and the Australian Research Council (IREX award, X00106611).

## REFERENCES

1. M. M. Frocht, *Photoelasticity* (Wiley, New York, 1941; OGIZ, Moscow, 1948), Vol. 1.
2. M. L. Zoback, M. D. Zoback, J. Adams, *et al.*, Nature **341**, 291 (1989).
3. K. M. Hansen and V. S. Mount, J. Geophys. Res. B **95**, 1155 (1990).
4. A. V. Karakin and Sh. A. Mukhamediyev, Fiz. Zemli, No. 11, 27 (1993) [Izvestiya, Phys. Solid Earth **29**, 956 (1993)].
5. N. I. Muskhelishvili, *Some Basic Problems of the Mathematical Theory of Elasticity* (Nauka, Moscow, 1966; Sijhoff & Noordhoff, Hardbound, 1977).
6. F. D. Gakhov, *Boundary Value Problems* (Nauka, Moscow, 1977; Dover, New York, 1990).
7. A. N. Galybin and Sh. A. Mukhamediev, J. Mech. Phys. Solids **47**, 2381 (1999).
8. Sh. A. Mukhamediev and A. N. Galybin, Fiz. Zemli, No. 8, 23 (2001) [Izvestiya, Phys. Solid Earth **37**, 636 (2001)].

*Translated by Sh. Mukhamediev*

*Doklady Physics, Vol. 49, No. 5, 2004, pp. 315–317. Translated from Doklady Akademii Nauk, Vol. 396, No. 2, 2004, pp. 191–193.*

**MECHANICS**

# Aerodynamic Interaction of Two Bodies in a Supersonic Flow

**I. A. Zhdan*, V. P. Stulov**, and P. V. Stulov**

Presented by Academician G.G. Chernyĭ February 5, 2004

Received February 5, 2004

Supersonic flows around systems of bodies were thoroughly studied at the Institute of Mechanics, Moscow State University, in the late 1970s and 1980s [1–6]. The results of the first experiments with a flow having a Mach number of M = 2.5 around two spheres when the line connected their centers was directed across the flow were published in [1]. In this case, configurations of the leading shock wave at various distances between the closest points of the spheres, as well as the maximum interaction distance beginning with which the interaction between the spheres is sharply weakened, were determined. The shape of the leading shock wave indicated both Mach and regular reflections of the shock from the symmetry plane between the spheres.

The results of approximate theoretical calculations and experimental studies of flows around a pair of cylinders were described in [2, 3]. A special algorithm was developed for calculating gas flows near the reflection point for the leading shock wave. Approximate calculations of the Mach stem showed a satisfactory agreement with available experimental data. For a pair of cylinders, the maximum interaction distance $h_{\max}$ turned out to be considerably larger than that for two spheres.

The results of two additional experiments with flows around a pair of spheres and cylinders for a Mach number of M = 1.75 were published in [4]. The approximate calculation of a flow near the triple point made it possible to obtain $h_{\max}$ values in the entire supersonic range of Mach numbers for the incident flow. These results were published in [4, 5]. The calculated data were obtained using the principle of the flow hypersonic stabilization, and they agree well with previous experiments. These results were analyzed together with the experimental data on the supersonic flow around a pair of wedges [7]. The comparison showed that even a significant variation of the body's shape (cylinder → wedge) did not considerably change the desired $h_{\max}$ value.

More recently, the data obtained for $h_{\max}$ in [4, 5] were used (in the explicit [8, 9] or implicit [10] forms) to estimate the behavior of a swarm of fragments after the disintegration of a meteoroid subjected to an aerodynamic load in the atmosphere.

Finally, in the concluding publication [6] of the series of studies under discussion, the experimental data for gas flows around a pair of cylinders were given for M = 6. The main attention was devoted to the range of distances between the bodies for which both Mach and regular reflections of a leading shock wave from the flow symmetry plane were possible. It turned out that the Mach configuration was always realized in the ambiguity interval.

Thus, at the early stage of the studies, it was reliably established that the interference distance between bodies was limited in a supersonic flow, and quantitative data on this distance were obtained. However, the quantitative characteristic of this interaction, which was manifested in the appearance of a transverse force repulsing the bodies, was not investigated in detail.

The goal of the present study is to compensate this drawback. Here, we analyze the results of systematic calculations for gas flows around a pair of finite cylinders with spherical ends for a Mach number of M = 6. The flow fields, as well as the drag and transverse forces, are determined. The calculated results are thoroughly compared with available experimental data. This comparison showed the high reliability of our calculations.

The software package used in numerically calculating was tested with experimental data. Special calculations were performed for comparing with the experimental results obtained at the preceding stage of the investigations.

The calculation series for gas flows around two spheres for M = 1.75 allowed us to compare the geometric parameters of the Mach configuration of the leading shock wave with the experimental data from [4]. The data concerning the distance $d_M$ of the tri-

---

*Institute of Mechanics, Moscow State University,*
*Vorob'evy gory, Moscow, 119899 Russia*
** e-mail: djo@access.izba.ru*
*** e-mail: stulov@imec.msu.ru*

**Table 1**

| $h$ | $d_M$, exp | $d_M$, calc |
|---|---|---|
| 1.12 | 0.428 | 0.435 |
| 1.32 | 0.276 | 0.246 |

Note: Distance $d_M$ of the triple point from the flow symmetry plane. Here, $h$ is the distance from the sphere's lower point to the symmetry plane. All distances are measured in the radius of either sphere or spherical ends of the cylinder.

ple point from the flow symmetry plane are presented in Table 1. These experimental data are obviously not considered as absolute, because they are obtained from the corresponding plots presented in [4].

We also compared the elements of the Mach configuration for a gas flow around two spheres for M = 3 with the experimental data obtained by Shvets *et al.*[1] These authors measured the pressure distribution over a sphere for M = 3 and $h = 0.38$. These results demonstrate a pressure increase for the polar angle $\theta \approx 60°$ measured from the front point of the sphere. This pressure increase is evidently caused by the incidence of the reflected shock onto the surface of the sphere. In the corresponding calculation variant, the coordinate $\theta = 66°$ of the shock reflected in the Mach configuration is obtained on the sphere's surface. In accordance with our estimates, the divergence of calculated and experimental results does not exceed 10%. This estimate includes all possible deviations.

The basic goal of the present study is the determination of the aerodynamic coefficients for bodies of various shapes with allowance for their interaction in supersonic flows. This problem was not analyzed at the previous stage of investigations. Reliable data on the aerodynamic characteristics of groups or pairs of bodies having a simple shape are also absent in available works. The only exclusion is work [11], where the motion of the fragments of a meteoritic body was considered at the initial stage after disintegration. The transverse velocity of the fragments formed due to disintegration was estimated with the transverse-force coefficient $c_y = 2$.

Here, the flow around a pair of circular cylindrical bodies with spherical ends is chosen as the object of the study. The length of the purely cylindrical part is denoted as $l$ so that the value $l = 0$ corresponds to a sphere. The two cylinders are located so that the length of the line connecting the centers of their cross-sections is perpendicular to the velocity of the incident flow. The flow is three-dimensional and has two mutually perpendicular symmetry planes. The line of their intersection coincides with the velocity direction of the incident flow.

The calculations are carried out for several $l$ values and various distances $2h$ between two closest points of the cylinder cross sections up to $h$ values virtually corresponding to the independent flows around each cylinder of the pair. At the previous stage of the studies, termination of the interaction was detected primarily by the position of the reflected shock: it was assumed that the interaction ceased when the reflected shock had passed downstream the body's surface. In this study, the criterion that the interaction ceased was the transverse-force coefficient.

The aerodynamic coefficients $c_x$ and $c_y$ of the drag and transverse forces, respectively, were calculated by the formulas

$$c_x = \frac{p_\infty}{0.5\rho_\infty V_\infty^2 S}\int_\Sigma p\cos\theta\, d\sigma,$$
$$c_y = \frac{p_\infty}{0.5\rho_\infty V_\infty^2 S}\int_\Sigma p\sin\theta\, d\sigma. \tag{1}$$

Here, $S = 2l + \pi$ is the midsection area of a cylinder, $\rho_\infty V_\infty^2/p_\infty = \gamma M^2$, the pressure $p$ in the integrand is normalized to the pressure $p_\infty$ in the incident flow, and the angle $\theta$ is described above. The results of the calculation are presented in Table 2 for four $l$ values and for $h$ values up to those corresponding to independent flows around each body of a pair.

Below, we determine the ultimate (hypersonic) values for the coefficients $c_x$ and $c_y$ for the configurations under study. In calculating the coefficients for a single sphere ($l = 0$) and a single cylinder ($l = \infty$), the pressure distribution estimated by the following Newton formula was used in formulas (1) ($p$ is a dimensional quantity):

$$p = \gamma M^2\cos^2\theta. \tag{2}$$

For flows around a pair of cylinders for $h = 0$, we assumed that the cross-section quadrant directed toward the other cylinder is a stagnation zone where $p = \gamma M^2$, and formula (2) is realized in the external quadrant. For flows around a pair of spheres for $h = 0$, it was assumed that the pressure in the octants directed toward the other sphere is distributed according to the modified Newton formula

$$p = \gamma M^2(\cos^2\theta - \sin\varphi\sin^2\theta). \tag{3}$$

Here, $\varphi$ ($\pi \le \varphi \le 2\pi$) is the circular angle. As before, formula (2) is valid in other octants. For all configurations, it was as usual assumed that $p = 0$ in the aerodynamic shadow. The resulting ultimate values are given in Table 3.

---

[1] These data are presented in the Report No. 3354 of the Institute of Mechanics, Moscow State University, 1986.

**Table 2**

| $l$ | Coefficient \ $h$ | 0.0 | 0.2 | 0.4 | 0.6 | 0.8 | 1.0 | 1.2 |
|---|---|---|---|---|---|---|---|---|
| 0 | $c_x$ | 1.030 | 0.860 | 0.850 | 0.855 | | | |
| | $c_y$ | 0.280 | 0.151 | 0.014 | 0.001 | | | |
| 2 | $c_x$ | 1.191 | 1.157 | 1.128 | 1.018 | 1.000 | | |
| | $c_y$ | 0.399 | 0.361 | 0.298 | 0.159 | 0.005 | | |
| 4 | $c_x$ | 1.250 | 1.230 | 1.210 | 1.185 | 1.048 | 1.059 | |
| | $c_y$ | 0.460 | 0.439 | 0.379 | 0.308 | 0.079 | 0.002 | |
| 6 | $c_x$ | 1.272 | 1.254 | 1.220 | 1.223 | 1.189 | 1.150 | 1.100 |
| | $c_y$ | 0.500 | 0.478 | 0.412 | 0.354 | 0.291 | 0.150 | 0.007 |

Comparison of Tables 2 and 3 shows that the existence of the aerodynamic shadow is the strongest assumption for calculating parameters given in Table 3. Therefore, the most noticeable difference of data on the transverse-force coefficient $c_y$ takes place for two spheres in the case of $h = 0$ ($c_y = 0.280$ and 0.750). Moreover, spread due to the finite length of a cylinder affects the case of $l = 6$. It is worth noting that the experiments with gas flows around cylinders for M = 1.75 and 2.5 were carried out for $l = 24$ [4].

Table 2 shows a significant increase in the maximum interaction distance with the length $l$. However, this distance is equal to about the cylinder radius even for $l = 6$.

In the previous studies [4, 5], the tangency of the body's surface by the reflected shock was considered as a criterion that the interaction ceased. Analysis of the calculated patterns of flows around the bodies shows that this criterion corresponds exactly to the condition of a significant decrease in the transverse-force coefficients $c_y$ shown in Table 2.

Below, our data on the shock-wave pattern under the conditions corresponding to the maximum interaction distance are quantitatively compared with the results reported in [4–6]. For flows around a pair of spheres ($l = 0$), the calculations made in [4, 5] yield the value $h_{\max} = 0.33$, whereas our numerical calculations yield $h_{\max} = 0.40$. For flows around cylinders ($l = \infty$), the calculations made in [4, 5] yield $h_{\max} = 1.56$, whereas this study for a cylinder with $l = 6$ yields $h_{\max} = 1.20$. It should be taken into account that the latter $h_{\max}$ value must increase with $l$.

**Table 3**

| Configuration | $c_x$ | $c_y$ |
|---|---|---|
| Single sphere | 1.000 | 0 |
| Pair of spheres $l = 0$, $h = 0$ | 1.318 | 0.750 |
| Single cylinder | 1.333 | 0 |
| Pair of cylinders $l = \infty$, $h = 0$ | 1.667 | 0.667 |

## ACKNOWLEDGMENTS

This work was supported by the Russian Foundation for Basic Research, project no. 02-01-00204.

## REFERENCES

1. O. M. Kuznetsov and V. P. Stulov, in *Aerodynamics of Solid Reentry into the Atmosphere of Planets: A Collection of Scientific Works* (Mosk. Gos. Univ., Moscow, 1983), pp. 12–16.
2. I. A. Zhdan, in *Gagarin Scientific Lectures on Cosmonautics and Aeronautics, 1985* (Nauka, Moscow, 1986), pp. 179–180.
3. I. A. Zhdan and V. P. Stulov, in *Fundamental Problems of Physics of Shock Waves: A Collection of Papers, Azau, 1987* (Chernogolovka, 1987), Vol. 1, Part 2, pp. 301–303.
4. A. L. Dmitriev, I. A. Dubrovina, O. M. Kuznetsov, I. A. Zhdan, and V. P. Stulov, in *Gagarin Scientific Lectures on Cosmonautics and Aeronautics, 1988* (Nauka, Moscow, 1989), pp. 45–56.
5. I. A. Dubrovina and V. P. Stulov, Vestn. Mosk. Univ., Ser. 1: Mat., Mekh., No. 5, 46 (1989).
6. B. E. Lyagushin, V. P. Stulov, and A. Yu. Yushkov, in *Studies of Gas Dynamics and Heat Exchange in the Complex Flows of Homogeneous and Multiphase Media* (Mosk. Gos. Univ., Moscow, 1990), pp. 26–29.
7. H. G. Hornung and M. L. Robinson, J. Fluid Mech. **123**, 155 (1982).
8. V. P. Korobeĭnikov, S. B. Gusev, and I. V. Semenov, Astron. Vestn. **31**, 370 (1997).
9. I. V. Nemchinov, O. P. Popova, and A. V. Teterev, Inzh.-Fiz. Zh. **72**, 1233 (1999).
10. I. V. Nemchinov and O. P. Popova, Astron. Vestn. **31**, 458 (1997).
11. Q. R. Passey and H. J. Melosh, Icarus **42**, 211 (1980).

*Translated by G. Merzon*

*Doklady Physics, Vol. 49, No. 5, 2004, pp. 318–322. Translated from Doklady Akademii Nauk, Vol. 396, No. 2, 2004, pp. 194–198.*
*Original Russian Text Copyright © 2004 by Kondaurov.*

**MECHANICS**

# Kinetics of First-Order Phase Transitions in a Thermoelastic Material

**V. I. Kondaurov**

Presented by Academician I.G. Goryacheva January 22, 2004

Received January 26, 2004

Solids can abruptly change their structure under intense mechanical and/or thermal loads. This means that a first-order phase transition occurs; i.e., the uniqueness of the constitutive relations (equations of state) disappears, and the transition from one branch of a material reaction to another is realized. Traditional description [1, 2] of the equilibrium of liquid (gaseous) phases separated by an interface leads to the equality of pressures and chemical potentials. Phase transitions in solids present a more complicated phenomenon. The basic result of investigations of this phenomenon [3–8] is the introduction of the chemical potential tensor, as well as allowance for the irreversibility of phase transitions, which is attributed to entropy sources concentrated at the interface. The dependence of these sources on the velocity of the interface and properties of the phases is unclear.

In this work, a kinetic model of first-order phase transitions in a thermoelastic body is proposed that makes it possible to partially overcome these difficulties. The model differs from the known approaches [9–11] in the explicit inclusion of the latent energy of structural changes. The features of the model are illustrated in application to a one-dimensional continuum. The relation between the parameter of the kinetic equation and dissipation source value is found. The effect of the kinetic parameter on the stress–strain dependence upon a phase transition is analyzed.

**1.** Let a thermoelastic material undergo the first-order phase transition under quasistatic load. At the interface moving with velocity $c$ in the direction of the normal vector $\mathbf{n}$, the following relations are valid [5, 8]:

$$\begin{gathered}[\mathbf{u}] = 0, \quad [\theta] = 0, \quad [\rho c] = 0, \\ [\nabla \otimes \mathbf{u}] = \mathbf{n} \otimes \mathbf{h}, \quad [\boldsymbol{\sigma}] \cdot \mathbf{n} = 0, \\ [\rho\psi] = \mathbf{n} \cdot \boldsymbol{\sigma} \cdot \mathbf{h} + \delta_*. \end{gathered} \tag{1}$$

They follows from the continuity of displacement $\mathbf{u}$, temperature $\theta$, and mass flux; equations of compatibility, equilibrium, and energy balance; and entropy inequality. Hereinafter, $\psi$ is the specific free energy, $\boldsymbol{\sigma}$ is the stress tensor, $\mathbf{e}$ is the small-strain tensor, $\mathbf{h} = -\frac{[\mathbf{v}]}{c}$, $\mathbf{v}$ is the velocity, and $\delta_*$ is the entropy source concentrated at the interface. For $\delta_* = 0$, the transition is reversible. For $\delta_* > 0$, the transition is irreversible, and the rearrangement of a crystal lattice is accompanied by various dissipative processes.

An important consequence of relations (1) is the condition for the jump of the normal components of the chemical potential tensor. For small strains of a thermoelastic body, this condition can be written as

$$\begin{gathered}\mathbf{n} \cdot [\boldsymbol{\chi}] \cdot \mathbf{n} = \delta_*, \\ \boldsymbol{\chi} \equiv \psi \mathbf{I} - \rho^{-1}(\boldsymbol{\sigma} \cdot \mathbf{e} + \mathbf{e} \cdot \boldsymbol{\sigma} - I_1(\mathbf{e})\boldsymbol{\sigma}), \end{gathered} \tag{2}$$

where $\boldsymbol{\chi}$ is the chemical potential tensor defined at the interface.

**2.** We consider a mixture of two phases of a thermoelastic material. Phases are considered as isotropic, the deviation of temperature from the initial value is small, $\vartheta = \theta - \theta_0 \ll 1$, and the scalar parameter $\omega$ is equal to the mass concentration of the second phase, $0 \le \omega \le 1$. The initial state of the medium is natural: $\boldsymbol{\sigma} = 0$, $\vartheta = 0$, $\omega = 0$. The free energy is specified by the expression

$$\begin{aligned}&\psi(\mathbf{e}, \vartheta, \omega) \\ &= \psi_f(\omega) + (1-\omega)\psi^{(1)}(\mathbf{e}, \vartheta) + \omega\psi^{(2)}(\mathbf{e}, \vartheta), \end{aligned} \tag{3}$$

where $\psi_f(\omega)$ is the latent energy of the transition such that $\psi_f(0) = 0$ and $\psi_f(1) = \psi_0$ is the latent energy of the total transition, whereas $\psi^{(i)}(\mathbf{e}, \vartheta)$, $i = 1, 2$, is the free

---

*Moscow Institute of Physics and Technology,*
*Institutskiĭ per. 9, Dolgoprudnyĭ,*
*Moscow oblast, 141700 Russia*
*e-mail: vk@mipt.ru*

energy of the phases. The terms in Eq. (3) are determined by the expressions

$$\rho\psi_f(\omega) = g\omega + \frac{1}{n+1}b\omega^{n+1}, \quad n > 0,$$

$$\rho\psi^{(1)}(\mathbf{e}, \vartheta)$$

$$= \frac{1}{2}K_1 I_1^2(\mathbf{e}) + \mu_1 J^2(\mathbf{e}) - \alpha_1\vartheta I_1(\mathbf{e}) - \frac{1}{2}c_1\vartheta^2, \tag{4}$$

$$\rho\psi^{(2)}(\mathbf{e}, \vartheta) = -p_0 I_1(\mathbf{e}) - \rho\eta_0\vartheta$$

$$+ \frac{1}{2}K_2 I_1^2(\mathbf{e}) + \mu_2 J^2(\mathbf{e}) - \alpha_2\vartheta I_1(\mathbf{e}) - \frac{1}{2}c_2\vartheta^2.$$

Here, $\mathbf{e}' = \mathbf{e} - \frac{1}{3}I_1\mathbf{I}$ is the deviator; $I_1 = \mathbf{e} : \mathbf{I}$ and $J^2 = \mathbf{e}' : \mathbf{e}'$ are the invariants of the strain tensor; $\alpha_i$ are the thermal-expansion coefficients; $K_i$ and $\mu_i$ are the volume compression and shear moduli, respectively; $c_i$ are the specific heat at constant strain (up to the factor $\theta_0$) of the phases; and $p_0$ and $\eta_0$ are the pressure and entropy of the second phase of the system ($\mathbf{e} = 0$, $\omega = 1$).

In order to write the kinetic equation, we consider the local entropy inequality

$$\rho\theta\dot{\eta} - \theta\nabla\cdot(\theta^{-1}\mathbf{q}) - \rho r \geq 0,$$

where $\eta$ is the specific entropy, $\mathbf{q}$ is the heat flux, and $r$ is the density of distributed heat sources. This inequality, along with Eqs. (3) and (4), leads to the relations

$$\boldsymbol{\sigma}(\mathbf{e}, \vartheta, \omega) = \frac{\rho\partial\psi}{\partial\mathbf{e}}$$

$$= (\hat{K}(\omega)I_1 - \hat{\alpha}(\omega)\vartheta - \omega p_0)\mathbf{I} + 2\hat{\mu}(\omega)\mathbf{e}',$$

$$\rho\eta(\mathbf{e}, \vartheta, \omega) = -\frac{\rho\partial\psi}{\partial\theta} = \hat{\alpha}(\omega)I_1 + \hat{c}(\omega)\vartheta + \omega\rho\eta_0, \tag{5}$$

$$\hat{a}(\omega) = (1-\omega)a_1 + \omega a_2, \quad a = K, \mu, \alpha, c,$$

$$\delta_f \equiv -\rho\dot{\omega}\frac{\partial\psi(\mathbf{e}, \vartheta, \omega)}{\partial\omega} \geq 0,$$

$$\delta_f + \theta^{-1}\mathbf{q}(\mathbf{e}, \vartheta, \omega, \nabla\vartheta)\cdot\nabla\vartheta \geq 0,$$

where $\delta_f$ is the dissipation of the structural transformation. A sufficient condition for the validity of the inequality $\delta_f \geq 0$ in any processes is the kinetic equation in the form

$$\dot{\omega} = -A\frac{\partial\psi(\mathbf{e}, \vartheta, \omega)}{\partial\omega},$$
$$A = (\tau b)^{-1}H(\omega)H(1-\omega) \geq 0, \tag{6}$$

where $\tau$ is the time of stress relaxation due to the structural changes in the material and $H(x)$ is the Heaviside step function. The derivative $-\frac{\partial\psi}{\partial\omega}$ is the "driving force" of the phase transition. In the direct transition, this quantity characterizes the balance between the energy released due to the partial unloading of the material near the nucleus of the new phase and absorbed energy associated with the latent energy of the transition. The situation is opposite in the reverse transition.

Using $(\boldsymbol{\sigma}, \vartheta, \omega)$ as independent variables, one arrives at the kinetics with the driving force equal to the derivative $-\frac{\partial\chi}{\partial\omega}$ of the scalar chemical potential (Gibbs potential) $\chi \equiv \psi - \boldsymbol{\sigma} : \mathbf{e}$. For the potential in the form of Eqs. (4), this derivative is equal to the difference between the chemical potentials of the pure phases minus the rate of an increase in the latent energy. Similarly, the choice of the variables $(\mathbf{e}, \eta, \omega)$ leads to the driving force expressed in terms of the internal energy density $u = \psi + \theta\eta$.

The linear relation between the transition rate and difference between the chemical potentials of the phases was often used to describe the kinetics of phase transitions [9, 10]. In contrast to those works, the model under development explicitly involves the latent energy depending on the transition depth. As will be shown below, it is this dependence that determines whether the transition is reversible or not, the conditions of the onset and termination of the structural transition, etc.

Thus, taking Eqs. (4)–(6) into account, we arrive at the kinetic equation

$$\dot{\omega} + \beta\omega^n = \beta\Phi(\mathbf{e}, \vartheta), \quad \beta \equiv \tau^{-1}H(\omega)H(1-\omega),$$

$$n \geq 1,$$

$$\Phi(\mathbf{e}, \vartheta) \equiv \frac{1}{2}\Delta K I_1^2 + \Delta\mu J^2 - \Delta\alpha\vartheta I_1 - \frac{1}{2}\Delta c\vartheta^2 \tag{7}$$

$$+ b^{-1}(p_0 I_1 + \rho\eta_0\vartheta - g),$$

where $\Delta a \equiv \frac{a_1 - a_2}{b}$, $a = K, \mu, \alpha$, and $c$ is the relative change in the thermoelastic moduli.

If the difference between the entropies of the phases in the initial state is such that $\frac{\rho\eta_0}{b} = O(1)$, the term $\rho b^{-1}\eta_0\vartheta$ on the right-hand side of Eq. (7) is much larger than the other terms, and the kinetics of the transition is linear in temperature. Structural transformations are determined only by thermal effects, whereas the effect of stresses is negligibly small, although both phases correspond to the thermoelastic solid material. If

$\frac{\rho\eta_0}{b} = O(\mathbf{e})$, all terms in Eq. (7) are of the same order, and the kinetics of the transformation depends substantially on the solid-state properties of the material.

**3.** Let us consider a one-dimensional continuum, or a cylindrical rod, in the isothermal approximation. The material of the rod can be in two phase states. The difference between Young's moduli of the phases is assumed to be much smaller than Young's modulus of the initial phase. The elastic potentials of the phases are given by the expression

$$u_f^0 = u_0 + \frac{1}{2}Ee_0^2, \quad u_1(e) = \frac{1}{2}Ee^2,$$
$$u_2(e) = \frac{1}{2}Ee^2 - Ee_0 e, \tag{8}$$

where $E$ is Young's modulus, $u_f^0$ is the latent energy of the phase transition, and $e_0$ is the natural strain of the phase transition that is associated with the difference between the densities of the phases. The stress–strain relation has the form

$$\sigma_1(e) = Ee, \quad \sigma_2(e) = E(e - e_0).$$

Relations (1) at the interface are reduced to the stress continuity condition $\sigma_1 = \sigma_2$ and energy-jump condition $u_2 - u_1 = \sigma_1(e_2 - e_1) - \delta_*$. Taking Eq. (8) into account, we obtain

$$e_1 = \frac{u_0 + \delta_*}{\sigma_0}, \quad e_2 = e_1 + e_0, \quad \sigma^{(12)} = \frac{u_0 + \delta_*}{e_0}, \tag{9}$$

where $\sigma_0 \equiv Ee_0$ and $\sigma^{(12)}$ is the stress at which the direct phase transition from the first phase to the second one occurs.

In the reverse phase transition, when the second phase is transformed into the first phase, we have

$$\sigma_1 = \sigma_2, \quad u_2 - u_1 = \sigma_1(e_2 - e_1) + \delta_*.$$

In view of Eq. (8), the stress $\sigma^{(21)}$ of the reverse phase transition is given by the expression

$$\sigma^{(21)} = \frac{u_0 - \delta_*}{e_0}. \tag{10}$$

According to Eqs. (9) and (10), the hysteresis of the phase transition is equal to

$$(\sigma^{(12)} - \sigma^{(21)})e_0 = 2\delta_*.$$

We now consider this problem in the kinetic model. Let, according to Eqs. (4) and (8), the elastic potential of the mixture of the two phases be equal to

$$u(\mathbf{e}, \omega) = \frac{1}{n+1}b\omega^{n+1}$$
$$+ g\omega + \frac{1-\omega}{2}Ee^2 + \frac{1}{2}\omega(Ee^2 - 2\sigma_0 e), \tag{11}$$
$$\sigma_0 \equiv Ee_0.$$

The kinetic equation for this case is written as

$$\dot{\omega} + \beta\omega^n = \beta b^{-1}(\sigma_0 e - g),$$
$$\beta \equiv \tau^{-1}H(\omega)H(1-\omega), \quad n \geq 1. \tag{12}$$

Stress is given by the formula

$$\sigma(e, \omega) = Ee - \sigma_0\omega. \tag{13}$$

For slow extension $e(t) = e_* + e_0 z(t)$, where $z(0) = 0$ and $\tau\dot{z}(t) \ll 1$, and $e_* = \frac{g}{\sigma_0}$ is the strain at which the transition begins, the structure parameter is expressed as

$$\omega^n(t) = b^{-1}\sigma_0 e_0 z(t). \tag{14}$$

Strain $e_{**}$ at which the phase transition is completed ($\omega = 1$) is determined from the equation $b^{-1}\sigma_0(e_{**} - e_*) = 1$. In order to express quantities $b$ and $g$ in terms of the parameters $E$, $e_0$, and $u_0$ of the material and to determine the dissipation $\delta_*$ of the structural transformation, we use the relations

$$e_* = e_1, \quad e_{**} = e_2, \quad \frac{b}{n+1} + g = u_0 + \frac{1}{2}\sigma_0 e_0.$$

The first two equalities are the conditions of coincidence of strains at which the phase transition begins and completes in the kinetic model and strong-discontinuity model. The third relation is the condition that the energy

$$u_f(\omega) = \frac{b\omega^{n+1}}{n+1} + g\omega$$

for $\omega = 1$ is equal to the latent energy $u_0 + \frac{1}{2}\sigma_0 e_0$. Taking Eq. (9) into account, we obtain

$$b = \sigma_0 e_0, \quad g = u_0 - \sigma_0 e_0\left(\frac{1}{2} - \frac{1}{n+1}\right),$$
$$\delta_* = \sigma_0 e_0\left(\frac{1}{2} - \frac{1}{n+1}\right).$$

Therefore, dissipation $\delta_*$ is uniquely related to the parameter $n$ of kinetic equation (12). The approxima-

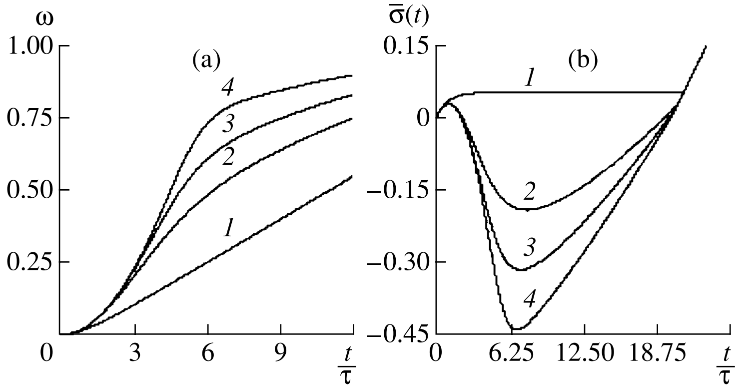

**Fig. 1.** (a) Structure parameter $\omega(t)$ and (b) stress $\bar{\sigma}(t)$ for uniform-load rate $\frac{\varepsilon\tau}{e_0} = 0.05$ and kinetic parameter $n$ = (*1*) 1, (*2*) 2, (*3*) 3, and (*4*) 5.

tion $\delta_* = 0$ of the reversible phase transition [3, 4] in the framework of the model under consideration leads to the necessity of using the linear kinetic equation with $n = 1$. The presence of dissipation corresponds to the parameter $n > 1$. In view of Eqs. (13) and (14), stress has the form

$$\frac{\sigma - Ee_*}{\sigma_0} = z(t) - z^{1/n}(t). \qquad (15)$$

The function $\omega(t)$ found from Eq. (14) and the function $\bar{\sigma}(t) \equiv \frac{\sigma - Ee_*}{\sigma_0}$ given by formula (15) are shown in Figs. 1a and 1b, respectively, for load $z(t) = \frac{\varepsilon t}{e_0}$ with rate $\frac{\varepsilon\tau}{e_0} = 0.05$. Lines *1*–*4* correspond to the kinetic parameter $n = 1$, 2, 3, and 5, respectively. For linear kinetics ($n = 1$), stress $\sigma(t)$ monotonically becomes constant, which, for $\varepsilon \to 0$, tends to stress $\bar{\sigma} = 0$ realized in the model of the transition with a strong-discontinuity surface. Kinetics with $n > 1$ is characterized by the existence of an interval where $\sigma(t)$ decreases. The amplitude and negative slope increase with both an increase in $n$ and a decrease in the strain rate.

High-rate loading $\left(\frac{\varepsilon\tau}{e_0} \gg 1\right)$ is accompanied by a monotonic increase in stresses for all values of $n$. The large order of the kinetic equation is preferable, because the transition from one deformation branch to another occurs in this case through the section of a curve close to horizontal. This enables one to introduce stress characteristic of the phase transition under high-rate loading.

Thus, the above model of the kinetics of first-order phase transitions in a thermoelastic solid satisfies the following requirements.

(i) Dissipation of the structural transformation is nonnegative in any processes of thermal and mechanical loading.

(ii) There is the threshold thermomechanical load above which the transition begins; i.e., inclusions of a new phase are formed. The existence of the threshold load is not an additional assumption but is determined by the properties of the phases of a material.

(iii) There are limiting thermal and/or mechanical loads corresponding to the complete phase transition. The condition of the complete transition, as well as the existence of the threshold load, follows from the thermomechanical properties of the material.

(iv) Kinetics is related to the thermomechanical properties of the material. This relation presents the dependence of the formation and growth of new-phase nuclei on the thermoelastic moduli of the phases.

(v) The character of a first-order phase transition in solids (reversibility and irreversibility) depends explicitly on the order of the kinetic equation. This conclusion is fundamentally novel.

## ACKNOWLEDGMENTS

This work was supported by the Division of Power Engineering, Mechanical Engineering, Mechanics, and Control Processes, Russian Academy of Sciences (program "Accumulation of Damages, Fracture, Wear, and Structure Changes in Materials under Intense Mechanical, Thermal, and Radiation Actions") and the Russian Foundation for Basic Research (project no. 03-05-64643).

## REFERENCES

1. J. W. Gibbs, *Thermodynamics. Statistical Mechanics*, in *The Collected Works of J. Willard Gibbs* (Yale Univ. Press, New Haven, 1948; Nauka, Moscow, 1982).
2. L. D. Landau and E. M. Lifshitz, *Course of Theoretical Physics*, Vol. 5: *Statistical Physics* (Nauka, Moscow, 1995; Pergamon, Oxford, 1980).
3. M. A. Grinfel'd, Dokl. Akad. Nauk SSSR **251**, 824 (1980).
4. L. M. Truskinovskiĭ, Geokhimiya, No. 12, 1730 (1983).
5. V. I. Kondaurov and L. V. Nikitin, Izv. Ross. Akad. Nauk, Mekh. Tverd. Tela, No. 6, 49 (1983).
6. M. E. Gurtin, Arch. Ration. Mech. Anal. **84**, 1 (1983).
7. N. F. Morozov, I. R. Nazyrov, and A. B. Freĭdin, Dokl. Akad. Nauk **346**, 188 (1996) [Phys. Dokl. **41**, 40 (1996)].
8. V. I. Kondaurov and V. E. Fortov, *Fundamentals of Thermal Mechanics of Condensed Media* (MFTI, Moscow, 2002).
9. E. Fried and G. Grach, Arch. Ration. Mech. Anal. **138**, 355 (1997).
10. J. K. Knowles, Comput. Mech. **22**, 429 (1999).
11. V. I. Levitas and D. L. Preston, Phys. Rev. B **66**, 134206 (2002).

*Translated by R. Tyapaev*

Doklady Physics, Vol. 49, No. 5, 2004, pp. 323–327. Translated from Doklady Akademii Nauk, Vol. 396, No. 2, 2004, pp. 199–203.
Original Russian Text Copyright © 2004 by Petrov.

## MECHANICS

# Asymptotic Expansion Law for an Axisymmetric Free Jet

**A. G. Petrov**

Presented by Academician G.G. Chernyĭ January 21, 2004

Received January 23, 2004

For the problem of the axisymmetric cavitation flow, Gurevich (1947) and Levinson (1946) independently established the following asymptotic expansion law for the free boundary (jet) on which the velocity is everywhere equal to the velocity $v_\infty$ at infinity:

$$\frac{Y^2}{4} = RX(\ln X)^{-1/2}, \quad X \to \infty. \tag{1}$$

Here, $X$ and $Y$ are cylindrical coordinates and $R$ is a constant ($X$, $Y$, and $R$ have the dimension of length).

Levinson proceeded from the integral identity for a harmonic function and the condition that velocity is constant at the free boundary. He obtained the next term

$$-\frac{1}{4}RX\ln\ln X(\ln X)^{-3/2}$$

in the asymptotic expansion.

Gurevich reduced the problem to the determination of the boundary of a semi-infinite finite-drag body and obtained asymptotic relation (1), as well as established the following relation between the coefficient $R$ and force $F$ acting on a semi-infinite body:

$$R^2 = \frac{F}{2\pi\rho v_\infty^2}, \tag{2}$$

which was absent in Levinson's study. Moreover, the additional asymptotic term derived by Levinson follows from the asymptotic law written in the implicit form

$$\frac{8F}{\rho\pi v_\infty^2} \approx \frac{Y^4}{X^2}\ln\frac{X^2}{Y^2},$$

obtained by Gurevich [1, p. 466].[1] Detailed references are given in [1, 2].

In this study, the integro-differential equation for a free jet is derived and its exact integral is obtained using the variational asymptotic theory for thin cavities. Employing this integral, a one-parameter family of the solutions of this equation is constructed. The family parameter $R$ is expressed in terms of the force from Gurevich formula (2). The equation and asymptotic expansion are independent of the cavitator shape, are as accurate as possible in this sense, and appreciably improve the existing expansions. Further improvements will depend on the shape of the body in a flow.

## AXISYMMETRIC FLOW AROUND A THIN BODY

**Formulation of the problem.** We consider the problem of the steady potential flow of an ideal fluid around an elongated (thin) body of revolution. All lengths are scaled on the body half-length $l_x$, and all velocities, on the incident flow velocity at infinity $v_\infty$. Then, the body boundary in a meridional plane can be described by the equation $y = \chi f(x)$, $-1 \le x \le 1$, where the small parameter $\chi = \frac{l_y}{l_x}$ is the ratio of the body thickness $2l_y$ to its length.

The velocity field potential $\Phi(x, y)$ is obtained by solving the boundary value problem

$$\Delta\Phi = \frac{\partial^2\Phi}{\partial x^2} + \frac{\partial^2\Phi}{\partial y^2} + \frac{1}{y}\frac{\partial\Phi}{\partial y} = 0,$$

$$\frac{\partial\Phi}{\partial y}\left(\frac{\partial\Phi}{\partial x}\right)^{-1} = \chi\frac{df}{dx}, \quad |x| \le 1, \quad y = \chi f(x), \tag{3}$$

$$\Phi \to x, \quad x^2 + y^2 \to \infty,$$

where $x$ and $y$ are the dimensionless cylindrical coordinates.

---

[1] This was noticed by O.V. Voinov.

*Institute for Problems in Mechanics, pr. Vernadskogo 101, Moscow, 119526 Russia*
*e-mail: petrov@ipmnet.ru*

1028-3358/04/4905-0323$26.00 © 2004 MAIK “Nauka/Interperiodica”

**The solution** is sought in the form of sources distributed along the $x$ axis

$$\Phi = x + \chi^2 \Pi(q), \quad \Pi(q) = \int_{-1}^{1} \frac{q(\xi)d\xi}{r(\xi)}, \tag{4}$$
$$r(\xi) = \sqrt{(x-\xi)^2 + y^2}.$$

The expansion of the solution for $y \to 0$ with the accuracy of $y^2 \ln y$ was given by Colle [3]. It can be expressed in terms of the integral operators $L(q)$ and $I(q)$ as follows:

$$L(q) = -q(x)\ln(1-x^2) + I(q),$$
$$I(q) = \int_{-1}^{1} \frac{q(x) - q(\xi)}{|x-\xi|} d\xi, \tag{5}$$

$$\Pi(q) = -L(q) + q\ln\frac{4}{y^2} + O(y^2 \ln y). \tag{6}$$

The expression $\Pi(q)$ in the form of series convergent in the parameter $y$ was studied by Fedoryuk [4] and makes it possible to determine the function $q(x)$ from the boundary condition with an arbitrary accuracy with respect to the small parameter $\chi$.

From boundary condition (4), we can obtain

$$\chi^2 q(x) = -z'(x) + O(\chi^4 \ln\chi),$$
$$z(x) = \frac{1}{4}\chi^2 f^2(x), \quad z'(x) = \frac{dz}{dx}.$$

Substituting this expression into Eqs. (6) and (4), we derive an asymptotic expansion of the velocity field potential in the vicinity of the body surface for $y \sim \chi$ and then obtain the velocity and pressure distributions over the body surface

$$\frac{v^2}{v_\infty^2} = \left(\frac{\partial\Phi}{\partial x}\right)^2 + \left(\frac{\partial\Phi}{\partial y}\right)^2$$
$$= 1 + 2\frac{d}{dx}L(z') + 2z''\ln z + \frac{z'^2}{z} + O(\chi^4 \ln^2\chi). \tag{7}$$

## ASYMPTOTIC EXPANSIONS FOR THIN AXISYMMETRIC CAVITIES

Very simple results can be obtained in the approximation $\frac{v^2}{v_\infty^2} \sim 1 + 2z''\ln\chi^2$ in Eq. (7) (plane cross section hypothesis). The cavity shape was determined in this approximation in [5, 6] and with allowance for integral terms in [7] with an error of the order $\frac{1}{\ln\chi}$ and $\frac{1}{\ln\chi^2}$, respectively. The force acting on the cavitator cannot be calculated. The inclusion of all terms of expansion (7) and application of the variational principle appreciably improve the accuracy of the asymptotic expansions for both the cavity shape and force [8–10].

**Integro-differential equation of the cavity.** If the constant velocity $v_k$ at the cavity boundary is expressed in terms of the cavitation number $\sigma = \frac{v_k^2}{v_\infty^2} - 1$, then from Eq. (7) we obtain the equation of the free boundary in the cavitation-flow problem in accordance with the Riabouchinsky scheme

$$z''\ln z + \frac{z'^2}{2z} + \frac{d}{dx}L(z') = \frac{\sigma}{2} \tag{8}$$

with an error of the order $\chi^4 \ln^2\chi$. For a thick cavitator, we have $z(\pm1) = \frac{R^2}{l_x^2} \sim \chi^4$ and, without loss in the accuracy of the approximation, the conditions $z(-1) = z(1) = 0$ can be taken at the free jet shedding points.

**Variational formulation.** Equation (8) has a variational formulation following from the Riabouchinsky variational principle. In [8–10], it was shown that solution (8) is the extremum of the energy functional

$$\frac{U}{2\pi\rho v_\infty^2 l_x^3} = \int_{-1}^{1} [\sigma z + z'^2 \ln z + z' L(z')]dx. \tag{9}$$

**Drag force.** In order to overcome the difficulties of calculating the force acting on the cavitator at small cavitation numbers, Garabedian expressed the force acting on a disk and cones in terms of the extremum value of the energy functional $F \approx \frac{3}{2}\frac{U_0}{l_x}$ [1, 11]. In [8–10], it was shown that the Garabedian formula is exact for cones and has a relative error of about the ratio of the cavitator dimension $R$ to the cavity length $l_x$ for other cavitator shapes.

For solving Eq. (8), a parameter $\varepsilon$ is introduced as follows: $\sigma = \varepsilon\ln\frac{1}{\varepsilon}$. The solution of the equation for a thick cavitator is represented by a power series in the parameter $\varepsilon_1 = \left(\ln\frac{1}{\varepsilon}\right)^{-1}$. In particular, one can obtain both the expansion for the inverse aspect ratio of the cavity (the ratio of its midsection radius to the half-length) $\chi^2 = 4z(0) = \varepsilon(1 + \varepsilon_1 + \ldots)$ and the asymptotic formula for $1 + x \to 0$, which is required for matching with the asymptotic law of jet expansion:

$$z(x) = \varepsilon(1+x)\left[1 - \frac{1}{2}\left(\ln\frac{1}{\varepsilon}\right)^{-1}\ln(1+x) + \ldots\right]. \tag{10}$$

The drag force is expressed in terms of the extremum value of the functional $U$ given by Eq. (9) as

$$F = \frac{3}{2l_x}U_0 = \pi\rho v_\infty^2 l_x^2 \varepsilon^2\left(\frac{1}{2}\ln\frac{1}{\varepsilon} + 1 - \ln 2 + \dots\right). \quad (11)$$

The above formulas provide the basis for the calculation of the geometric and force characteristics of the cavitation flow.

## INTEGRO-DIFFERENTIAL EQUATION OF THE FREE BOUNDARY

The equation determining the asymptotic law of jet expansion can be derived from Eq. (9) by passing to the limit $\sigma \to 0$. We introduce the dimensional variables

$$X = l_x(1+x), \quad Z = \frac{Y^2}{4} = l_x^2 z \quad (12)$$

and the one-parameter family of integral operators

$$L(Z, l_x) = -Z(X)\ln[X(2l_x - X)] + \int_0^{2l_x} \frac{Z(X) - Z(X')}{|X - X'|}dX'. \quad (13)$$

At $l_x = 1$, the operator $L(Z, 1)$ is identical to the operator $L(z)$ defined by Eq. (5). In the new variables, Eq. (9) takes the form

$$Z''\ln Z + \frac{Z'^2}{2Z} + \frac{d}{dx}L(Z', l_x) = \frac{\sigma}{2}.$$

We now pass to the limit $\sigma \to 0$ fixing the cavitator shape. The pressure distribution over the cavitator surface and the force acting on it do not change. From expression (11) for the force, it follows that $l_x \to \infty$ in this case. For the free jet $Z(X)$, we obtain the equation

$$Z''\ln Z + \frac{Z'^2}{2Z} = -\lim_{l_x\to\infty}\frac{d}{dX}L(Z', l_x)$$
$$= -\lim_{l\to\infty}\frac{d^2}{dX^2}N(Z', l), \quad (14)$$
$$N(Z', l) = \int_0^l Z'(X')\ln|X - X'|\operatorname{sgn}(X' - X)dX'.$$

When passing to the limit, the integration range is divided into the intervals $(0, X)$ and $(X, l)$, where variables are changed as $X' = Xt$ and $X' = \frac{X}{t}$, respectively. In the limit $l \to \infty$, we obtain the integrals over the interval $t \in (0, 1)$. The result of the passage to the limit is formulated as follows.

**Theorem.** *Let a function* $\phi(X)$ *be such that* (i) *the second derivative* $\phi''(X)$ *exists on the interval* $(0, \infty)$ *and* (ii) $\frac{\phi(l)}{l} \to 0$ *and* $\phi'(l)\ln l \to 0$ *for* $l \to \infty$. *Then, we have*

$$\lim_{l\to\infty}\frac{d^2}{dX^2}N(\phi(X), l) = N_\infty(\phi(X))$$
$$= X\int_0^1 \phi''\left(\frac{X}{t}\right)(\ln X + \ln(1-t) - \ln t)\frac{dt}{t^2}$$
$$-\frac{d^2}{dX^2}\left[X\int_0^1 \phi(Xt)(\ln X + \ln(1-t))dt\right], \quad (15)$$

*if the corresponding integrals are convergent.*

Thus, we arrive at the following integro-differential equation for a free jet:

$$Z''\ln Z + \frac{Z'^2}{2Z} = -N_\infty(Z') + O\left(\frac{1}{X^2}\right), \quad (16)$$

where $N_\infty(Z')$ stands for integral transform (15), for which an asymptotic expansion for $X \to \infty$ is constructed below.

## ASYMPTOTIC EXPANSION OF THE LIMITING INTEGRAL TRANSFORM

We will construct an asymptotic expansion for $N_\infty(\phi(X))$ with the function $\phi(X) = f(\ln X)$. We substitute this function into Eq. (15) and change the variable as $\lambda = \ln X$. Using the differentiation formulas for arbitrary functions $\Phi(\lambda)$ and $f(\lambda \pm a)$

$$X\frac{d\Phi(\ln X)}{dX} = \frac{d\Phi(\lambda)}{d\lambda},$$
$$\frac{\partial}{\partial\lambda}f(\lambda \pm a) = \pm\frac{\partial}{\partial a}f(\lambda \pm a),$$

one can reduce the integral transform to the form

$$e^\lambda N_\infty(f(\lambda)) = \int_0^1 F(\lambda, t)dt,$$

$$F(\lambda, t) = (\lambda + a_1)\left(\frac{\partial^2}{\partial a^2} + \frac{\partial}{\partial a}\right)(f(\lambda - a) - f(\lambda + a))$$

$$-f(\lambda + a) - 2\frac{\partial}{\partial a}f(\lambda + a) - a\left(\frac{\partial^2}{\partial a^2} + \frac{\partial}{\partial a}\right)f(\lambda - a),$$

$$a = \ln t, \quad a_1 = \ln(1 - t).$$

The functions $f(\lambda \pm a)$ are presented as the Maclaurin series. Substituting them into the integrand $F(\lambda, t)$, we obtain

$$F(\lambda, t) = \lambda \sum_{k=0}^{\infty} A_k(t) f^{2k+1}(\lambda) + \sum_{k=0}^{\infty} B_k(t) f^k(\lambda),$$

where $A_k$ and $B_k$ are polynomials in functions $a(t)$ and $a_1(t)$ of a rather simple form. The integrals of these functions can be calculated as

$$\int_0^1 A_0 dt = -2, \quad \int_0^1 B_0 dt = -1,$$

$$\int_0^1 B_{2k+1} dt = -2\zeta(2k+1),$$

where $\zeta(2k+1)$ is the value of the Riemann zeta function at the points $2k+1$, $k = 1, 2, \ldots$. Thus, we have $\zeta(3) = 1.20206$, $\zeta(5) = 1.03693$, $\zeta(7) = 1.00835$, etc.

All other integrals of $A_k$ and $B_k$ are zero. Thus, the integral $\int_0^1 F dt$ is calculated exactly, and the integral transform is finally expressed as

$$e^{\lambda} N_{\infty}(f(\lambda)) = -f(\lambda) - 2\lambda f'(\lambda) - 2\sum_{k=1}^{\infty} \zeta(2k+1) f^{2k+1}(\lambda). \qquad (17)$$

## INTEGRAL OF THE EQUATION FOR THE FREE BOUNDARY

We substitute Eq. (17) into Eq. (16) and multiply both sides of the equation by $2X\frac{dZ}{dX} = 2e^{\lambda} f(\lambda)$. Thus, we obtain the free jet equation in the form

$$\frac{d}{d\lambda}[f^2(\lambda)\ln Z] = 2f^2(\lambda) + 4\lambda f(\lambda) f'(\lambda) + 4\sum_{k=1}^{\infty} \zeta(2k+1) f(\lambda) f^{2k+1}(\lambda) + O(e^{-\lambda}).$$

All terms on the right-hand side can be represented in the form of a derivative with respect to the variable λ. Then, we obtain the exact integral of the equation

$$(2\lambda - \ln Z) f^2(\lambda) = 1 - 2\sum_{k=1}^{\infty} \zeta(2k+1) S_{2k}(f) + O(e^{-\lambda}), \qquad (18)$$

$$Z(X) = e^{\lambda}(f(\lambda) - f'(\lambda) + f''(\lambda) + \ldots),$$

$$\lambda = \ln X, \quad S_{2k}(f) = \sum_{m=0}^{2k} (-1)^m f^m(\lambda) f^{2k-m}(\lambda).$$

The second equation can be derived by representing $Z(X)$ in the form of the integral $Z(X) = \int f(\lambda) e^{\lambda} d\lambda$ and integrating it by parts.

## ASYMPTOTIC LAW OF JET EXPANSION

The $n$th approximation of the solution of Eq. (18) has the asymptotic form

$$f_n(\lambda) = \lambda^{-1/2}[1 + P_1(u)\lambda^{-1} + P_2(u)\lambda^{-2} + \ldots + P_n(u)\lambda^{-n}],$$

$$Z_n(\lambda) = e^{\lambda}\lambda^{-1/2}[1 + Q_1(u)\lambda^{-1} + Q_2(u)\lambda^{-2} + \ldots + Q_n(u)\lambda^{-n}], \qquad (19)$$

where $P_n(u)$ and $Q_n(u)$ are the polynomials of degree $n$ in the variable $u = \ln\lambda$. The asymptotic terms $f_n(\lambda)$, $n = 0, 1, 2, \ldots$, are found successively from the equations

$$f_0 = \lambda^{-1/2}, \quad Z_0 = e^{\lambda}\lambda^{-1/2},$$

$$(2\lambda - \ln Z_0) f_1^2(\lambda) = 1, \quad Z_1 = e^{\lambda}(f_1(\lambda) - f'_0(\lambda)),$$

$$(2\lambda - \ln Z_1) f_2^2(\lambda) = 1,$$

$$Z_2 = e^{\lambda}(f_2(\lambda) - f'_1(\lambda) + f''_2(\lambda)),$$

$$(2\lambda - \ln Z_2) f_3^2(\lambda) = 1 - 2\zeta(3)(2f_0(\lambda) f''_0(\lambda) - (f'_0(\lambda))^2), \ldots.$$

We thence successively calculate the polynomials

$$P_1 = -\frac{1}{4}u, \quad Q_1 = -\frac{1}{4}u + \frac{1}{2},$$

$$P_2(u) = \frac{3}{32}u^2 - \frac{1}{8}u + \frac{1}{4}, \quad Q_2 = \frac{3}{32}u^2 - \frac{1}{2}u + \frac{5}{4},$$

$$P_3 = -\frac{5}{128}u^3 + \frac{1}{8}u^2 - \frac{3}{8}u + \frac{9}{16} - \frac{5}{4}\zeta(3), \qquad (20)$$

$$Q_3 = -\frac{5}{128}u^3 + \frac{23}{64}u^2 - \frac{29}{16}u + \frac{57}{16} - \frac{5}{4}\zeta(3).$$

The above expansions are asymptotic and, generally speaking, divergent series, so that their accuracy of approximation is limited. A more accurate approach to the calculation of a free jet can be proposed. Substituting the asymptotic forms for the sums $S_{2k} \sim (\ln X)^{-2k+1}$ into the right-hand side of Eq. (18), we obtain, with a corresponding accuracy, an ordinary differential equation for $Z(X)$, which can be solved numerically. With an accuracy to $(\ln X)^{-3}$, we obtain $\ln \frac{X^2}{Z}\left(\frac{dZ}{dX}\right)^2 = 1$ or

$$\frac{dZ}{d\lambda} = e^{\lambda}(2\lambda - \ln Z)^{1/2}.$$

In this case, the error of the right-hand side can be evaluated as $2S_2 \approx \frac{5}{2}\lambda^{-3}$.

After the dimensionless function $Z(X)$ has been calculated, using the symmetry $X \to RX$ and $Z \to R^2 Z$ of Eq. (16), we obtain the one-parameter family of the solutions $\frac{Y^2(X)}{4} = R^2 Z\left(\ln\frac{X}{R}\right)$, where the dynamic parameter is determined from Gurevich formula (2).

## DRAG FORCE

The relation between the dynamic parameter $R$ and the force $F$ can be obtained from the coincidence of asymptotic formulas (10) for $l_x \to \infty$, $1 + x \to 0$ and (19) for $X = l_x(1 + x) \to \infty$. They coincide for $l_x = R\frac{2}{\varepsilon}\left(\ln\frac{2}{\varepsilon}\right)^{-1/2}$. Substituting this expression for $l_x$ into Eq. (11), for $\varepsilon \to 0$ we arrive at Gurevich formula (2) determining the relation between the coefficient $R$ and the drag force in the asymptotic law of jet expansion. The leading terms of the expansion of the solution family obtained above coincide with law (1) derived by Levinson and Gurevich.

## ACKNOWLEDGMENTS

I am grateful to G.G. Chernyĭ, V.F. Zhuravlev, and O.V. Voinov for discussion of the results.

## REFERENCES

1. M. I. Gurevich, *Theory of Ideal Liquid Jets* (Nauka, Moscow, 1979).
2. G. Birkhoff and E. Zarantonello, *Jets, Wakes, and Cavities* (New York, 1957; Mir, Moscow, 1964).
3. J. Colle, *Perturbation Methods in Applied Mathematics* (Blaisdell Publishing Company, Waltham, 1968; Mir, Moscow, 1972).
4. M. V. Fedoryuk, *Asymptotic Behavior, Integrals, and Series* (Nauka, Moscow, 1987), pp. 39–43.
5. Yu. L. Yakimov, Prikl. Mat. Mekh. **32** (3) (1968).
6. G. V. Logvinovich, *Hydrodynamics of Flows with Free Boundaries* (Naukova Dumka, Kiev, 1969).
7. G. V. Logvinovich and V. V. Serebryakov, in *Hydromechanics* (Naukova Dumka, Kiev, 1975), issue 32, pp. 47–54.
8. A. G. Petrov, Dokl. Akad. Nauk SSSR **257**, 1323 (1981) [Sov. Phys. Dokl. **26**, 382 (1981)].
9. A. G. Petrov, Dokl. Akad. Nauk SSSR **282**, 1320 (1985) [Sov. Phys. Dokl. **30**, 453 (1985)].
10. A. G. Petrov, Prikl. Mekh. Tekh. Fiz., No. 5, 45 (1986).
11. P. R. Garabedian, Bull. Am. Math. Soc. **62**, 642 (1956).

*Translated by M. Lebedev*

*Doklady Physics, Vol. 49, No. 5, 2004, pp. 328–331. Translated from Doklady Akademii Nauk, Vol. 396, No. 2, 2004, pp. 204–207.*
*Original Russian Text Copyright © 2004 by Urmancheev, Kireev.*

**MECHANICS**

# Steady Flow of a Fluid with an Anomalous Temperature Dependence of Viscosity

**S. F. Urmancheev* and V. N. Kireev****

Presented by Academician R.I. Nigmatulin January 14, 2004

Received January 28, 2004

Variation of viscosity strongly affects the pattern of a fluid flow. Certain features of flows of fluids with variable viscosity were described in [1–4]. Monotonically decreasing temperature dependence characteristic for the viscosity of most fluids can be violated for substances where both polymerization and depolymerization of molecules occur in a limited temperature range. Liquid sulfur, whose viscosity has a peak temperature dependence, is among these fluids [5, 6]. Certain features of a liquid-sulfur flow in a heat exchanger were considered in [7].

This paper presents the numerical results for a flow of an incompressible fluid, whose viscosity has an anomalous temperature dependence, in a two-dimensional channel with a nonuniform temperature field. It is established that the flow pattern is determined by the structure of a "viscous barrier." The effects of both the shape of the nonmonotonic dependence and ambient conditions on the basic features of the flow are also studied.

We consider a flow of a certain model fluid, whose viscosity depends nonmonotonically on temperature and which will be called abnormally viscous. This dependence corresponds to equilibrium between the polymerization and depolymerization of molecules at a given temperature. For slow flows, relaxation processes in the fluid are neglected and its viscosity is considered as a single-valued function of temperature.

We consider a flow of the anomalously viscous fluid subjected to pressure drop in a two-dimensional channel with length $L$ and height $h$. The channel is sufficiently long ($L \gg h$), and we introduce the small parameter $\varepsilon = \frac{h}{L}$. The $Ox$ axis of the Cartesian coordinate system is directed along the channel. The inflowing-fluid temperature is denoted as $T_0$, while channel walls are assumed to be maintained at the constant temperature $T_w$ (Fig. 1).

The temperature dependence of kinematic viscosity $\nu(T)$ is approximated by the expression

$$\nu(T) = \nu_0(1 + A\exp(-B(T - T_*)^2)),$$

where $A = \frac{\nu_1}{\nu_0} - 1$ and $B$ are the parameters of the anomalous dependence; $\nu_1$ and $\nu_0$ are the maximum and minimum of viscosity in the temperature range $[T_0, T_w]$,

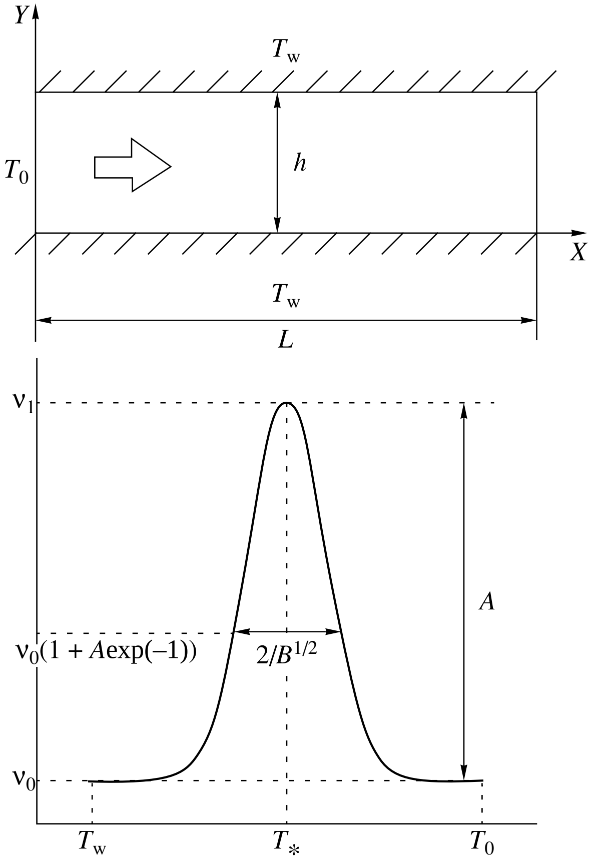

**Fig. 1.** Channel configuration (flow direction is shown by an arrow) and temperature dependence of the fluid viscosity.

---

*Institute of Mechanics, Ufa Scientific Center,*
*Russian Academy of Sciences, ul. Karla Marksa 12,*
*Ufa, 450000 Bashkortostan, Russia*
* *e-mail: said@anrb.ru*
** *e-mail: kireev@anrb.ru*

respectively; and $T_* = \dfrac{T_0 + T_w}{2}$. This dependence is plotted in Fig. 1.

Dimensionless variables and criteria are introduced as follows:

$$\bar{x} = \frac{x}{L}, \quad \bar{y} = \frac{y}{h}, \quad \bar{u} = \frac{\varepsilon u}{v_0}, \quad \bar{v} = \frac{v}{v_0}, \quad \bar{t} = \frac{v_0}{h}t,$$

$$\bar{p} = \frac{\varepsilon^2 p}{\rho v_0^2}, \quad \bar{T} = \frac{T - T_w}{T_0 - T_w}, \quad \bar{\nu} = \frac{\nu - \nu_0}{\nu_1 - \nu_0},$$

$$\mathrm{Re} = \frac{h v_0}{\nu_0}, \quad \mathrm{Pe} = \frac{h v_0}{\chi}.$$

Here, $u$ and $v$ are the $Ox$ and $Oy$ components of the velocity vector, $p$ is the pressure, $t$ is time, $T$ is the temperature, $\rho$ is the density, $\chi$ is the thermal diffusivity, and $v_0$ is the characteristic velocity.

The set of dimensionless equations describing the thermal hydrodynamics of the fluid with variable viscosity has the form

$$\frac{\partial u}{\partial x} + \frac{\partial v}{\partial y} = 0,$$

$$\frac{\partial u}{\partial t} + \frac{\partial u^2}{\partial x} + \frac{\partial}{\partial y}\left(uv - \frac{1 + A\nu(T)}{\mathrm{Re}}\frac{\partial u}{\partial y}\right) = -\frac{\partial p}{\partial x} + O(\varepsilon^2),$$

$$\frac{\partial v}{\partial t} + \frac{\partial (uv)}{\partial x} + \frac{\partial}{\partial y}\left(v^2 - \frac{1 + A\nu(T)}{\mathrm{Re}}\frac{\partial v}{\partial y}\right) = -\varepsilon^{-2}\frac{\partial p}{\partial y}$$

$$+ \frac{A\nu'(T)}{\mathrm{Re}}\left[\frac{\partial T}{\partial x}\frac{\partial u}{\partial y} + \frac{\partial T}{\partial y}\frac{\partial v}{\partial y}\right] + O(\varepsilon^2),$$

$$\frac{\partial T}{\partial t} + \frac{\partial (uT)}{\partial x} + \frac{\partial}{\partial y}\left(vT - \frac{1}{\mathrm{Pe}}\frac{\partial T}{\partial y}\right) = 0 + O(\varepsilon^2),$$

where bars over dimensionless variables are omitted. This set was solved numerically by using the control volume approach and the semi-implicit method for pressure-linked equations (SIMPLE) [8], where the latter was modified to take into account variable viscosity.

Numerical simulation of the process under investigation was performed under the assumption that heat-exchange intensity on the channel walls was high enough to reduce the boundary condition to equality of the near-wall fluid temperature to the wall temperature. The temperature range between the fluid temperature at the channel entry and the wall temperature covers the entire temperature range of viscosity variation. Calculations were performed with the following dimensionless parameters:

$$\varepsilon = 0.01, A = 100, B = 0.01, \mathrm{Re} = 1, \mathrm{Pe} = 10.$$

Figure 2a shows both viscosity distribution forming a surface and contours of the temperature field in the channel. The temperature field is typical for the case of convective heat transfer. Following the temperature field distribution, fluid viscosity values form a non-monotonic-variation region that is convex in the flow direction and represents a viscous barrier. The sections of the viscosity-variation surface by the mutually perpendicular planes $x = 0.25$ and $y = 0.5$ are shown for clarity. The data presented here correspond to the pressure drop fitted so that the viscous barrier lies entirely within the channel length.

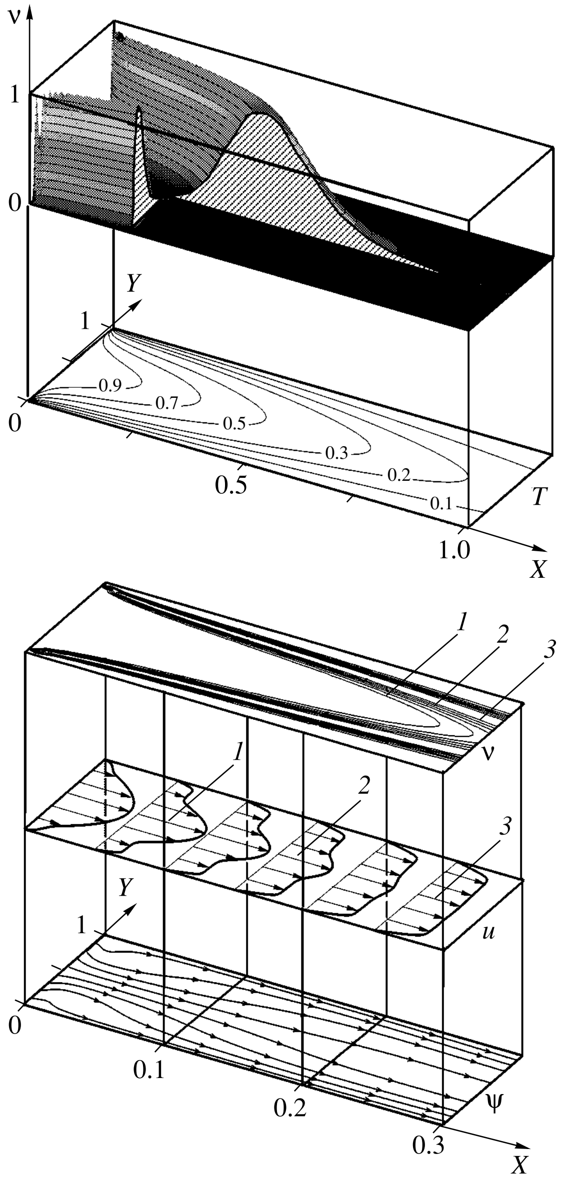

**Fig. 2.** (a, from top to bottom) Dimensionless viscosity distribution, where the viscous barrier is seen, and temperature contours in the channel and (b, from top to bottom) viscosity contours for (*1*) 0.2, (*2*) 0.5, and (*3*) 0.8; the distributions of the longitudinal velocity with their maxima equal to (*1*) 0.70, (*2*) 0.57, and (*3*) 0.45 for various channel cross sections; and streamlines in the channel region containing the interior of the viscous barrier.

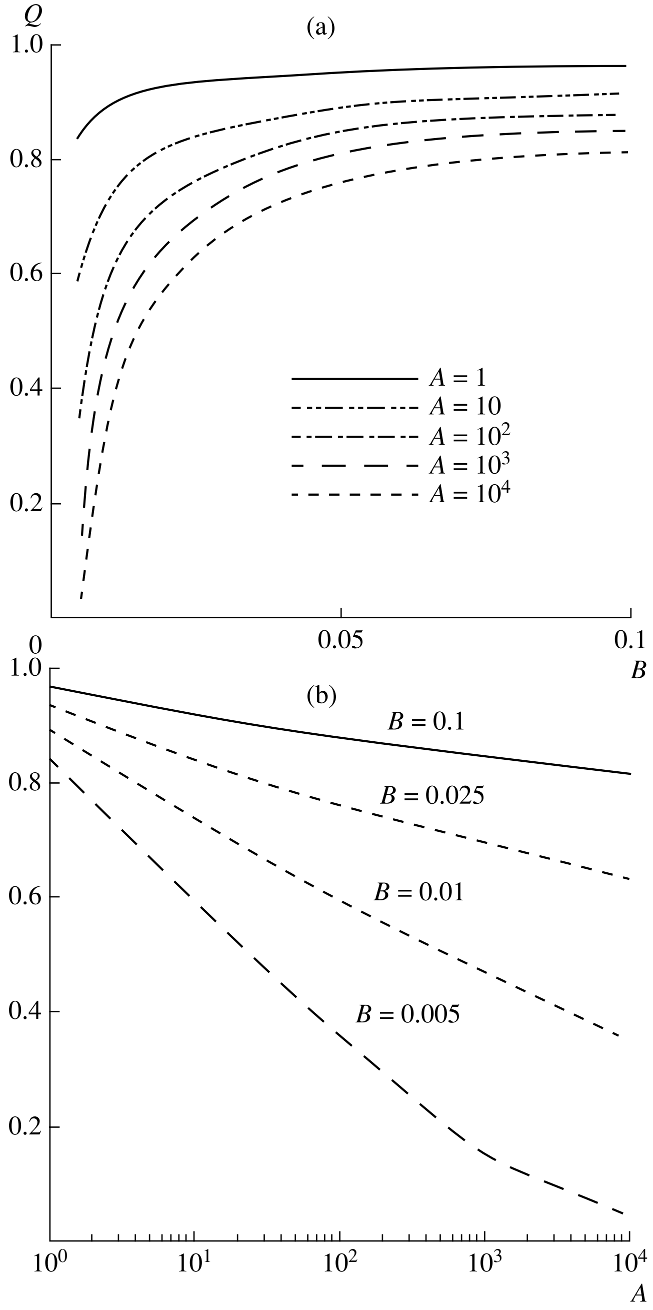

**Fig. 3.** Reduced flow rate of the anomalously viscous fluid vs. the anomaly parameters.

Figure 2 shows (from top to bottom) viscosity contours, longitudinal-velocity distributions, and streamlines in the region of their maximum variation in the interior of the viscous barrier. The stream function $\psi$ is defined according to the relations

$$u = \frac{\partial\psi}{\partial x}, \quad v = -\frac{\partial\psi}{\partial y}.$$

The longitudinal-velocity distributions testify to an intricate flow character, which differs noticeably from the Poiseuille law. A jetlike flow is first formed with the characteristic increase in the longitudinal velocity in the channel center. However, the longitudinal velocity is almost constant in the regions, where viscosity varies strongly, that are adjacent to the central zone. Downstream, these regions expand, the central zone contracts, and the longitudinal-velocity distribution becomes uniform everywhere except the boundary layer. We note that, outside the viscous-barrier region, the longitudinal-velocity profile gradually becomes close to a parabolic profile typical for the Poiseuille flow. Analysis of the streamlines of the flow pattern reveals the existence of the transverse velocity component in the interior of the viscous barrier.

Rate is the basic characteristic of a fluid flow in a channel. Below, we consider the effect of the anomalous-viscosity parameters on the reduced flow rate

$$Q = \frac{1}{Q_0}\int_0^1 u\,dy,$$

where $Q_0$ is the dimensionless flow rate for the Poiseuille flow with constant viscosity $\nu_0$. We note that the longitudinal velocity component $u$ used to calculate the flow rate is also dimensionless.

Our numerical calculations show that the reduced flow rate depends strongly on the parameters $A$ and $B$, which quantitatively characterize the chosen form of the nonmonotonic temperature dependence of viscosity. Physically corresponding to the contraction of the anomalous-viscosity region in the fixed temperature interval, an increase in $B$ leads to a monotonic increase in the reduced flow rate, which is limited by its value at vanishingly small viscosity anomaly (Fig. 3a). At the same time, an increase in the maximum value of viscosity, which is characterized by the parameter $A$, decreases the reduced flow rate according to the lines plotted in Fig. 3b in the semilogarithmic scale for various $B$ values. We note that, for $B > 0.025$, change in $A$ by an order of magnitude only slightly changes the flow rate, while the flow rate may change by a factor of 2 in the range $0 < B \leq 0.025$.

The dependence of the flow rate on the pressure drop is the most important characteristic for applications. It is shown in Fig. 4 for various $A$ values. The curves show that the reduced flow rate for anomalously viscous fluids decreases with an increase in the pressure drop. Here, the solid horizontal straight line corresponds to the linear dependence of the flow rate on the pressure drop for a fluid with constant viscosity.

A decrease in the flow rate with an increase in the pressure drop is attributed to the expansion of the anomalous-viscosity region due to convective transport. The value of the flow-rate decrease depends on the viscosity maximum and is virtually proportional to $\log A$. In addition, with increasing $A$, minima in the flow-rate curves shift to larger pressure drops (Fig. 4).

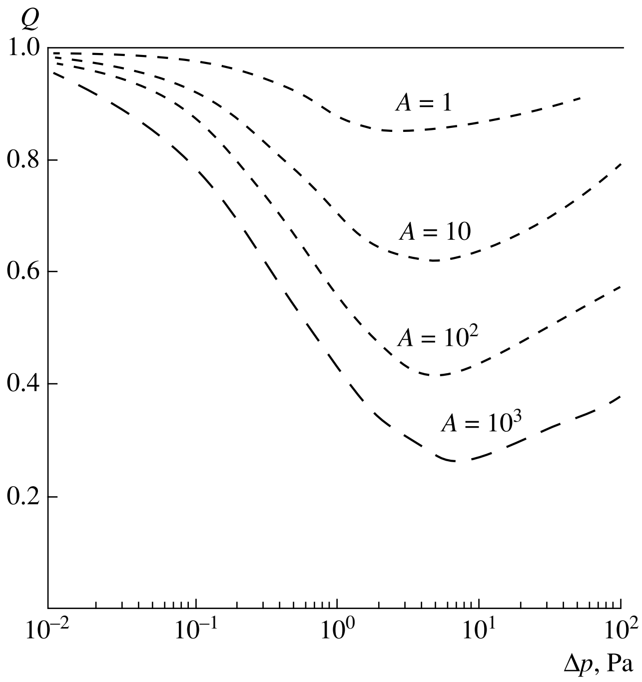

**Fig. 4.** Reduced flow rate of the anomalously viscous fluid vs. the pressure drop for $B = 0.01$ and various $A$ values.

After reaching its minimum, the flow rate increases with increasing pressure drop. This effect is caused by the formation of two open regions of anomalous viscosity, which are adjacent to the channel walls and do not traverse its cross section within the channel.

Our investigation of a flow of a model fluid, whose viscosity is a nonmonotonic function of temperature, reveals a variety of possible hydrodynamic effects. As is established above, the basic feature of the thermal hydrodynamics of anomalously viscous media is the formation of the spatially localized viscous barrier, which can noticeably affect the flow pattern. It is of interest that there is a parameter-space region where an increase in the pressure drop decreases the reduced flow rate.

## ACKNOWLEDGMENTS

This work was supported by the Russian Foundation for Basic Research (project no. 02-01-97907) and by the Program of Fundamental Investigations “Dynamics and Acoustics of Nonuniform Fluids, Gas-Fluid Systems, and Suspensions,” Division of Power Engineering, Mechanical Engineering, Mechanics, and Control Processes, Russian Academy of Sciences.

## REFERENCES

1. L. S. Leĭbenzon, Azerb. Neft. Khoz., No. 2 (3), 59 (1922).
2. J. R. A. Pearson, Y. T. Shan, and E. S. A. Vieira, Chem. Eng. Sci. **28**, 2087 (1973).
3. S. N. Aristov, Dokl. Akad. Nauk **359**, 625 (1998) [Phys. Dokl. **43**, 241 (1998)].
4. S. N. Aristov and V. G. Zelenina, Izv. Ross. Akad. Nauk, Mekh. Zhidk. Gaza, No. 2, 75 (2000).
5. R. E. Bacon and R. Fanelli, J. Am. Chem. Soc. **65**, 639 (1943).
6. V. M. Lekae and L. N. Elkin, *Physicochemical and Thermodynamic Constants of Elementary Sulfur* (Mendeleev Univ. Khim. Tekhnol., Moscow, 1964).
7. S. F. Urmancheev, V. N. Kireev, S. I. Larionov, *et al.*, in *Proceedings of the 3rd International Conference on Multiphase Flow, Lyon, 1998*, Pap. 375.
8. S. Patankar, *Numeral Heat Transfer and Fluid Flow* (McGraw-Hill, New York, 1980; Énergoatomizdat, Moscow, 1984).

*Translated by Yu. Verevochkin*

*Doklady Physics, Vol. 49, No. 5, 2004, pp. 332–335. Translated from Doklady Akademii Nauk, Vol. 396, No. 3, 2004, pp. 339–342.*
*Original Russian Text Copyright © 2004 by Agafonov, Georgievskiĭ.*

**MECHANICS**

# Dynamic Stability of a Beam That Has Nonlinear Internal Viscosity and Is Subjected to a Follower Force

**S. A. Agafonov* and D. V. Georgievskiĭ****

Presented by Academician D.M. Klimov December 29, 2003

Received December 20, 2003

The nonconservative stability of elastic and inelastic bodies and construction elements is a section of both the mechanics of a deformable solid and theory of stability that has attracted attention for the entire last century [1–3]. At present, the development of both computational methods and computer power provides the possibility of finer analysis and discovery of new qualitative effects in the behavior of systems subjected to nonconservative loads. This work is devoted to the stability of a beam with non-Voigt (cubic) internal viscosity. The critical load is compared with the known values in an elastic system and a system that is linearly viscoelastic in the Voigt sense.

**1.** We consider a homogeneous viscoelastic beam with length $l$ and constant cross section $\sigma$. The beam is rigidly fixed at one end and is subjected to a constant follower force $P$ at the other end (Fig. 1). The governing relation of the beam material

$$\sigma = E\varepsilon + k_1\varepsilon^2\dot{\varepsilon} + k_2\dot{\varepsilon}^3 \tag{1}$$

presents the parallel connection of an elastic element with the elastic modulus $E$ and a nonlinear viscous element with the viscosity coefficients $k_1 > 0$ and $k_2 > 0$. The model specified by Eq. (1) can be called an elastic model with non-Voigt viscosity. It is worth noting that the standard Voigt body

$$\sigma = E\varepsilon + k\dot{\varepsilon} \tag{2}$$

is not a particular case of Eq. (1).

Let us derive the equation of vibrations of the beam with governing relation (1). Substituting the kinematic equalities $\varepsilon = -yv_{xx}(x, t)$ and $\dot{\varepsilon} = -y\dot{v}_{xx}(x, t)$ into Eq. (1) and, then, Eq. (1) into the bending-moment expression $M(x, t) = \int\limits_{\Sigma} y\sigma\, d\Sigma$, where integration is carried out over the beam cross section $\Sigma$ (Fig. 2), we obtain the following relation between the moment and deflection $v$:

$$M = -EIv_{xx} - k_1Jv_{xx}^2\dot{v}_{xx} - k_2J\dot{v}_{xx}^3, \tag{3}$$

where

$$I = \int\limits_{\Sigma} y^2 d\Sigma, \quad J = \int\limits_{\Sigma} y^4 d\Sigma.$$

The classical equation $M_{xx} = Pv_{xx} + m\ddot{v}$ of vibrations in the theory of beams, where $m$ is the linear density of the beam, takes the form

$$\begin{gathered} EIv_{xxxx} + k_1J(v_{xx}^2\dot{v}_{xx})_{xx} + k_2J(\dot{v}_{xx}^3)_{xx} \\ + Pv_{xx} + m\ddot{v} = 0. \end{gathered} \tag{4}$$

The boundary conditions

$$\begin{aligned} x = 0&: \quad v = 0, \quad v_x = 0; \\ x = l&: \quad M = 0, \quad M_x = 0 \end{aligned} \tag{5}$$

correspond to the rigid fixation and action of the follower force.

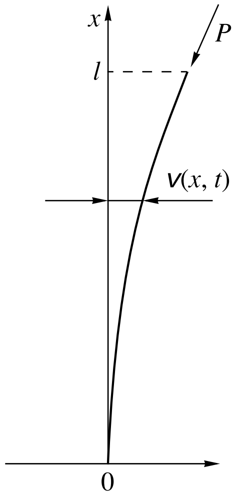

**Fig. 1.**

---

* *Bauman State Technical University, Vtoraya Baumanskaya ul. 5, Moscow, 107005 Russia*

** *Moscow State University, Vorob'evy gory, Moscow, 119992 Russia*
*e-mail: georgiev@mech.math.msu.su*

1028-3358/04/4905-0332$26.00 © 2004 MAIK "Nauka/Interperiodica"

Let us reduce the problem specified by Eqs. (4) and (5) to the dimensionless form in terms of three quantities $EI$, $l$, and $m$. All relations below are given in the dimensionless form, and the notation of the dimensionless variables coincides with the notation of the respective dimensional variables. Deflection $v(x, t)$ satisfies the nonlinear partial differential equation

$$v_{xxxx} + a_1(v_{xx}^2 v_{xxt})_{xx} + a_2(v_{xxt}^3)_{xx} + p v_{xx} + v_{tt} = 0, \tag{6}$$

where

$$a_1 = \frac{k_1 J}{l^4\sqrt{EIm}}, \quad a_2 = \frac{k_2 J\sqrt{EI}}{l^2\sqrt{m^3}}, \quad p = \frac{Pl^2}{EI}$$

with the four boundary conditions specified by Eqs. (5).

Let us substitute Eq. (3) for the binding moment into boundary conditions (5) and note that the conditions

$$\begin{aligned} x = 0&: \quad v = v_x = 0; \\ x = 1&: \quad v_{xx} = v_{xxx} = 0 \end{aligned} \tag{7}$$

are sufficient for boundary conditions (5) to be satisfied if the initial values of the functions $v_{xx}(1, t)$ and $v_{xxx}(1, t)$ are zero.

Thus, we have formulated a boundary value problem that is specified by Eqs. (6) and (7) and describes vibrations of a beam made of the material with governing relation (1) near the equilibrium position $v(x, t) \equiv 0$. This problem involves only three parameters: $p$, $a_1$, and $a_2$.

Equation (6) with $a_1 = a_2 = 0$ corresponds to the classical problem of small vibrations of an elastic beam that has a constant bending rigidity, is fixed at one end, and is subjected to the follower force at the other end. For loads in the range $0 < p \lesssim 20.05$, a vibrational mode with a constant amplitude is realized. The critical value $p_0^* \approx 20.05$ obtained in [4] corresponds to the vibrational instability (flatter) of the rectilinear equilibrium. A quite smaller value, $p_0^* \approx 19.77$, was presented for a similar system in [5]. Theoretically, the $p_0^*$ value is equal to the least positive root of the equation $\tan\sqrt{x} = \sqrt{x}$, i.e., $p_0^* \approx 20.19$ [6].

We point out works [6, 7] (see also [2]) devoted to the effect of the mass distribution over the length of the elastic beam on the $p_0^*$ value. Some mass is concentrated at the point $x = 1$, and the remaining mass is uniformly distributed over the length. The limiting case of the massless beam with the pointlike mass at the end is called a Beck post.

In the presence of internal friction in the linear Voigt model given by Eq. (2), the critical load depends on the viscosity coefficient $k$. When viscosity is negligibly low, we have $\lim\limits_{k \to 0} p^*(k) \equiv p_1^* \approx 10.94$ [8], which is almost half the $p_0^*$ value. As well as for the case of a finite number of degrees of freedom, the introduction of small linear dissipation into the elastic system reduces the stability limit by a finite value. This phenomenon is well known in dynamic stability as the Ziegler paradox. We omit the causes and explanation of this paradox and refer to the detailed review of these problems in [9].

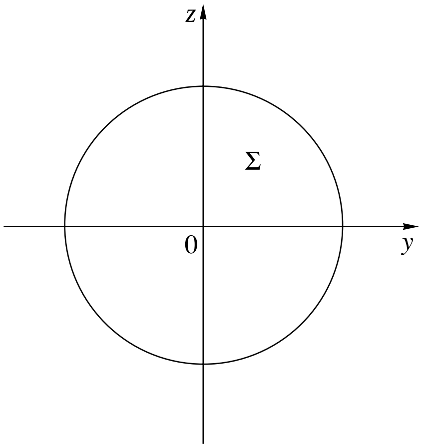

**Fig. 2.**

In [10], the Ziegler pendulum with nonlinear friction in hinges given by $F = ax^2\dot{x} + b\dot{x}^3$ was considered. Stability is analyzed by constructing the Lyapunov function. It was shown that the destabilization effect holds for a nonlinear friction law.

The destabilization of a beam loaded by a force following the tangent to the axis with advance or lag (quasi-follower force) by low internal and external frictions was considered in [11]. Criteria and certain mathematical aspects of the stability of a cantilever beam with an arbitrary linear viscoelastic law were developed in [12]. The optimization of masses for reducing an undesirable jump of the critical force was analyzed in [13].

This paper is primarily focused on the following problems.

(i) How does the critical force $p^*(a_1, a_2)$ depend on the two governing parameters $a_1$ and $a_2$;

(ii) Is a jump in $p^*$ observed in the system under investigation for negligibly low nonlinear viscosity ($a_1 \to 0$ and $a_2 \to 0$) as compared to the values $p_0^*$ and $p_1^*$ in the elastic and Voigt models, respectively.

**2.** We seek a solution of the problem given by Eqs. (6) and (7) in the form of the Fourier series

$$v(x, t) = \sum_{k=1}^{\infty} u_k(t) z_k(x). \tag{8}$$

The functions $z_k(x)$ are the solutions of the boundary value problem

$$\frac{d^4 z_k}{dx^4} - \lambda_k^2 z_k = 0, \quad z_k(0) = \frac{dz_k}{dx}(0) = 0,$$

$$\frac{d^2 z_k}{dx^2}(1) = \frac{d^3 z_k}{dx^3}(1) = 0$$

and have the form

$$z_k(x) = \gamma_k(\cos\delta_k x - \cosh\delta_k x) + \sinh\delta_k x - \sin\delta_k x,$$

$$\gamma_k = \frac{\sin\delta_k + \sinh\delta_k}{\cos\delta_k + \cosh\delta_k},$$

where $\delta_k$ are the roots of the equation

$$\cosh\delta_k \cos\delta_k = -1, \quad k = 1, 2, \ldots. \tag{9}$$

The first two roots of this equation are $\delta_1 \approx 1.875$ and $\delta_2 \approx 4.694$ and, therefore, $\gamma_1 \approx 1.362$ and $\gamma_2 \approx 0.982$.

The functions $z_k(x)$ are mutually orthogonal in the interval [0, 1]:

$$\int_0^1 z_i(x) z_k(x) dx = 0, \quad i \neq k. \tag{10}$$

Substituting Eq. (8) into Eq. (6), multiplying by $z_i(x)$, integrating from 0 to 1, and taking condition (10) into account, we arrive at a countable set of ordinary differential equations. We restrict our consideration to the following set of two equations for $u_1(t)$ and $u_2(t)$:

$$\begin{gathered}
\ddot{u}_1 + \delta_1^4 u_1 + p(e_{11}u_1 + e_{12}u_2) + 3a_1\alpha_1 u_1^2 \dot{u}_1 \\
+ 3a_1\alpha_2 u_2^2 \dot{u}_2 + 2a_1\alpha_3 u_1 u_2 \dot{u}_2 + 2a_1\alpha_4 u_1 u_2 \dot{u}_1 \\
+ a_1\alpha_3 u_2^2 \dot{u}_1 + a_1\alpha_4 u_1^2 \dot{u}_2 + 3a_2\alpha_1 \dot{u}_1^3 + 3a_2\alpha_2 \dot{u}_2^3 \\
+ 3a_2\alpha_3 \dot{u}_1 \dot{u}_2^2 + 3a_2\alpha_4 \dot{u}_2 \dot{u}_1^2 = 0, \\
\ddot{u}_2 + \delta_2^4 u_2 + p(e_{21}u_1 + e_{22}u_2) + 3a_1\beta_1 u_1^2 \dot{u}_1 \\
+ 3a_1\beta_2 u_2^2 \dot{u}_2 + 2a_1\beta_3 u_1 u_2 \dot{u}_2 + 2a_1\beta_4 u_1 u_2 \dot{u}_1 \\
+ a_1\beta_3 u_2^2 \dot{u}_1 + a_1\beta_4 u_1^2 \dot{u}_2 + 3a_2\beta_1 \dot{u}_1^3 + 3a_2\beta_2 \dot{u}_2^3 \\
+ 3a_2\beta_3 \dot{u}_1 \dot{u}_2^2 + 3a_2\beta_4 \dot{u}_2 \dot{u}_1^2 = 0,
\end{gathered} \tag{11}$$

where

$$e_{11} = \frac{1}{\kappa_1}\int_0^1 z_1'' z_1 dx, \quad e_{12} = \frac{1}{\kappa_1}\int_0^1 z_2'' z_1 dx,$$

$$e_{21} = \frac{1}{\kappa_2}\int_0^1 z_1'' z_2 dx, \quad e_{22} = \frac{1}{\kappa_2}\int_0^1 z_2'' z_2 dx, \tag{12}$$

$$\kappa_1 = \int_0^1 z_1^2 dx, \quad \kappa_2 = \int_0^1 z_2^2 dx.$$

Formulas (12) yield $e_{11} \approx 0.858$, $e_{12} \approx -8.464$, $e_{21} \approx 2.599$, and $e_{22} \approx -13.294$. The coefficients $\alpha_1 \approx 222.022$, $\alpha_2 \approx 2273.73$, $\alpha_3 \approx 7430.31$, $\alpha_4 \approx 1286.77$, $\beta_1 \approx 825.596$, $\beta_2 \approx 134887$, $\beta_3 \approx 13129.6$, and $\beta_4 \approx 14302$ appearing in set (11) are calculated by integrating expressions depending on the eigenfunctions $\{z_k(x)\}$ and their derivatives in the interval [0, 1].

For $0 < p < 20.19$, the characteristic equation of the linear part of set (11) has two pairs of imaginary roots $\pm i\omega_1$ and $\pm i\omega_2$, where $i^2 = -1$ and $\omega_1$ and $\omega_2$ satisfy the frequency equation ($\omega_2 > \omega_1$)

$$\begin{gathered}
\omega^4 = (\delta_1^4 + \delta_2^4 + pe_{11} + pe_{22})\omega^2 \\
+ (\delta_1^4 + pe_{11})(\delta_2^4 + pe_{22}) - p^2 e_{12} e_{21} = 0.
\end{gathered} \tag{13}$$

Thus, the problem of the stability of the zeroth equation of set (11) for $0 < p < 20.19$ is reduced to analysis of the critical case of two pairs of imaginary roots.

**3.** To use the Kamenkov criterion [14], it is necessary to perform the linear and nonlinear normalization of set (11) up to the third-order terms inclusively. The linear transformation

$$\begin{gathered}
u_1 = \frac{1}{2}[y_1 + \bar{y}_1 + \delta_{12}(y_2 + \bar{y}_2)], \\
u_2 = \frac{1}{2}[\delta_{21}(y_1 + \bar{y}_1) + y_2 + \bar{y}_2], \\
\dot{u}_1 = \frac{i}{2}[\omega_1(y_1 - \bar{y}_1) + \delta_{12}\omega_2(y_2 - \bar{y}_2)], \\
\dot{u}_2 = \frac{i}{2}[\delta_{21}\omega_1(y_1 - \bar{y}_1) + \omega_2(y_2 - \bar{y}_2)],
\end{gathered} \tag{14}$$

where the bar stands for complex conjugation,

$$\delta_{12} = \frac{pe_{12}}{\omega_2^2 - \delta_1^4 - pe_{11}}, \quad \delta_{21} = \frac{pe_{21}}{\omega_1^2 - \delta_2^4 - pe_{22}}$$

reduces set (11) to the form

$$\begin{aligned}
\dot{y}_1 &= i\omega_1 y_1 + Y_1(y_1, \bar{y}_1, y_2, \bar{y}_2), \\
\dot{y}_2 &= i\omega_2 y_2 + Y_2(y_1, \bar{y}_1, y_2, \bar{y}_2).
\end{aligned} \tag{15}$$

Here, $Y_1$ and $Y_2$ are the set of the third-order terms with respect to $y_1$, $\bar{y}_1$, $y_2$, and $\bar{y}_2$. The equations for the complex conjugate variables $\bar{y}_1$ and $\bar{y}_2$ are not presented in Eqs. (15). Further, set (15) is nonlinearly normalized up to the third-order terms.

In the absence of the internal resonance $\omega_2 \neq 3\omega_1$, the normal form is represented as

$$\begin{aligned} \dot{y}_1 &= i\omega_1 y_1 + a y_1^2 \bar{y}_1 + b y_1 y_2 \bar{y}_2, \\ \dot{y}_2 &= i\omega_2 y_2 + c y_1 \bar{y}_1 y_2 + d y_2^2 \bar{y}_2, \end{aligned} \tag{16}$$

where the old notation of the variables is used. The coefficients $a$, $b$, $c$, and $d$ are expressed as

$$\begin{aligned} a &= -\frac{3}{8}(a_1 + 3a_2\omega_1^2) f_1(p), \\ b &= -\frac{1}{4}(a_1 + 3a_2\omega_2^2) f_2(p), \\ c &= -\frac{1}{4}(a_1 + 3a_2\omega_1^2) f_3(p), \\ d &= -\frac{3}{8}(a_1 + 3a_2\omega_2^2) f_4(p), \end{aligned} \tag{17}$$

where $f_k(p)$, $k = 1$–$4$, are functions of one variable, $p$.

The coefficients $a$, $b$, $c$, and $d$ are negative at $p = 0$. Calculations with the Mathematica 5 package show that $a$ is negative and positive for $p \in (0, 11.19)$ and $(11.19, 20.19)$, respectively.

According to the Kamenkov criterion [14], set (15) is asymptotically stable for $p \in [0, 11.19)$. This conclusion is also valid for original set (11) [15]. The internal resonance $\omega_2 = 3\omega_1$ corresponds to the value $p \approx 12.298$, which is obtained from frequency equation (13). Set (11) is unstable for $p \in (11.19, 20.19)$ except perhaps the value $p \in 12.298$, because the coefficient $a$ is positive for these $p$ values [15].

Thus, the effect of stability loss takes place in the presence of nonlinear viscosity (1). The critical value $p^*$ for a nonlinear viscosity law is quite larger than that in Voigt model (2). In addition, the effect of a decrease in the critical load in the Voigt model is observed for low viscosity, whereas this effect in the nonlinear model is manifested for any coefficients $a_1 > 0$ and $a_2 > 0$.

## ACKNOWLEDGMENTS

This work was supported by the NATO Science Fellowship and Russian Foundation for Basic Research, project no. 02-01-00780.

## REFERENCES

1. V. V. Bolotin, *Nonconservative Problems in the Theory of Elastic Stability* (Fizmatgiz, Moscow, 1961; Pergamon, London, 1965).
2. A. P. Filin, *Applied Mechanics of Deformable Solids* (Nauka, Moscow, 1981), Vol. 3.
3. N. Kh. Arutyunyan, A. D. Drozdov, and V. B. Kolmanovskiĭ, Itogi Nauki Tekh., Ser.: Mekh. Deform. Tverd. Tela **19**, 3 (1987).
4. M. Beck, Z. Angew. Math. Mech. **3**, 225 (1952).
5. K. S. Deĭneko and M. Ya. Leonov, Prikl. Mat. Mekh. **19**, 738 (1955).
6. G. Yu. Dzhanelidze, Tr. Lenigr. Politekh. Inst., No. 192, 21 (1958).
7. A. Pflüger, Z. Angew. Math. Mech. **35**, 191 (1955).
8. V. V. Bolotin and N. I. Zhinzher, Int. J. Solids Struct. **5**, 965 (1969).
9. A. P. Seĭranyan, Usp. Mekh. **13** (2), 89 (1990).
10. P. Hagedorn, Int. J. Non-Linear Mech. **5**, 341 (1970).
11. G. G. Denisov and V. V. Novikov, Izv. Akad. Nauk SSSR, Mekh. Tverd. Tela, No. 1, 150 (1975).
12. I. I. Voloshin and V. G. Gromov, Izv. Akad. Nauk SSSR, Mekh. Tverd. Tela, No. 4, 179 (1976).
13. D. V. Georgievskiĭ, in *Numerical Analysis, Mathematical Modeling, and Their Application in Mechanics* (Mosk. Gos. Univ., Moscow, 1988), pp. 31–35.
14. G. V. Kamenkov, *Selected Works*, Vol. 1: *Stability of Motion, Oscillations, Aerodynamics* (Nauka, Moscow, 1971).
15. L. G. Khazin and É. É. Shnol’, *Stability of Critical Equilibrium Positions* (Tsentr Biol. Issled. AN SSSR, Pushchino, 1985).

*Translated by R. Tyapaev*

*Doklady Physics, Vol. 49, No. 5, 2004, pp. 336–337. Translated from Doklady Akademii Nauk, Vol. 396, No. 3, 2004, pp. 343–344.*
*Original Russian Text Copyright © 2004 by Badmaev, Shamshev.*

**MECHANICS**

# Generalized Hydrodynamic Model of Penetration

**R. L. Badmaev and Corresponding Member of the RAS K. N. Shamshev**

Received August 11, 2003

The high-velocity penetration of metallic bodies into a solid target is accompanied by both the formation of a complicated state and fracture of materials with the formation of a cavity in the target [1]. The problem of the penetration of bodies with various geometric shapes is not described by a unified analytical solution.

Models establishing the fundamental properties of high-velocity penetration are well known [2–5]. The subsequent models based on the hydrodynamic concept of the penetration of a thin jet with account of the strength effect did not improve the agreement of theory with experimental results.

In this work, a simple generalized formula is proposed for estimating the penetration depth of bodies with various shapes into a massive target. The formula is obtained in the scheme of local interaction between bodies by relating dimensionless values both introduced here and taken from models [2–7]. The effective length of the penetrating body is determined as a function of the parameters of interacting bodies. It is shown that the strength resistance of the medium depends strongly on the shape of the penetrating body.

A local liquid–solid medium is realized near the interface upon high-velocity penetration [8]. On the boundary between plastic and undeformed solid parts of the target, stress can achieve or exceed the ultimate strength, which is the main characteristic of the mechanical properties of the material. The resistance of the medium is taken to be equal to the product of the temporal resistance of the material and an empirical constant.

Calculated and measured penetration depths

| Penetrating body | | | | | Target | | | Penetration depth | | | |
|---|---|---|---|---|---|---|---|---|---|---|---|
| shape | material | $V_p$, km/s | $l_s$, mm | $l_2$, mm | material | $\sigma_t$, GPa | $\mu$ | $L_c$, mm | $L_e$, mm | $\Delta$, % | ref. |
| Thin jet | Steel | 4.65 | 51 | 139 | Steel | 0.42 | 1.0 | 139 | 140 | –0.7 | [9] |
| | | ″ | ″ | 117 | | 1.2 | 1.0 | 117 | 120 | –2.5 | ″ |
| | | ″ | ″ | 135.5 | 2024stAl | 0.48 | 1.0 | 227 | 220 | 3.2 | ″ |
| | | ″ | ″ | 241.4 | Lead | 0.015 | 1.0 | 202 | 210 | –3.8 | ″ |
| | | 1.63 | 162 | 312.8 | Steel | 0.42 | 1.0 | 312.8 | 285 | 9.8 | [10] |
| Sphere | Steel | 1.05 | 9.4 | 27.0 | Lead | 0.015 | 1.0 | 22.4 | 22.5 | –0.4 | [11] |
| | | 2.65 | 9.4 | 36.9 | | 0.015 | 1.0 | 30.5 | 30.9 | –1.3 | ″ |
| | Plastic | 6.6 | 8.0 | 22.0 | 1100-FAl | 0.12 | 1.0 | 14.7 | 14.2 | 3.5 | [12] |
| Rod | Copper | 0.87 | 20 | 19.8 | Aluminum | 0.07 | 100 | 35.8 | 35.5 | 0.8 | [1, 11] |
| | Alloy W-10 | 2.55 | 27.7 | 27.5 | Steel | 1.2 | 100 | 41.2 | 41 | 0.5 | [1, 13] |
| | Alloy X27Wa | 2.25 | 300 | 285 | | 1.2 | 100 | 421.3 | 421 | 0.1 | [14] |
| | Duralumin | 1.64 | 63.5 | 82 | Polyethylene | 0.012 | 100 | 142 | 138 | 2.9 | [15] |
| Planar Jet | Steel | 1.42 | 35.4 | 30 | Steel | 0.42 | 100 | 30 | 29 | 3.4 | [10] |
| | | 1.42 | 70.7 | 60.4 | | 0.42 | 100 | 60.4 | 60 | 0.6 | ″ |

---

*OAO Dolgoprudnyĭ Scientific and Production Enterprise, Dolgoprudnyĭ, Moscow oblast, Russia*

The generalized formula for the penetration depth of bodies with various shapes into the massive target can be written in the form

$$L = l_2\sqrt{\frac{\rho_p}{\rho_t}}, \tag{1}$$

where

$$l_2 = l_p\left(\frac{\rho_p v_p^2}{\sigma}\right)^{\frac{1}{6}} \tag{2}$$

is the effective length of the penetrating body and $\rho_p$ and $\rho_t$ are the densities of the penetrating body and target, respectively. In formula (2), $l_p$ is either the length of the rod or the diameter of the jet source; $v_p$ is the velocity or average velocity of the penetrating body; and

$$\sigma = \mu\sigma_t, \tag{3}$$

is the resistance of the medium, where $\sigma_t$ is the temporal resistance of the material and $\mu$ is a constant.

The characteristics of the interacting bodies are presented in the table, where the results $L_c$ calculated for the cavity depth are compared with its experimental values $L_e$ [9–15]. The data in the table show that the cavity depth $L$ given by Eq. (1), effective length $l_2$ specified by Eq. (2), and constant $\mu$ in Eq. (3) depend only on the impact conditions. It is worth noting that dissipative phenomena disregarded here do not noticeably affect the quantitative estimate of the final result of penetration.

## CONCLUSIONS

Thus, a unified formula based on the determination of the effective length of the penetrating body and the resistance of the medium is proposed for the penetration depth of bodies with various shapes into targets, including steel targets, for impact velocities above 1 km/s.

## REFERENCES

1. *High Velocity Interaction of Solids*, Ed. by V. M. Fomin (Izd. SO RAN, Novosibirsk, 1999).
2. G. Birkhoff, D. P. MacDougall, E. M. Pugh, and S. G. Taylor, J. Appl. Phys. **19**, 563 (1948).
3. M. A. Lavrent'ev, Usp. Mat. Nauk **12** (4), 41 (1957).
4. F. F. Vitman and N. A. Zlatin, Dokl. Akad. Nauk SSSR **146**, 337 (1962) [Sov. Phys. Dokl. **7**, 838 (1962)].
5. A. Ya. Sagomonyan, Dokl. Akad. Nauk SSSR **156**, 1053 (1964) [Sov. Phys. Dokl. **9**, 449 (1964)].
6. W. Herrmann and J. S. Wilbeck, Int. J. Impact Eng. **5**, 307 (1987).
7. A. S. Balankin, A. A. Lyubomudrov, and I. T. Sevryukov, *Kinetic Theory of Cumulative Armor Piercing* (Izd. Minoborony, Moscow, 1989), pp. 255–259.
8. M. A. Lavrent'ev, Prikl. Mekh. Tekh. Fiz. **41** (5), 3 (2000).
9. R. J. Eichelberger, J. Appl. Phys. **27**, 63 (1956).
10. *Physics of Explosion*, Ed. by L. P. Orlenko (Fizmatgiz, Moscow, 2002), Vol. 2.
11. *Ballistic Installations and Their Application for Experimental Studies*, Ed. by N. A. Zlatin and G. I. Mishin (Nauka, Moscow, 1974).
12. J. Gering, in *High Velocity Impact Phenomena*, Ed. by V. N. R. Kinslow (Academic, New York, 1971; Mir, Moscow, 1973), pp. 469–515.
13. P. M. Holland, J. T. Gordon, T. L. Menna, and A. C. Charters, Int. J. Impact Eng. **10**, 241 (1990).
14. B. R. Sorensen, K. D. Kimsey, G. F. Silsby, *et al.*, Int. J. Impact Eng. **11**, 107 (1991).
15. A. Tate, J. Mech. Phys. Solids **15**, 387 (1967).

*Translated by R. Badmaev*

*Doklady Physics, Vol. 49, No. 5, 2004, pp. 338–341. Translated from Doklady Akademii Nauk, Vol. 396, No. 3, 2004, pp. 345–348.*
*Original Russian Text Copyright © 2004 by Bratov, Gruzdkov, Krivosheev, Petrov.*

**MECHANICS**

# Energy Balance in the Crack Growth Initiation under Pulsed-Load Conditions

**V. A. Bratov, A. A. Gruzdkov, S. I. Krivosheev, and Yu. V. Petrov***

Presented by Academician N.F. Morozov November 17, 2003

Received December 5, 2003

## 1. ENERGY APPROACH TO THE FRACTURE PROBLEM

The classical approach to fracture mechanics going back to Griffith is based on the statement that a crack propagates if this process leads to a decrease in the total energy $\varepsilon$ of a system. For a plate of unit thickness, the crack-growth conditions can be written as

$$-\frac{\partial\varepsilon}{\partial L} = 2\gamma. \qquad (1)$$

Griffith initially interpreted the quantity $2\gamma$ as the surface energy, because it represented the specific work (per unit area) expended to form a new surface. Irwin and Orowan showed that this quantity should be interpreted as the total work (including the plastic one) in the fracture zone. This work can be taken as the resistance to a certain dissipative process proceeding in a small region near the crack tip. The study of this characteristic includes the determination of its physical origin (different for different classes of materials) and its measurement.

For the fracture near the crack tip loaded by mode I, criterion (1) is equivalent to the criterion for the critical stress-intensity factor $K_I \le K_{Ic}$. For a linearly elastic body, the Griffith constant is equal to

$$\gamma = \frac{K_{Ic}^2}{2E}, \qquad (2)$$

where $E$ is Young's modulus. Thus, $\gamma$ can be indirectly determined in this case from the standard tests for measuring $K_{Ic}$.

Nowadays, it is generally recognized [1] that the expenditure energy per unit area of a fracture surface essentially depends on the action duration. Other characteristics of dynamic fracture (critical intensity factor, limiting amplitude of applied load) also essentially depend on time. Therefore, the problem of determining the Griffith specific surface energy is urgent for high-rate fracture.

## 2. DYNAMIC TESTS

It is impossible to adequately study the energy balance by conventional methods of creating short-term loads, because it is very difficult to estimate the energy fraction directly transferred to a specimen. In particular, the parameters of explosive or shock action can be estimated only approximately. For most cases, energy exchange between the specimen and a loading device is rather complicated [2], which makes it impossible to authentically determine the stage at which fracture occurs.

The procedure using a magnetic pulse installation is free of the above disadvantage. Load is formed by the magnetic-pulse method, where the mechanical pressure depends on the spatial configuration of current-carrying elements [3–5]. For a known current distribution, the current-pulse parameters are unambiguously related to magnetic pressure. In addition, the energy state of the specimen at the instant of fracture can be determined quite exactly in many cases. This determination is possible for the following reasons. First, the pressure on cut edges is monitored throughout the pulse (about 1–10 μs). Second, high-speed shooting of the fracture process makes it possible to precisely determine the instant at which cracks start. In certain cases, it can occur after the disappearance (removal) of the external pressure pulse. Third, after the termination of the pulse action, the specimen does not interact with the installation; hence, the specimen under fracture becomes an energetically closed system.

The indicated principles were realized in the run of tests for specimens with a cut modeling a macrocrack. The specimens were manufactured from spheroplastics (120 × 120 × 10-mm specimens with a 60 × 2.2-mm cut) [3] and polymethyl methacrylate (200 × 200 × 10-mm specimens with a 100 × 3-mm cut) [4, 5]. At the cut tips, we made a 0.2-mm-thick notch 3 mm in length.

---

*St. Petersburg State University,*
*Bibliotechnaya pl. 2, St. Petersburg, 198504 Russia*
** e-mail: yp@yp1004.spb.edu*

1028-3358/04/4905-0338$26.00 © 2004 MAIK "Nauka/Interperiodica"

The cut edges were loaded by uniform pressure approximated by the dependence

$$P(t) = A\sin^2\frac{\pi t}{T}, \quad 0 \le t \le T. \qquad (3)$$

For each pulse duration $T$, the dependence of the crack-growth length on the applied-load amplitude $A$ was studied. We aimed to determine the threshold amplitude. The obtained dependences were well approximated by the linear functions (Fig. 1)

$$\Delta L = k(A - A_0), \quad A > A_0. \qquad (4)$$

The quantity $A_0$ is the threshold amplitude above which the crack begins to grow. This quantity was found by extrapolating the experimental data to the value $\Delta L = 0$.

The high-speed shooting of the fracture process revealed a delay of the onset of crack growth relative to the instant at which the stress-intensity factor reaches its maximum [6]. In this case, the time before the onset of crack growth is appreciably longer than the time of action of the external pressure pulse. Hence, the total energy of the external action is converted to the elastic and kinetic energy of the material, and the crack propagation is further determined by this internal energy. Since the potential of external forces is equal to zero at the instant of fracture near the crack tip, it is possible to consider that the function ε in Eq. (1) coincides with the internal energy of the specimen.

## 3. ENERGY BALANCE

We analytically estimate the energy transferred to the specimen due to interaction with the installation. During the load action, the wave has no time to pass along the cut edges; therefore, in the first approximation, it is possible to consider the problem of a plane wave in a half-space:

$$U_{tt} - c^2 U_{xx} = 0,$$

$$U_x(0, t) = -\frac{P(t)}{c^2\rho}, \quad U(x, 0) = 0, \quad U_t(x, 0) = 0.$$

Here, $x$ and $U$ are the coordinate and the longitudinal displacement, respectively; $c$ is the longitudinal-wave velocity; $t$ is the time; and $\rho$ is the density. Solving the problem with Eq. (3), we derive the expression for the energy transferred to the specimen:

$$\varepsilon = \frac{3DHA^2T}{8c\rho}, \qquad (5)$$

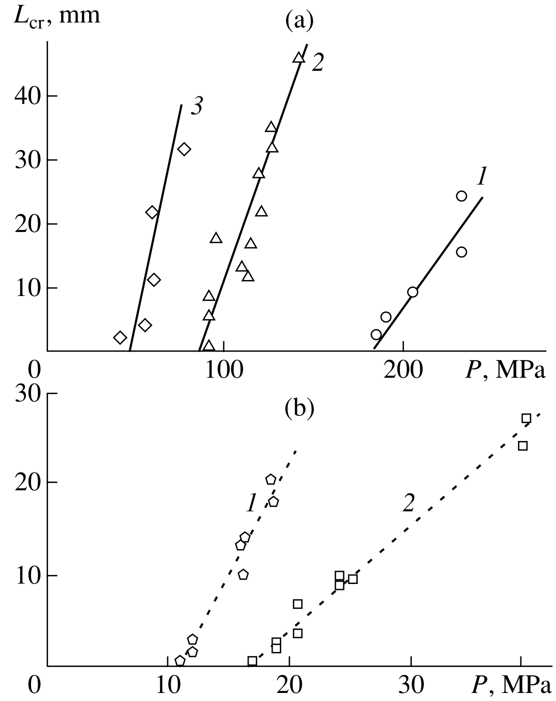

**Fig. 1.** Experimental data on the length $L_{cr}$ of a crack grown from the cut tip vs. the amplitude $P$ of rupturing pressure pulse for (a) polymethyl-methacrylate specimens at the time of a pulse increase to the maximum (*1*) 1, (*2*) 2, and (*3*) 4.6 μs and for (b) spheroplastic specimens at the time of a pulse increase to the maximum (*1*) 4.4 and (*2*) 2.76 μs.

where $D$ is the cut length, $H$ is the plate thickness, and $A$ and $T$ are the parameters of the pressure pulse from Eq. (3).

To prove the correctness of this approach for estimating the energy transferred to a plate during the contact, we numerically analyzed the three-dimensional problem of the interaction of a specimen with a loading device [7]. Using a finite-element software package, we calculated the energy transmitted to the specimen during the contact with the current-carrying bus. For estimating this energy, it suffices to numerically simulate only an early stage of the process, and precisely during the pressure-pulse action from the bus side, and then to estimate the energy involved in the specimen.

As a result, we obtained data on the total energy of the specimen. Thus, similar to analytical calculation, the total energy of the system including its kinetic component is taken into account.

The simulation was carried out for polymethyl methacrylate specimens at three different durations of the action pulse. The table presents the energies transferred to the specimen as calculated by both Eq. (5) and the finite-element method. The good agreement between them supports the applicability of this

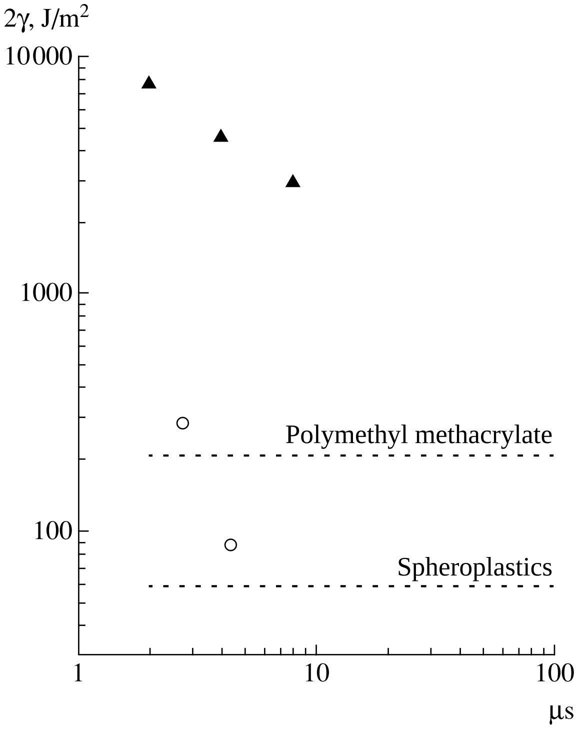

**Fig. 2.** Fracture energy consumption vs. the loading-pulse duration (the dashed lines correspond to quasistatic tests) for (triangles) polymethyl methacrylate and (circles) spheroplastic.

approach for estimating the energy transferred to the specimen during the contact.

## 4. CONDITION OF CRACK GROWTH

From Eq. (4), it follows that the crack-length increment is related to the increment of the amplitude of the applied pulsed pressure as $dL = kdA$. Taking into account Eq. (5) and $dS = HdL$, we obtain the specific (per unit area) energy consumption on fracture at the crack onset

$$\left.\frac{d\varepsilon}{dS}\right|_{\Delta L = 0} = \frac{3TA_0D}{4kc\rho}.$$

If the time of travel of an elastic wave along a cut exceeds the time interval from the loading-application instant to the crack onset, i.e., for sufficiently large specimens, only an effective area $D_* = ct_*$, where $t_*$ is the time before the crack onset, instead of the total cut length, must be taken into account when calculating the fracture energy consumption. In this case, we derive the following relation for the specific energy consumption:

$$\frac{3TA_0t_*}{2k\rho} = 2\gamma_d. \qquad (6)$$

The quantity $\gamma_d$ is an analogue of the quantity $\gamma$ in Eq. (1). Since $c$ and $\rho$ are the known material parameters, and $A_0$, $k$, and $t_*$ are determined experimentally for the pulses of various duration $T$, Eq. (6) yields this quantity as a function of load duration.

**Table**

| $T$, μs | $A$, MPa | Energy, J | |
|---|---|---|---|
| | | by Eq. (5) | finite-element calculation |
| 2 | 172 | 4.17 | 4.00 |
| 4 | 93 | 2.44 | 2.32 |
| 8.6 | 48 | 1.40 | 1.33 |

## 5. DISCUSSION OF THE RESULTS

Figure 2 shows that $\gamma_d$ exceeds the value calculated from Eq. (2) using the results of quasistatic tests by more than an order of magnitude. However, as the load duration increases, this value decreases markedly. For polymethyl methacrylate, the points calculated from Eq. (6) lie on a straight line plotted in logarithmic coordinates; i.e., the relation $\gamma_d T^{\alpha}$ = const is met for microsecond loads.

The results of the finite-element simulation show that the kinetic and potential components of the energy are comparable. Thus, at the action rates realized in the experiments at the magnetic-pulse installation, it is unjustified to neglect the kinetic energy of a material. Moreover, the inclusion of the kinetic energy can qualitatively change the behavior of the fracture energy consumption.

The basic advantage of the applied testing scheme is that there is no energy exchange between a specimen and a loading device after the termination of the pressure-pulse action, and fracture begins to develop after removing load when the specimen becomes energetically closed.

## ACKNOWLEDGMENTS

This work was supported by the Russian Foundation for Basic Research (project nos. 02-01-01035, 03-01-39010, and TsKP 00-01-05020), Swiss Science Foundation, NATO Scientific Affairs Division, and the Russian Federal Program “Integratsiya.”

## REFERENCES

1. N. F. Morozov and Yu. V. Petrov, *Dynamics of Fracture* (Izd. S.-Peterburg. Gos. Univ., St. Petersburg, 1997; Springer-Verlag, Berlin, 2000).

2. Yu. V. Petrov and V. I. Smirnov, *Nonstationary Oscillations and Behavior of Internal Energy of One-Dimensional Solids* (S.-Peterb. Gos. Univ., St. Petersburg, 2002).
3. S. A. Atroshenko, S. I. Krivosheev, Yu. V. Petrov, *et al.*, in *Proceedings of the 3rd International Conference "Kharitonov Topical Lectures"* (VNIIÉF, Sarov, 2001), pp. 131–132.
4. S. I. Krivosheev, N. F. Morozov, Yu. V. Petrov, and G. A. Shneerson, Izv. Akad. Nauk, Mekh. Tverd. Tela **165** (5), 78 (1999).
5. S. I. Krivosheev and G. I. Shneerson, in *Strength and Fracture of Materials and Structures: Collection of Scientific Works* (S.-Peterb. Gos. Univ., St. Petersburg, 1999), No. 18, pp. 116–122.
6. A. N. Berezkin, S. I. Krivosheev, Yu. V. Petrov, and A. A. Utkin, Dokl. Akad. Nauk **375**, 328 (2000) [Dokl. Phys. **45**, 617 (2000)].
7. V. A. Bratov and A. A. Gruzdkov, in *Proceedings of the 17th International Conference of Young Scientists (Gagarin Lectures), Moscow, 2001*, p. 119.

*Translated by V. Bukhanov*

*Doklady Physics, Vol. 49, No. 5, 2004, pp. 342–346. Translated from Doklady Akademii Nauk, Vol. 396, No. 3, 2004, pp. 349–353.*
*Original Russian Text Copyright © 2004 by Manuĭlovich.*

**MECHANICS**

# Transformation of the Instability Wave under an Abrupt Change in the Flexibility of Boundaries

**S. V. Manuĭlovich**

Presented by Academician G.S. Byushgens December 19, 2003

Received December 19, 2003

Methods of laminarization of fluid flows by means of flexible boundaries are still of current interest [1]. In this work, the problem of the structure of perturbed motion near the joint between the rigid and flexible segments of the control panel is analytically solved.

We study nonstationary two-dimensional perturbations of the plane Poiseuille flow. The fluid density, channel half-width, and velocity of the unperturbed flow on its axis are used as the basic units of measurement. The Reynolds number expressed in terms of these parameters is denoted as R.

We use a Cartesian coordinate system with the origin on the channel axis, the $x$ axis along the unperturbed flow, and the $y$ axis perpendicular to walls. The dimensionless time is denoted as $t$. Perturbations of the flow are considered to be small. In this case, the components of perturbed motion with different frequencies $\omega > 0$ can be studied independently.

Perturbations of the components of velocity and pressure are denoted as

$$\varepsilon q(x, y)\exp(-i\omega t) + \text{c.c.} + O(|\varepsilon|^2),$$

where $|\varepsilon| \ll 1$ and $q = u$, $v$, and $p$. The complex amplitudes of the perturbation parameters $q$ satisfy the linearized system

$$\frac{\partial u}{\partial x} + \frac{\partial v}{\partial y} = 0,$$

$$-i\omega u + (1-y^2)\frac{\partial u}{\partial x} - 2yv + \frac{\partial p}{\partial x} = \frac{1}{\mathrm{R}}\left(\frac{\partial^2 u}{\partial x^2} + \frac{\partial^2 u}{\partial y^2}\right), \quad (1)$$

$$-i\omega v + (1-y^2)\frac{\partial v}{\partial x} + \frac{\partial p}{\partial y} = \frac{1}{\mathrm{R}}\left(\frac{\partial^2 v}{\partial x^2} + \frac{\partial^2 v}{\partial y^2}\right).$$

Since the instability wave is an antisymmetric mode, we consider only antisymmetric perturbations satisfying the conditions

$$u(x, 0) = p(x, 0) = 0 \quad (2)$$

on the channel axis. These conditions enable one to formulate the boundary value problem in the band $-\infty < x < +\infty$, $0 \le y \le 1$. It is worth noting that symmetric and antisymmetric perturbations can be investigated independently only for the symmetric unperturbed flow and identical boundary conditions at both ends of the channel. In this connection, we assume that the channel walls have identical flexibilities.

We assume that perturbations of the flow are generated by the instability wave (Tollman–Schlichting wave). These perturbations induce antisymmetric transverse vibrations of the walls with the frequency of the incident wave. The corresponding shape of the upper wall is given by the expression

$$y_w = 1 + [\varepsilon f(x)\exp(-i\omega t) + \text{c.c.}] + O(|\varepsilon|^2), \quad (3)$$

where $f(x)$ is the longitudinal distribution of the complex amplitude of vibrations.

When studying the evolution of perturbations, we use the flexibility law [2] according to which the vibrations of boundaries are induced by pressure pulsations on the wall $p_w = p(x, 1)$ and are described by the equation

$$B\frac{d^4 f}{dx^4} - T\frac{d^2 f}{dx^2} + (K - \omega^2 M - i\omega D)f = p_w, \quad (4)$$

where $K$ is the elasticity, $M$ is the inertia, $D$ is the damping, $T$ is the tension, and $B$ is the bend resistance. The perturbed flow satisfies the no-slip boundary conditions on the wall given by Eq. (3). In the approximation linear in $\varepsilon$, these conditions have the form

$$u(x, 1) = 2f(x), \quad v(x, 1) = -i\omega f(x). \quad (5)$$

If the flexibility of the channel walls is uniform, arbitrary perturbation is represented as superposition of

---

*Zhukovsky Central Institute of Aerohydrodynamics, Zhukovskiĭ, Moscow oblast, 140160 Russia*

1028-3358/04/4905-0342$26.00 © 2004 MAIK “Nauka/Interperiodica”

the eigenfunctions of the problem:

$$q = q_n(y)\exp(i\alpha_n x), \tag{6}$$

where $\alpha_n$ is the complex eigenvalue and $q_n$ is the corresponding eigenfunction. Since the flow is bounded in the transverse direction, the $\{\alpha_n\}$ spectrum is discrete and infinite ($n = 1, 2, \ldots$).

To analyze free perturbations (6), it is convenient to use an auxiliary function $\varphi(y; \alpha)$ that is a solution of the Orr–Sommerfeld equation with the inhomogeneous boundary conditions

$$\left(1-y^2-\frac{\omega}{\alpha}\right)\left(\frac{d^2\varphi}{dy^2}-\alpha^2\varphi\right)+2\varphi = \frac{1}{i\alpha \mathrm{R}}\left(\frac{d^4\varphi}{dy^4}-2\alpha^2\frac{d^2\varphi}{dy^2}+\alpha^4\varphi\right), \tag{7}$$

$$\varphi(1) = \frac{\omega}{\alpha}, \quad \frac{d\varphi}{dy}(1) = 2, \quad \frac{d\varphi}{dy}(0) = \frac{d^3\varphi}{dy^3}(0) = 0.$$

In terms of this function, the components of the eigenfunctions $q_n$ are expressed as

$$u_n = \sigma_n\frac{d\varphi_n}{dy}, \quad v_n = -i\sigma_n\alpha_n\varphi_n,$$

$$p_n = \frac{\sigma_n}{i\alpha_n\mathrm{R}}\left(\frac{d^3\varphi_n}{dy^3}-\alpha_n^2\frac{d\varphi_n}{dy}\right) - \sigma_n\left(1-y^2-\frac{\omega}{\alpha_n}\right)\frac{d\varphi_n}{dy}-2\sigma_n y\varphi_n,$$

where

$$\sigma_n = [K-\omega^2M-i\omega D+\alpha_n^2T+\alpha_n^4B]^{-1},$$

$$\varphi_n = \varphi(y; \alpha_n).$$

The eigenfunctions are normalized so that $p_n(1) = 1$, and the eigenvalues $\alpha_n$ satisfy the dispersion relation

$$\Phi(\alpha_n) = \sigma_n, \tag{8}$$

where the left-hand side is expressed in terms of the solution of problem (7) as

$$\Phi(\alpha) = i\alpha\mathrm{R}\left[\frac{d^3\varphi}{dy^3}(1;\alpha)-2\alpha^2\right]^{-1}.$$

Relation (8) contains the flexibility parameters of the walls in the explicit form and, for $\sigma_n = 0$, takes the form of the dispersion relation $\Phi(\alpha_n) = 0$ for the flow in the channel with rigid walls.

This work is primarily focused on the passage of the Tollman–Schlichting wave through the joint between the rigid and flexible segments of the channel. First, we consider the evolution of perturbations in the channel containing a finite flexible segment in the interval $l_1 \le x \le l_2$. The joints between the flexible and stationary segments of the walls are assumed to be rigid:

$$f(l_1) = f(l_2) = \frac{df}{dx}(l_1) = \frac{df}{dx}(l_2) = 0. \tag{9}$$

The problem specified by Eqs. (1), (2), (4), (5), and (9) was solved in [2] by direct numerical simulation, which required extensive computations. To reduce calculation time, we propose a method using the solution [3] of the problem of the response of the plane Poiseuille flow to the local vibrations of the channel walls. Let us represent perturbed motion in terms of a superposition of the Tollman–Schlichting wave propagating in a channel with rigid walls and forced perturbation generated by antisymmetric vibrations of the walls of the flexible segment. As a result, we obtain the relation between pressure perturbation on the upper wall $p_\mathrm{w}(x)$ and the unknown distribution of the complex amplitude of wall vibrations $f(x)$, which is specified by the Fourier transform:

$$p_\mathrm{w} = \exp(i\alpha_1x)+I[f], \tag{10}$$

$$I[f] = \int\limits_C [2\pi\Phi(k)]^{-1}dk\int\limits_{l_1}^{l_2} f(\xi)\exp[ik(x-\xi)]d\xi,$$

where the integration contour $C$ passes from below the pole $k = \alpha_1$, which corresponds to the unstable mode (and does not encircle other poles in the lower half-plane). At the same time, flexibility law (4) provides the second relation between $p_\mathrm{w}$ and $f$. Excluding pressure perturbation from relations (4) and (10), we arrive at the following linear inhomogeneous integro-differential equation for the unknown function $f(x)$:

$$B\frac{d^4f}{dx^4}-T\frac{d^2f}{dx^2}+(K-\omega^2M-i\omega D)f = \exp(i\alpha_1x)+I[f]. \tag{11}$$

As an example, we apply the method to the flow in a channel with Reynolds number $\mathrm{R} = 12\,000$. Let the flexible segment occupy the interval $10 \le x \le 60$ and be characterized by the parameters $K = 0.5$, $M = 2$, $D = 0.1$, $T = 0.1$, and $B = 0.15$. Figure 1 illustrates the passage of the instability wave with frequency $\omega = 0.24$ through the flexible segment. Figure 1a shows the longitudinal distribution of the complex amplitude of pressure pulsations on the upper wall. The solid line $\mathrm{Re}\,p_\mathrm{w}$ corre-

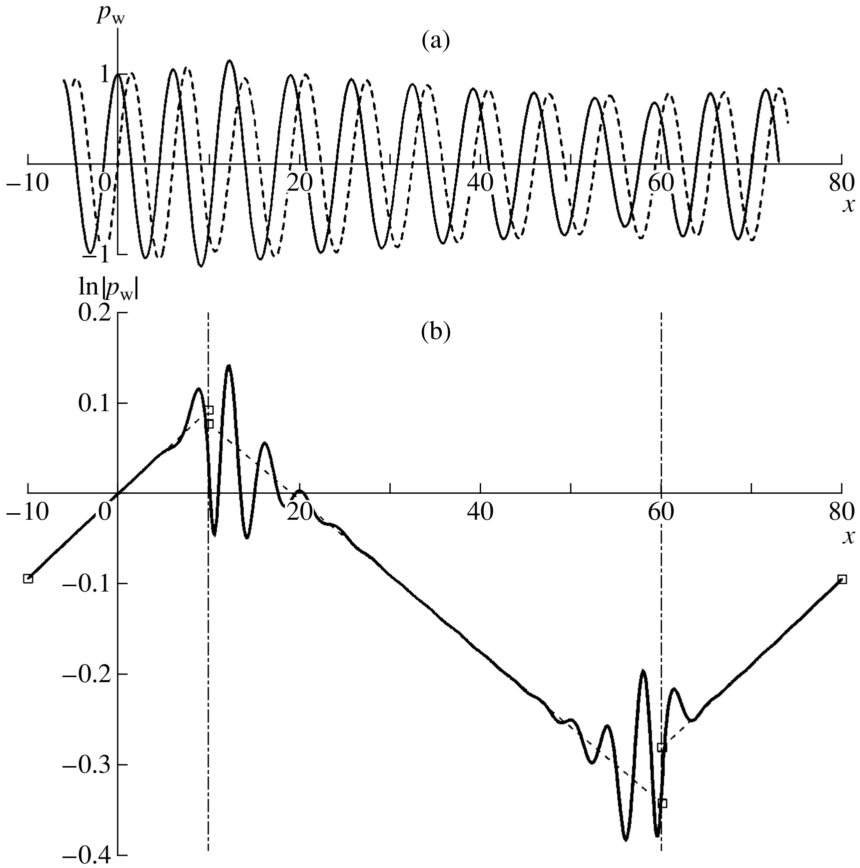

**Fig. 1.** (a) Complex amplitude of pressure pulsations on the wall and (b) curve of increasing perturbation when the instability wave passes through the finite flexible segment.

sponds to the longitudinal distribution of pressure perturbation at the initial time, and the dashed line Im$p_w$, after a quarter of the vibration period. Figure 1b shows the corresponding curve of increasing perturbation. The dash–dotted lines show the position of the flexible segment. Perturbation on the left and right of the flexible segment (excluding the vicinities of the joints) is an increasing wave whose parameters are very close to those of the instability wave in an infinite channel with rigid walls ($\alpha_1 = 1.032 - i \cdot 0.0093$). Perturbation inside the segment is also well approximated by the damping Tollman–Schlichting wave in the channel with uniformly flexible walls ($\alpha'_1 = 0.934 + i \cdot 0.0084$).

Thus, the propagation of perturbation can be conventionally divided into the following stages. First, the unstable mode corresponding to the rigid walls falls onto the flexible segment from the left. Second, this mode is transformed into the same mode for the channel with uniform flexibility. Third, the inverse transformation occurs at the right joint. This qualitative description is represented by the dashed lines in Fig. 1b. As is seen, the amplitude of the unstable mode changes stepwise at the joints between the rigid and flexible walls (it is most pronounced at the right joint).

To analyze the transformation of perturbation at the joints between rigid and flexible walls in more detail, we consider a model problem of the passage of the instability wave through the joint region between two semi-infinite segments. Let the $x < 0$ region be occupied by the rigid segment, and the $x > 0$ region, by the flexible segment with the above parameters. Perturbation both up- and downstream of the joint is a superposition of modes (6). Pressure perturbation on the upper wall is given by the expressions

$$
\begin{aligned}
p_w &= \sum_{n=1}^{\infty} c_n \exp(i\alpha_n x), \quad x < 0, \\
p_w &= \sum_{n=1}^{\infty} c'_n \exp(i\alpha'_n x) + \sum_{n=1}^{4} c^{\circ}_n \exp(i\alpha^{\circ}_n x), \quad x > 0.
\end{aligned}
\qquad (12)
$$

In addition to the wave numbers of the unstable mode for the rigid and flexible segments, we present the wave numbers of other very important modes. Calculation of hydrodynamic modes in the rigid segment yields $\alpha_2 = -0.310 - i \cdot 0.817$, $\alpha_3 = -0.364 + i \cdot 0.833$, $\alpha_4 = 0.503 + i \cdot 0.627$, and $\alpha_5 = 0.590 + i \cdot 0.399$. The corresponding

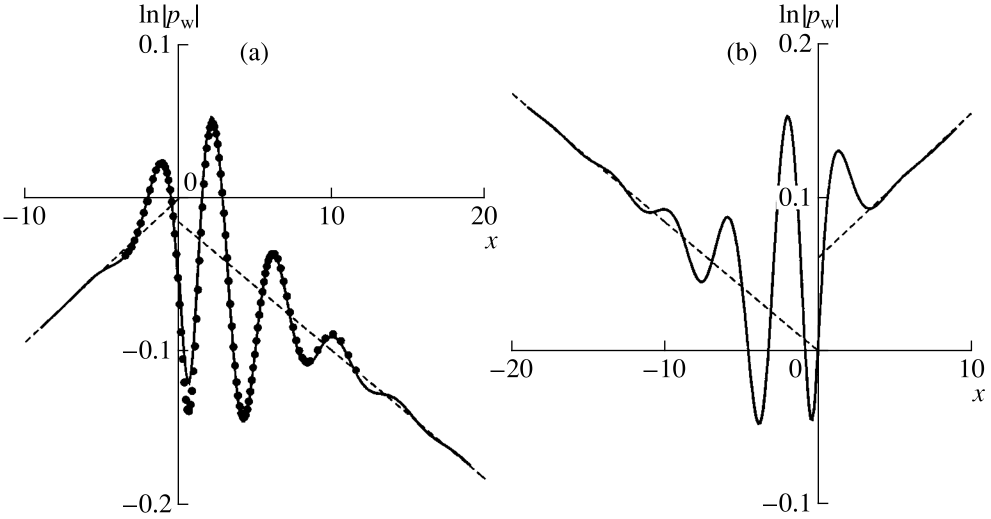

**Fig. 2.** Transformation of the instability wave at the joint between the semi-infinite rigid and flexible segments when the flexible segment is on the (a) left and (b) right.

modes in the flexible segment are as follows $\alpha'_2 = -0.696 - i \cdot 0.356$, $\alpha'_3 = -0.616 + i \cdot 0.320$, $\alpha'_4 = 0.547 + i \cdot 0.566$, and $\alpha'_5 = 0.622 + i \cdot 0.436$. Moreover, there are four additional flutter modes in the flexible segment: $\alpha^\circ_1 = -0.587 + i \cdot 1.338$, $\alpha^\circ_2 = 0.843 + i \cdot 0.981$, $\alpha^\circ_3 = -0.526 - i \cdot 1.263$, and $\alpha^\circ_4 = 0.907 - i \cdot 0.971$.

For a given structure of perturbations (12) in the $x > 0$ region, i.e., for given coefficients $c'_n$ and $c^\circ_n$, we determine the form of vibrations of the flexible segment by using flexibility law (4). The structure of perturbations over the entire flow can be calculated by using the known form of vibrations of the walls and solution of the vibrator problem [3]. Using the Cauchy theorem on residues, we obtain the weight coefficients of expansion (12) for $x < 0$ in the form

$$c_n = \sum_{m=1}^{\infty} S'_{nm} c'_m + \sum_{m=1}^{4} S^\circ_{nm} c^\circ_m. \qquad (13)$$

Here,

$$S^{',\circ}_{nm} = \frac{\sigma^{',\circ}_m}{\alpha^{',\circ}_m - \alpha_n} \left[ \frac{d\Phi}{d\alpha}(\alpha_n) \right]^{-1}$$

are the infinite-dimensional scattering matrices.

The problem of the transformation of the instability wave at the joints between the rigid and flexible segments of the channel is formulated as follows. Let the Tollman–Schlichting wave with the amplitude $c_1 = 1$ fall on the joint region from the left. The complex amplitude $c'_1$ of the transmitted wave is called the scattering coefficient and is denoted as $S$. We impose the conditions of the damping of the corresponding perturbations up- and downstream of the joint on the coefficients of expansions (12) for other modes; i.e., $c_n = 0$ for $\mathrm{Im}\,\alpha_n > 0$ and $c^{',\circ}_n = 1$ for $\mathrm{Im}\,\alpha^{',\circ}_n < 0$. Other coefficients, as well as $S$, are unknown and satisfy the linear algebraic system determined by expressions (13), the above conditions, and the relations

$$\sum_{n=1}^{\infty} \sigma'_n c'_n + \sum_{n=1}^{4} \sigma^\circ_n c^\circ_n = 0,$$

$$\sum_{n=1}^{\infty} \sigma'_n \alpha'_n c'_n + \sum_{n=1}^{4} \sigma^\circ_n \alpha^\circ_n c^\circ_n = 0,$$

following from conditions (9) written for the joints at $x = 0$.

The above problem was solved by the finite-dimensional approximation including all flutter and five hydrodynamic modes mentioned above. The calculation is shown by the solid line in Fig. 2a in comparison with (points) the calculation based on the integro-differential equation of the evolution of perturbations near the front boundary of the long finite flexible segment ($0 \le x \le 100$). As is seen, the results agree well with each other except for the narrow vicinity of the joint. Accuracy can be improved by including the dynamics of a larger number of hydrodynamic modes. The evolution of the perturbation component corresponding to the unstable mode is shown by the dashed line in Fig. 2 and illustrates the amplitude jump. This jump is determined by the value $|S| = 0.985$, and $\arg S = 0.119$ characterizes the phase shift between the transmitted and incident waves.

The problem of the transformation of the Tollman–Schlichting wave passing from the flexible segment to the rigid one is formulated similarly. Figure 2b shows calculations for this case. The transformation process is characterized by the values $|S| = 1.064$ and $\arg S = 0.115$. Thus, the right joint provides the additional destabilizing effect on the configuration under consideration. This effect is stronger than the stabilizing effect of the left joint by a factor of about 4.

## ACKNOWLEDGMENTS

This work was supported by the Russian Foundation for Basic Research (project nos. 02-01-00149 and 04-01-00632) and the Council of the President of the Russian Federation for Support of Young Russian Scientists and Leading Scientific Schools (project no. NSh-1984.2003.1).

## REFERENCES

1. *Proceedings of IUTAM Symposium on Flow in Collapsible Tubes and Past Other Highly Compliant Boundaries, Warwick, 2001* (Kluwer, Dordrecht, 2003).
2. C. Davies and P. W. Carpenter, J. Fluid Mech. **335**, 361 (1997).
3. S. V. Manuĭlovich, Izv. Akad. Nauk, Mekh. Zhidk. Gaza, No. 4, 12 (1992).

*Translated by R. Tyapaev*